

# Politecnico di Torino

Master of Science Program in Energy and Nuclear Engineering Academic year 2024/2025 October Session 2025

Master's degree Thesis

# Design of an experimental erosion test section in lead

Promotors:

Candidate:

Prof. Roberto Bonifetto, Politecnico di

Lara Massa

**Torino** 

Ir. Steven Keijers, SCK•CEN

#### **Abstract**

To support the transition towards low-carbon energy systems, new reactor concepts are being developed to offer greater flexibility and reduced construction costs. Among these, the Lead-cooled Fast Reactor (LFR) stands out for the favourable properties of lead as a coolant and its potential for simplified design. Despite its advantages, several technical challenges remain. This thesis focuses on one of them: the erosion corrosion phenomena induced by heavy liquid metal flow on protective layers within reactor components.

One important aspect to investigate is the erosion that the heavy liquid metal flow can induce on the passive-corrosion layers present along the fuel bundles and along the heat exchanger tubes. This can be a problem if it is not controlled, because the corrosion layer helps to protect the base material. For this reason, a fluid-dynamic study on the design of a specific test-section is performed.

In this thesis a test section is designed that permits to understand through CFD analysis the stresses and the velocity fields achieved in specific typical representative geometries, trying to study and stretch the rule of thumb erosion limit of 2 m/s now adopted in the reactor design. This study aims to determine whether this can be relaxed and at what condition. During this thesis only the design and the CFD simulation work is performed. The test section will be placed into the lead loop for a long period, then it will be extracted and analysed to understand where erosion takes place. With the experimental information and knowing the condition inside the test section given by the CFD analysis, it will be possible to learn more on the erosion behaviour of liquid lead.

Particular attention was given to areas with high velocity, shear stress and turbulence kinetic energy, which are likely to influence erosion corrosion phenomena. The design of the test section includes as representative geometries an array of cylinders in crossflow, two plates with holes and three inclined plates.

#### Key findings include:

- the array of cylinders permits to reach gradually high velocities. It shows less chaotic flow in the first columns making erosion corrosion coupling more straightforward, while the last columns exhibit high turbulence and velocity peaks;
- plates with holes give interesting results in terms of shear stress in the restrictions. They
  generate the highest shear stress in the test section, especially in rounded restrictions, which
  also reach the highest velocities. Sharp restrictions, despite lower velocity, still produce high
  shear stress and should be avoided in design;
- inclined plates permit to study the influence of the flow angle which can form with the solid surface. The 45° inclined plate shows expected shear stress peaks, but elevated TKE values upstream must also be considered.

These results provide a valuable foundation for interpreting future experimental data and refining design criteria for erosion corrosion mitigation in LFR systems.

## Acknowledges

This thesis marks the end of my long and emotional journey, throughout the engineering world and a personal growth. University has changed me profoundly, it has taught me responsibility, while engineering itself pushed my limits and helped me understand what I am truly capable of.

First of all, I want to thank my mentor at SCK•CEN, Steven Keijers. He gave me the opportunity to dive deeply into a subject I am passionate about, always providing the support and motivation I needed. Steven is a sensitive and insightful person who always helped me see the right path. I am also deeply grateful to all the colleagues at SCK•CEN, who were valuable both professionally and humanely. It is a place rich not only in knowledge but in kindness, where collaboration leads to great things. A special thanks also goes to my supervisor at Politecnico, Roberto Bonifetto. He was very supportive and attentive to my work, something I appreciated deeply.

I am incredibly grateful to the people I met in Belgium, who became my second family while I was far from my own. Rosario, Andrea, Candela, Alessandro (x2), Alessio, Diego, Francisco, Michele and Marco, you are and will always be very important to me. Thank you for all the time we shared together, for the memories and emotions that helped me through moments of homesickness.

A heartfelt thank you also to my group of friends in Italy and to Giulia, who always gave me the strength and joy to push through these five years of university.

The deepest gratitude goes to my family, my mum and dad, who gave me every possible opportunity to make this journey a success. Not just in terms of financial support, but above all through your love. You are the greatest inspiration in my life, I have always felt deeply loved. I know how much you longed for a child and you should know that I still search for the comfort of your warm and understanding eyes wherever I go.

Lastly, my final and most heartfelt acknowledgment goes to the truest love of my life, Francesco. There is not much I need to write here, because you already know everything, probably even better than I do. You have been my biggest supporter, not only of this thesis but of my entire academic path. If I pursued nuclear engineering it is because you gave me that final and crucial push, telling me that I could do it. And you were right: I did. But without you, I might never have started and I certainly would not have gone through these years with the same lightness and the same feeling of being so loved.

Thank you, nuclear world. You have challenged me deeply, but you are what makes my eyes light up with curiosity and wonder. You are tough but incredibly rewarding.

# Summary

Abstract	i
Acknowledges	ii
Summary	iii
List of Tables	V
List of Graphs	vi
List of Figures	vii
Acronyms	x
Introduction	1
1.1 Generation IV reactors and SMRs roles	1
1.2 Lead-cooled Fast Reactor	2
1.2.1 LFR project history and today's development	2
1.2.2 MYRRHA project and SCK•CEN infrastructure	3
1.3 Liquid lead as a coolant	
1.3.1 Erosion-corrosion phenomenon	4
1.4 Aim of the work	7
Chapter 2 - Perspective of the analysis and methodology	9
2.1 Experimental background	9
2.1.1 Description of the loop	
2.1.2 Test-section	
2.2 Simulation setup	
2.2.2 Computational domain	
2.2.3 Models	
2.2.4 Mesh generation	
2.2.5 Assumptions	
2.2.6 Numerical analysis	
2.3 Design method	
2.3.1 One Factor At Time (OFAT)	
2.4 Analysis setup	
2.4.1 Fragmented and full geometrical simulation	16
Chapter 3 – Array of cylinders in crossflow	17
3.1 Simulation setup	17
3.1.1 Geometry	
3.1.2 Mesh generation	
3.2 Design and hydraulic results	
3.2.1 Design	
3.2.2 Hydraulic	20

3.3 Numerical results	25
3.3.1 Convergence	
3.3.2 Grid independence analysis	25
3.4 Unsteady nature of the problem	27
3.4.1 Unsteady simulation setup	28
3.4.2 Unsteady solution	28
Chapter 4 – Plates with holes	31
4.1 Simulation setup	31
4.1.1 Geometry	
4.1.2 Mesh generation	
4.2 Design I: high number of holes, small diameters	36
4.2.1 Design results	
4.2.2 Hydraulic results	
4.3 Design II: low number of holes, larger diameters	30
4.3.1 Design results	
4.3.2 Hydraulic results	
4.4 Numerical results	
4.4.1 Convergence	
4.4.2 Grid independence analysis	
Chapter 5 – Inclined squared plates	
5.1 Simulation setup	
5.1.1 Geometry 5.1.2 Mesh generation	
-	
5.2 Design and Hydraulic results	
5.2.1 Design	
5.2.2 Hydraulic	
5.3 Numerical results	
5.3.1 Convergence	
5.3.2 Grid independence analysis	55
Chapter 6 – Full test section simulation	57
6.1 Full test section characterisation	57
6.1.1 Array of cylinders	58
6.1.2 Plates with holes	
6.1.3 Inclined squared plates	66
6.2 Fragmented and full geometry conclusion	70
Conclusion	71
References	73

# List of Tables

TABLE 1: LFR PROJECTS UNDER DEVELOPMENT [3]	. 2
TABLE 2: GEOMETRY CHOICE FOR THE EROSION-CORROSION PARAMETER TO STUDY	. 7
TABLE 3: SIMULATION COMPUTATIONAL SETUP.	14
TABLE 4: TARGET VELOCITIES ON THE CENTRAL PLANE OF THE CYLINDERS' COLUMNS	17
Table 5: Mesh settings for the array of cylinders	18
TABLE 6: DESIGN POINTS OF THE ARRAY OF CYLINDERS, WHERE R IS THE RADIUS OF EACH COLUMN EXPRESSED IN MM AND	VTHE
MAXIMUM VELOCITY REGISTERED IN M/S	20
Table 7: Final configuration of the cylinders' array	20
TABLE 8: MESH INDEPENDENCE PARAMETERS OF GENERATION.	26
Table 9: Mesh settings for the Design I of plates with holes	32
TABLE 10: QUALITY MESH PARAMETERS OF THE FIRST DESIGN OF PLATES WITH HOLES.	33
Table 11: Mesh settings for the Design II of plates with holes	34
TABLE 12: QUALITY MESH PARAMETERS OF THE SECOND DESIGN OF PLATES WITH HOLES	35
TABLE 13: CHANGES OF THE HOLES' DIAMETER IN THE PLATES.	36
TABLE 14: CHANGES OF THE TYPE AND THE RADIUS OF THE RESTRICTION IN THE PLATES. THE TYPES ARE REPRESENTED AS I	RFOR
THE ROUNDED ONE, C FOR THE CHAMFER AND E FOR THE ORIGINAL EDGE.	36
TABLE 15: DIAMETER EVALUATION FOR THE DESIGN II.	39
TABLE 16: CHANGES OF THE TYPE AND THE RADIUS OF THE RESTRICTION IN THE PLATES. THE TYPES ARE REPRESENTED AS I	RFOR
THE ROUNDED ONE, C FOR THE CHAMFER AND E FOR THE ORIGINAL EDGE.	39
TABLE 17: MESH INDEPENDENCE PARAMETERS OF GENERATION.	47
TABLE 18: MESH SETTINGS FOR THE INCLINED PLATES.	49
Table 19: Inclined plates' Geometrical configuration	50
TABLE 20: MESH INDEPENDENCE PARAMETERS OF THE INCLINED DISKS CASE STUDY.	56
TABLE 21: QUALITY MESH PARAMETERS OF THE FULL TEST SECTION.	57

# List of Graphs

GRAPH 1: WALL SHEAR STRESS FUNCTION OF THE MAXIMUM VELOCITY EVALUATED FOR EACH COLUMN OF CYLINDERS24
GRAPH 2: VELOCITY PROFILE ALONG COLUMN D CROSS-SECTION WITH THREE DIFFERENT MESHES: THE CASE STUDY (FINAL), THE
FINE AND THE COARSE ONES
GRAPH 3: PRESSURE DROP ALONG THE CYLINDERS' ARRAY FUNCTION OF THE NUMBER OF CELLS THROUGH THE MESH
REFINEMENT
GRAPH 4: MAXIMUM VELOCITY AND STRESS VERSUS LOCAL SHEAR STRESS IN THE PLATE A
GRAPH 5: MAXIMUM VELOCITY AND STRESS VERSUS LOCAL SHEAR STRESS IN THE PLATE B
GRAPH 6: VELOCITY PROFILE ALONG THE HOLES A Y-AXIS WITH THREE DIFFERENT MESHES: THE CASE STUDY (FINAL), THE FINE
AND THE COARSE ONES
GRAPH 7: PRESSURE DROP ALONG THE PLATE WITH HOLES GEOMETRY AS A FUNCTION OF THE NUMBER OF CELLS THROUGH THE
MESH REFINEMENT
GRAPH 8: STRESS VERSUS ANGLE OF IMPACT ON THE SURFACES OF THE INCLINED DISKS
GRAPH 9: VELOCITY PROFILE ALONG THE Y-AXIS FOR THE INCLINED PLATES WITH THREE DIFFERENT MESHES: THE CASE STUDY
(FINAL), THE FINE AND THE COARSE ONES
GRAPH 10: WALL SHEAR STRESS FUNCTION OF THE MAXIMUM VELOCITY EVALUATED FOR EACH COLUMN OF CYLINDERS60
GRAPH 11: RELATIVE DIFFERENCE BETWEEN AREA-AVERAGED SHEAR STRESS IN FRAGMENTED AND FULL GEOMETRIES60
GRAPH 12: MAXIMUM VELOCITY VERSUS LOCAL SHEAR STRESS (FULL GEOMETRY)
GRAPH 13: MAXIMUM STRESS VERSUS LOCAL VELOCITY (FULL GEOMETRY)
GRAPH 14: AVERAGED MAXIMUM COUPLED SHEAR STRESS AND VELOCITIES COMPARED TO THE TYPE OF RESTRICTION65
GRAPH 15: MAXIMUM SHEAR STRESS-LOCAL VELOCITY POINTS AND MAXIMUM VELOCITY-LOCAL SHEAR STRESS POINTS FOR THE
THREE TYPES OF RESTRICTION FROM THE SIMULATION WITH UNIFORM VELOCITY PROFILE (SECTION 4) AND FOR THE TOTAL
DOMAIN65
GRAPH 16: STRESS VERSUS ANGLE OF IMPACT, MEASURED ON THE SURFACES OF THE INCLINED DISKS WHERE THE FLUID DIRECTL
IMPACTS. ROUND DOTS ARE THE VALUES OBTAINED IN THIS ANALYSIS, WHILE THE SQUARED ONES ARE OBTAINED IN SECTION
569

# List of Figures

FIGURE 1: VARIATION OF THE MECHANISM OF FLOW ACCELERATED CORROSION AS A FUNCTION OF THE FLUID VELOCITY [7].5
FIGURE 2: ON THE LEFT A SIDE VIEW OF A SAMPLE OF REPRESENTATIVE PATH LINES IS SHOWN, THE COLOURS DENOTE DIFFERENT
STARTING POINT FOR THE PATH LINES. ON THE RIGHT THE TWO TOP VIEW COLOURMAPS SHOW RESPECTIVELY THE PATTERN
OF EROSION-CORROSION DAMAGE RECORDED, WHERE THE DARKER COLOUR INDICATES MORE SEVERE DAMAGES, AND
THEN A CONTOUR PLOT OF THE TKE [8]
FIGURE 3: SCHEMATIC DIAGRAM SHOWING THE EROSION OF API 5L-X65 CARBON STEEL GIVEN BY AN IMPACTING NA-CL LIQUID
STREAM ON ITS SURFACE [9]
FIGURE 4: LIQUID LEAD EXPERIMENTAL LOOP; THE CIRCLE INDICATES WHERE THE TEST-SECTION COULD BE PLACED [12] 9
FIGURE 5: GEOMETRY CONSTRUCTION OF THE ARRAY OF CYLINDERS
FIGURE 6: MESH GENERATION ON THE PLANE YZ WITH X=0 WITH INFLATION LAYERS ZOOM
FIGURE 7: Y <sup>+</sup> CONTOUR ON THE CYLINDERS
FIGURE 8: FINAL GEOMETRY OF THE ARRAY OF CYLINDERS
FIGURE 9: VELOCITY CONTOUR ON THE YZ PLANE AT X=0 OF THE ARRAY OF CYLINDERS
FIGURE 10: CONTOUR PLOT OF THE STATIC PRESSURE ON THE YZ-PLANE AT X=0 OF THE ARRAY OF CYLINDERS21
FIGURE 11: VELOCITY VECTORS ON THE YZ PLANE AT X=0 OF THE ARRAY OF CYLINDERS
FIGURE 12: VELOCITY PROFILE ON THE PLANES XY AT Z EQUALS TO THE CENTRES OF SYMMETRY OF THE COLUMNS OF PIPES. 22
FIGURE 13: CONTOUR PLOT OF THE TKE ON THE YZ-PLANE AT X=0 OF THE ARRAY OF CYLINDERS
FIGURE 14: PATH-LINES OF THE TKE AFTER THE LAST COLUMN OF CYLINDERS
FIGURE 15: WALL SHEAR STRESS ON THE CYLINDERS ARRAY SURFACES
FIGURE 16: RESIDUALS OF THE STEADY STATE SIMULATION OF THE ARRAY OF CYLINDERS
FIGURE 17: REGIMES OF FLUID FLOW ACROSS A CIRCULAR CYLINDER [17]
FIGURE 18: EVOLUTION IN TIME OF THE VELOCITY PROFILE ALONG YZ PLANE. FROM TOP LEFT TO RIGHT: 0,3s, 2,7s, 5,1s, 7,5s,
10,2S AND 12S
FIGURE 19: VELOCITIES EVALUATED AS THE MAXIMUM IN EACH MIDDLE CROSS-SECTION OF THE COLUMNS
FIGURE 20: INITIAL CONFIGURATION TO CREATE THE PATTERN, IN YELLOW THE ONE FOR THE PLATE A AND IN BLUE FOR THE PLATE
B
FIGURE 21: MESH GENERATION ON THE PLANE YZ WITH X=0 ON THE LEFT OF THE FIRST DESIGN OF PLATES WITH HOLES, ZOOM ON
TWO HOLES ON THE RIGHT
FIGURE 22: Y+ CONTOUR OF THE PLATE A ON THE LEFT AND ON THE PLATE B ON THE LEFT FOR THE FIRST DESIGN
FIGURE 23: MESH GENERATION ON THE PLANE YZ WITH X=0 ON THE LEFT OF THE SECOND DESIGN OF PLATES WITH HOLES, ZOOM
ON HOLE 3 ON THE RIGHT
FIGURE 24: SURFACE MESH OF THE DIFFERENT TYPES OF EDGES, RESPECTIVELY SHARP, CHAMFER AND ROUNDED ON THE PLATE
A
FIGURE 25: Y+ CONTOUR OF THE PLATE A ON THE LEFT AND ON THE PLATE B ON THE LEFT FOR THE SECOND DESIGN36
FIGURE 26: PLATES WITH HOLES' FIRST DESIGNS, RESPECTIVELY PLATE A AND B
FIGURE 27: CONTOUR PLOT OF THE STATIC PRESSURE ON THE YZ-PLANE AT X=0 OF THE PLATES WITH HOLES FIRST DESIGN.37
FIGURE 27: CONTOUR PLOT OF THE STATIC PRESSURE ON THE YZ-PLANE AT X=0 OF THE PLATES WITH HOLES FIRST DESIGN38
FIGURE 29: CONTOUR OF THE SHEAR STRESS IN THE INLET WALLS OF PLATE A AND B, RESPECTIVELY, OF THE DESIGN I38
FIGURE 30: DESIGN II OF THE PLATES WITH HOLES, IN YELLOW THE PLATE A AND IN BLUE THE PLATE B
FIGURE 31: CONTOUR PLOT OF THE STATIC PRESSURE ON THE YZ-PLANE AT X=0 OF THE PLATES WITH HOLES SECOND DESIGN.
FIGURE 32: CONTOUR PLOT OF THE VELOCITY ON THE YZ-PLANE AT X=0 OF THE PLATES WITH HOLES SECOND DESIGN40
FIGURE 33: VELOCITY CONTOUR PLOT AT PLANE PARALLEL TO THE WALL OF THE PLATES WITH HOLES, PLACED AT A DISTANCE OF 5
MM COMPARED TO THE LATTER. FROM RIGHT TO LEFT, FRONT A, BACK A, FRONT B AND BACK B41
FIGURE 34: TKE PLOT ALONG THE PLANE YZ AT X=0
FIGURE 35: ZOOM A IN THE VELOCITY (LEFT) AND TKE (RIGHT)
FIGURE 36: ZOOM A IN THE VELOCITY (LEFT) AND TKE (RIGHT)
FIGURE 35: ZOOM 6 IN THE VELOCITY (LEFT) AND TKE (RIGHT)
FIGURE 37: 200M C IN THE VELOCITY (LEFT) AND TRE (RIGHT)
FIGURE 30. STREAMILINES AND CONTOUR OF THE FIRE42

FIGURE~39: TKE~contour~plot~on~a~plane~after~the~plate~A~and~on~a~plane~before~plate~B~(distance~from~them~of~0,5)
MM)43
FIGURE 40: CONTOUR OF THE SHEAR STRESS IN THE INLET WALLS OF PLATE A AND B, RESPECTIVELY, OF THE DESIGN II43
FIGURE 41: CONTOUR OF THE PRESSURE IN THE INLET WALL OF PLATE A AND PLATE B RESPECTIVELY44
FIGURE 42: CONTOUR OF THE SHEAR STRESS IN THE WALL OF HOLES A AND B RESPECTIVELY
FIGURE 43: ZOOM OF THE SHEAR STRESS CONTOUR ON RESTRICTION 1, 2, 3 AND 4 IN PLATE A
FIGURE 44: ZOOM OF THE SHEAR STRESS CONTOUR ON RESTRICTION 5, 6 AND 7 IN PLATE B
FIGURE 45: MAXIMUM VELOCITIES LOCALIZED NEAR THE WALL AT THE RESTRICTIONS
FIGURE 46: MAXIMUM STRESSES LOCALIZED NEAR THE WALL AT THE RESTRICTIONS
FIGURE 47: MESH GENERATION ON THE PLANE YZ WITH X=0 ON THE LEFT, ON THE RIGHT A ZOOM ON PLATE E50
FIGURE 48: Y+ CONTOUR ON THE PLATES
FIGURE 49: DESIGN OF THE INCLINED PLATES
FIGURE 50: PATH-LINES COLOURED BY VELOCITY MAGNITUDE ON THE PLATE E, F AND G (FRONT-SIDE)
FIGURE 51: CONTOUR PLOT OF THE VELOCITY ALONG THE PLANE YZ AT X=0, WHERE THE CIRCLE INDICATES THE PLATE E52
FIGURE 52: VELOCITY MAGNITUDE ON FRONT-PLANES PARALLEL TO THE DISKS AND PLACED AT THE BOUNDARY LAYER DISTANCE
BEFORE THE DISKS THEMSELVES. IN THE FIGURE, FROM THE LEFT, ARE SHOWN PLATE E, PLATE F AND PLATE G52
FIGURE 53: PATH-LINES COLOURED BY TKE IN THE BACK-FACE OF EVERY DISK. FROM LEFT TO RIGHT E, F AND G
FIGURE 54: BACK VIEW OF THE TKE PLOT ON THE SURFACES PARALLEL TO THE PLATES PLACED 5 MM AFTER THESE ONES53
FIGURE 55: TKE ON THE YZ PLANE
FIGURE 56: STATIC PRESSURE CONTOUR PLOTS OF FRONT SURFACES OF THE INCLINED PLATES
FIGURE 57: WALL SHEAR STRESS CONTOURS ON THE FRONT PLATES' SURFACES
FIGURE 58: FULL GEOMETRY TEST SECTION ALONG Z AXIS, WITH RELATIVE DISTANCES BETWEEN THE OBSTACLES AND A FULL
LENGTH OF 1,042 M
FIGURE 59: VELOCITY DISTRIBUTION ALONG YZ PLANE AT X=0 OF THE CYLINDERS ARRAY. ABOVE THE PROFILE OF THE
FRAGMENTED VELOCITY, BELOW THE PROFILE OF THE FULL GEOMETRY
FIGURE 60: TKE DISTRIBUTION ALONG YZ PLANE AT X=0 OF THE CYLINDERS ARRAY. ON THE LEFT THE FRAGMENTED PROFILE, ON
THE RIGHT THE FULL GEOMETRY ONE
FIGURE 61: SHEAR STRESS DISTRIBUTION THE CYLINDERS OF THE COLUMN F; ON THE LEFT THE FRAGMENTED PROFILE, ON THE
RIGHT THE FULL GEOMETRY ONE
FIGURE 62: VELOCITY VECTORS ON A PLANE XY AT A DISTANCE OF 5 MM BEFORE THE INLET OF PLATE B
FIGURE 63: VELOCITY CONTOUR ON YZ PLANE AT X=0 ON THE PLATE WITH HOLES DOMAIN (FULL GEOMETRY)
FIGURE 64: VELOCITY CONTOUR PLOT AT PLANE PARALLEL TO THE WALL OF THE PLATES WITH HOLES (FULL GEOMETRY), PLACED AT
A DISTANCE OF 5 MM COMPARED TO THE LATTER. FROM RIGHT TO LEFT, FRONT A, BACK A, FRONT B AND BACK B62
FIGURE 65: TKE CONTOUR ON YZ PLANE AT X=0 ON THE PLATE WITH HOLES DOMAIN (FULL GEOMETRY)
FIGURE 66: TKE CONTOUR PLOT AT PLANE PARALLEL TO THE WALL OF THE PLATES WITH HOLES (FULL GEOMETRY), PLACED AT A
DISTANCE OF 0,5 MM COMPARED TO THE LATTER. FROM RIGHT TO LEFT, FRONT A, BACK A, FRONT B AND BACK B62
FIGURE 67: WALL SHEAR STRESS CONTOUR PLOT AT PLANE PARALLEL TO THE WALL OF THE PLATES WITH HOLES (FULL GEOMETRY).
FROM RIGHT TO LEFT, FRONT A, BACK A, FRONT B AND BACK B
FIGURE 68: WALL SHEAR STRESS CONTOUR OF THE HOLES' WALLS (FULL GEOMETRY)
FIGURE 69: PLATE WITH HOLES FRONT VIEW, WHERE THE BLACK CIRCLES INDIVIDUATE MAXIMUM VELOCITY, THE ORANGE ONE THE
MAXIMUM SHEAR STRESS AND THE CYAN ONE IF THE MAXIMUM SHEAR AND VELOCITY COINCIDE IN THE ZONE
FIGURE 70: PATH-LINES COLOURED BY VELOCITY MAGNITUDE ON THE PLATE E, F AND G (FRONT-SIDE, FULL GEOMETRY)66
FIGURE 71: CONTOUR PLOT OF THE VELOCITY ALONG THE PLANE XY AT Z=0 OF THE INCLINED PLATES (FULL GEOMETRY)67
FIGURE 72: ZOOM OF FIGURE 51 (A) AND FIGURE 71 (B). IN THE FIGURES ARE UNDERLINED IN THE RECTANGLES THE FRONT
AREAS OF THE PLATE E, WHILE IN THE CIRCLES THE DETACHMENT POINTS OF THE FLUID FROM THE PLATE
FIGURE 73: VELOCITY MAGNITUDE ON FRONT-PLANES PARALLEL TO THE DISKS AND PLACED AT 0,5 MM DISTANCE BEFORE THE DISKS THEMSELVES. IN THE FIGURE FROM THE LEFT PLATE E, F AND G
FIGURE 74: TKE ON THE YZ PLANE
FIGURE 75: PATH-LINES COLOURED BY TKE IN THE BACK-FACE OF EVERY DISK. FROM LEFT TO RIGHT E, F AND G (FULL
GEOMETRY)
FIGURE 77: BACK VIEW OF THE TKE PLOT ON THE E AND G SURFACES PARALLEL TO THE PLATES PLACED 4 MM AFTER THESE ONES.
69

FIGURE 78: SHEAR STRESS AND STATIC PRESSURE CONTOUR PLOTS OF FRONT SURFACES OF THE INCLINED PLATES.......69

# Acronyms

CFD

Computational Fluid-Dynamics

IEA

International Energy Agency

RES

Renewable Energy Systems

SMR

Small Modular Reactor

LFR

**Lead Fast Reactor** 

GFR

Gas-cooled Fast Reactor

SFR

Sodium-cooled Fast Reactor

**SCWR** 

SuperCritical-Water-cooled fast Reactor

VHTR

Very High Temperature Reactor

MSR

Molten Salt Reactor

HLM

Heavy Liquid Metal

**FACE** 

Flow-Accelerated Corrosion and Erosion

DOE

**Design Of Experiment** 

RSM

Response Surface Methodology

TKE

**Turbulent Kinetic Energy** 

HEX

Heat Exchanger

### Introduction

According to the International Energy Agency (IEA), 2024 saw a strong increase in electricity demand compared to the previous years of about 4.2% [1]. The IAE predicts a continued increase of consumption until 2027. This is mainly due to the strong electrification that different application fields are carrying on, as for example the transportation and building electrification and a big demand of electricity from the data centres.

In this framework nuclear is a "clean and dispatchable source of electricity and heat that can be deployed at scale with round-the-clock availability" [2]. In fact, nuclear power can rely on its energy security, and it can help to reduce emissions and be complementary to the RES, which are intermittent in the time. Now, for these reasons nuclear power is again under the eye of scientific and political society, with some innovation given by 4<sup>th</sup> generation reactors and SMRs.

#### 1.1 Generation IV reactors and SMRs roles

The nuclear industry is seeing a resurgence in new capacity generation. In 2025 "63 nuclear reactors are currently under construction, representing more than 70 gigawatts of capacity, one of the highest levels seen since 1990" as reported by IEA [2]. The same agency also reported that in 2025 nuclear power produces around the 10% of global electricity and is "the second-largest source of low-emissions electricity today after hydropower".

Not only is the nuclear industry at the top of its high-level production, but to accomplish this transition new nuclear reactor designs are growing in importance and also the reactor concepts are changing. In fact, the nuclear sector is going deeply through new technology studying, with the 4<sup>th</sup> reactor generation (GEN-IV). It is trying to demonstrate the feasibility of smaller and modular reactor (SMRs) which can face other necessities compared to the ones that are accomplished by today's technology.

GEN-IV (but also the III+) represents a category of advanced large-scale reactors, which aim is to improve compared to the traditional large-scale reactors these keys parameters:

- Efficiency: trying to improve the efficiency of nuclear fuel utilization and minimize the nuclear waste;
- Economic: lowering construction and operating costs;
- Safety: reducing the risk of proliferation and trying to eliminate the off-plant emergency response.

There are several types of design under development, but the GIF selected six of them where the attention and the economical effort has to put major importance: Gas-cooled fast reactor (GFR), Sodium-cooled fast reactor (SFR), Supercritical-water-cooled reactor (SCWR), Very-high-temperature reactor (VHTR), Lead-cooled fast reactor (LFR) and Molten salt reactor (MSR).

Concerning the SMR new concept, the keys are the modularity and scalability which place them to new types of usage, like supporting de-centralized electric grids, but also the big cut in the costs plays an important role. In fact, for this new reactor concept the capital costs of one single project can be reduced to be comparable to the costs of a large renewable energy project; this helps also to reduce the risk for the investors and increase the interest to invest on them. To be cut are not

only the costs, but also the construction time: the modular design can reach the cash flow breakeven up to 10 years earlier than for large reactors [2].

#### 1.2 Lead-cooled Fast Reactor

One of the six selected designs of the GEN-IV is the Lead-cooled Fast Reactor, and the coolant can be liquid lead or, in a few cases, lead-bismuth alloy. In this thesis the focus is on this kind of design due to the coolant behaviour.

#### 1.2.1 LFR project history and today's development

In the 1950s Soviet scientists starts to do research on heavy liquid metals as coolants for nuclear reactors: they built a thermal prototype LBE-cooled reactor in 1959 (BR-5) and then also various Pb-Bi-cooled nuclear submarines. The latter have an operation time of about 80 reactor-years and from this experience some know-how was gained, but it cannot be completely transferrable to modern LFR concepts, due to their different spectrum and conditions of operation.

Because of the differences compared to the Soviet reactors and limited knowledge transfer, some experiments are carried out over the last 25 years; especially Japan studied the LBE heat transfer capability and the corrosion behaviour of the coolant thanks to the creation of the CRIEPI institute.

Today, in 2025, there are no completed LFR reactors, but a LFR reactor technology demonstrator in Russia is under construction and a lot of other projects are under development worldwide. Here are some of them:

Table 1: LFR projects under development [3]

Project name	Country	Power rating	Expected deployment	Fuel
name			date	
ALFRED	EU	300 MWth	2035-2040	MOX
ELFR	EU	1500 MWth	2040-2050	MOX
MYRRHA	Belgium	100 MWth	2036	MOX
DUAL FLUID - 300	Canada	600 MWth	-	SMR, liquid metallic fuel
LFR-AS-30	Italy/UK/France	9 MWth	2030	MOX
LFR-AS-200	Italy/UK/France	480 MWth	2033	MOX
SEALER-55	Sweden	140 MWth	-	Uranium nitrite
SVBR-100	Russia	100 MWe	-	Uranium oxide

G4M	USA	70 MWe	Conceptual design	UN
PEACER	Rep. of Korea	300 MWe	Conceptual design	U-TRU-Zr alloy

So, as can be seen from the table, the projects cover different reactor power rating scales and, in this way, the LFR concept is applied also to SMRs.

The main LFR concept design proposed by GIF operates in the fast neutron spectrum, at high temperature (480-570°C) and atmospheric pressure, but the many advantages of this system are related to its coolant choice. In fact, lead has a very high boiling point (up to 1743°C) and also good neutronic and radiation shielding properties. LFR uses MOX or nitride fuel and concerning the sustainability improvement given by the IV generation it allows for closing the fuel cycle and the transuranic actinides can burn [3].

#### 1.2.2 MYRRHA project and SCK•CEN infrastructure

The MYRRHA LFR project was initially a 57 MWth accelerator-driven system with a liquid lead-bismuth (Pb-Bi) spallation-target coupled with a Pb-Bi cooled subcritical fast nuclear core. Later it became a European fast neutron technology pilot plant for lead and multi-purpose research reactor. The Belgian nuclear research centre, SCK•CEN, is leading the project and currently phase 1 (the building of the linear accelerator) is under construction.

In 2010 the European Commission launched the European Sustainable Nuclear Industrial Initiative (ESNII) to support three GEN-IV fast reactor projects to promote low-carbon energy technologies. To do that ESNII supports economically some projects proposed by different countries, such as:

- France, with the Astrid sodium-cooled fast reactor (SFR), but the project was cancelled;
- Central and Eastern Europe, with the Allegro gas-cooled fast reactor (GFR);
- Romania, with the ALFRED lead-cooled fast reactor (LFR) technology pilot;
- Belgium, with the MYRRHA lead-bismuth facility accelerator driven system.

### 1.3 Liquid lead as a coolant

Liquid lead is chosen as a coolant because of its chemical and physical properties; some of the most important are here reported:

- High lead boiling point (up to 1743°C [4]): it permits low pressure in the primary circuit reducing the thickness of the walls and have a high primary coolant outlet temperature;
- Lead's inertness to air and water: no more hydrogen production and exothermic reaction problems occur;
- High lead density: it has quite good radiation shielding properties because it absorbs alpha and gamma radiation, however low neutron shielding;
- Lead reflecting properties: help the neutrons' economy;
- High lead thermal conductivity (around 18 W/m\*K, at 480°C [4]): it gives the possibility to transport heat in a very efficient way;
- Relatively low viscosity: low pumping power needed.

But some challenges are also present for the deployment of liquid lead, such as [3]:

- High lead melting temperature (around 327°C [4]): this property can lead to problems with the cooling continuity because the liquid lead can solidify and so some design precautions have to be taken into account;
- Lead opacity: it is a problem when some inspections have to be done, but some inspection methods are now under development;
- High density of lead: may pose challenges in seismic design;
- Lead corrosion: it has the tendency to be corrosive at high temperatures (as the one designed for LFR, around 480°C) when in contact with steel. Therefore, careful material selection is needed, and with a continuous coolant chemistry monitoring during plant operations.

Generation IV is still in a developing state, as said before, and some challenges have to be faced. In this work corrosion-erosion is studied by means of fluid-dynamic analysis. This will be done by designing a test section where different fluid-dynamic conditions are induced to investigate in which circumstances the most penalising situations for the flowing liquid lead erosion occur.

#### 1.3.1 Erosion-corrosion phenomenon

Erosion-corrosion is common in systems where a fluid flows on a metal surface, and it depends on two synergetic factors: the velocity and the corrosiveness of the medium. With the term "FACE" (flow-accelerated corrosion and erosion) it is possible to refer to this synergetic phenomenon.

#### 1.3.1.1 Velocity parameter

A high velocity increases the turbulence of the liquid film along the wall and also the erosion. Because of that, if some obstructions in the flow are present, they can also cause turbulence and local erosion corrosion damage. It is also important to point out that, depending on the metal and medium properties, below a given velocity no erosion-corrosion phenomenon occurs.

Depending on the turbulence and on the compatible corrosion between metal-coolant, erosion-corrosion can occur in uniform or local forms but always flow-oriented [5].

So, FACE is a chemical and mechanical process (corrosion and erosion, respectively) that affects the metal's surface enhanced by the turbulent flow.

Corrosion of structural metals in HLM can be divided into two categories [6]:

- 1. Dissolution: the interaction by which the medium dissolves directly the structural metal.
- 2. Oxidation: concerns the growth of the oxide layer on the structural metal. This layer plays an important role for the corrosion resistance of the structure because it can prevent further dissolution.

The oxide layer formed on the structural metal can be fragmented and taken away by the turbulent flow thanks to turbulence eddies which enhance the dissolution or due to a weak adhesion between oxide and substrate.

There are recent developments of some structural alloys affected by the liquid lead flow and they show also good corrosion resistance, but the tests are done only at moderate flow conditions [6]. Figure 1 shows how the velocity impacts the erosion rate.

- At relatively low velocity (around 0,3 m/s), the thickness of diffusion boundary layer (DBLs) reduces with increasing velocity: the corrosion rate increases due to a faster transfer of species from the structural material's surface to the fluid flow;
- When the DBL is sufficiently thin and does not limit the reaction through species transfer, the corrosion reaction rate will be governed only by its activation energy. This energy is influenced

by the type of reactants and the reaction temperature. As a result, the flow velocity will have no impact on the corrosion rate, which will stabilize at a constant value (after reaching a plateau) at intermediate velocities.

- At high flow velocities, turbulence effects become significant, but the interaction between turbulence, mechanical damage, and erosion remains poorly understood.
  - Fluctuations in hydrodynamic forces can lead to low/high-cycle fatigue, influencing slip plane relocation.
  - Therefore, oxide layers on the surface experience cyclic stress but may be less prone to classical fatigue due to their lack of grain structure.
  - Cracks may form at the oxide-substrate interface, leading to oxide layer detachment.

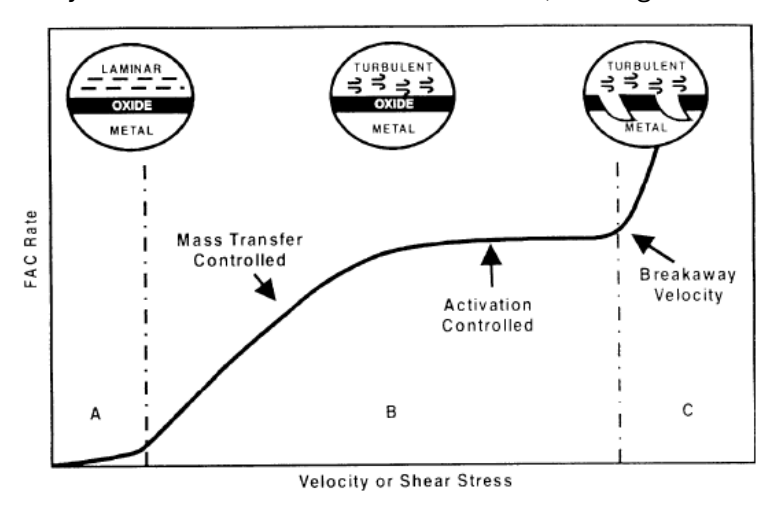


Figure 1: variation of the mechanism of flow accelerated corrosion as a function of the fluid velocity [7].

It is important to remark that the high velocity field has yet to be investigated, but, as said also before, FACE is believed to result from mechanical removal due to dissolution weakening and reduced adhesion between the oxide layer and substrate. With the test section designed in this work the velocity will be increased to values higher than the today's limit of 2 m/s to investigate this range of velocity.

#### 1.3.1.2 Turbulence parameter

It is true that the exact mechanism of erosion-corrosion is not known at high velocities, but the existence of a link between turbulence and erosion-corrosion is found in the work of Nešic about the CFD use in combating erosion-corrosion [8]. In fact, Nešic proved that the "near wall turbulence intensity is a good hydrodynamic predictor of corrosion-erosion damage in complex geometries".

To do that he observed that in his experiment on HEX, the inclined flow formed recirculation regions, which then re-attach to the surface and the areas near these re-attachment points are characterised by a too low shear stress compared to the erosion-corrosion resulting from.

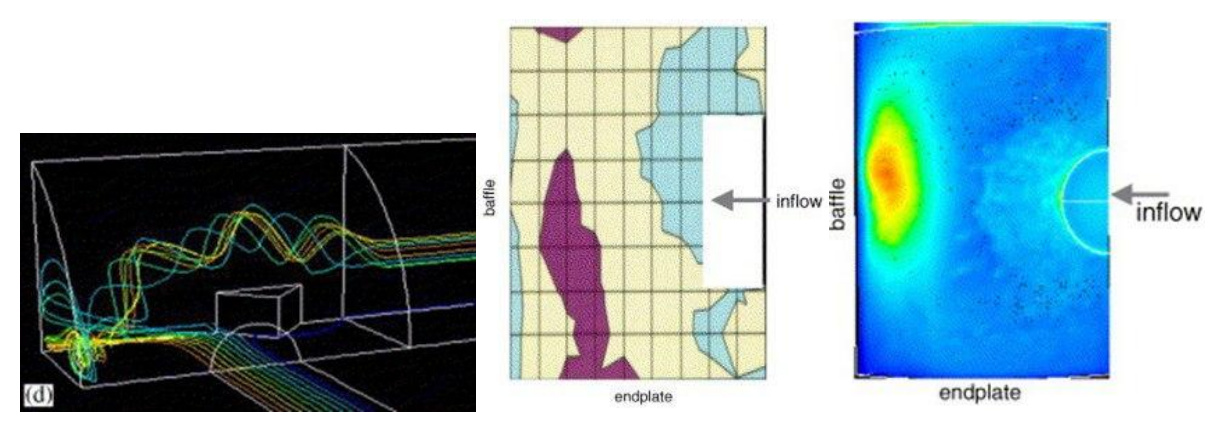


Figure 2: On the left a side view of a sample of representative path lines is shown, the colours denote different starting point for the path lines. On the right the two top view colourmaps show respectively the pattern of erosion-corrosion damage recorded, where the darker colour indicates more severe damages, and then a contour plot of the TKE [8].

Because of that Nešic concluded that the shear stress can not mechanically remove alone the protective layer of the metal, but there was some other parameter which affects the phenomena. So, he investigated these areas and he found that they are characterized by a high level of turbulence, which can enhance the corrosion by the increase of mass transfer rates and the mechanical removing of the protective layer.

#### 1.3.1.3 Impingement angle parameter

Not only the high velocity is a key parameter for the FACE, but also the liquid impingement angle is important. Studies performed by Toor et al. [9] have shown a correlation between impact angle and erosion rate at liquid-solid flow interaction. This study was done on carbon steel (API 5L-X65) where liquid Na-Cl without solid particles was used as impingement liquid, but the results can be easily transferred to liquid metal. The results indicate that for fluid velocities below 12 m/s, the erosion rate peaks at 45° and it has a minimum at 90°.

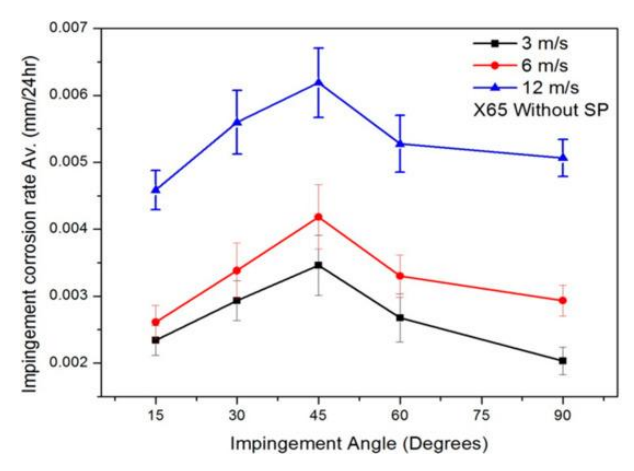


Figure 3: schematic diagram showing the erosion of API 5L-X65 carbon steel given by an impacting Na-Cl liquid stream on its surface [9].

It is reported that both the shear and normal stress play an important role during fluid impingement, where shear stress is dominant at lower angles and vice versa. Toor et al. observed that the highest corrosion rate at 45° can be due to the balance between shear and impact force.

In fact, it is important to observe that at low impact angles the shear stress is obviously higher, and it enhances erosion-corrosion by removing partially or entirely the corrosion layer. While

increasing the impingement angle the shear stress is lower, and the normal stress starts to increase. Normal stress damages the surface, but it provides somewhat protection because it does not contribute to the removal of the oxide protecting layer [10]. This explains why the corrosion rate decreases with the impingement angles.

#### 1.4 Aim of the work

These results give a reason why a lot of studies concentrate on the shear stress as one of the most important factors which increases the corrosion rate at high fluid velocities. But also, given the high density of HLMs, the erosion mechanics at critical impact angles cannot be underestimated and have to be under control.

So, in this work, a setup for a test section will be designed to obtain the best flow conditions to investigate the erosion-corrosion phenomena with the parameters discussed before which can affect it.

Table 2: Geometry choice for the erosion-corrosion parameter to study.

Parameter	Geometry	
Velocity	Bundle of pipes	
Shear stress	Plates with holes	
Impact angle	Inclined plates	

The bundle of pipes is chosen because on them it is possible to analyse the classical situation of a heat exchanger and tuning the pitch between them it is possible to significantly accelerate the flow.

The choice of plates with holes is interesting to study the shear stress on different holes' restrictions, the pressure drops and shear stress created by the jets on the following grid surface.

The inclined plates are chosen to study principally the effect of the impact angle of the flow.

# Chapter 2 - Perspective of the analysis and methodology

The goal of the thesis is to design a test section that creates typical flow condition in a nuclear reactor, where it is expected to see the erosion corrosion phenomena explained before. The typical flow conditions are:

- Cross flow over a bundle of pipes (in heat exchangers);
- Parallel flow in bundle (fuel assemblies);
- Flow restrictions, high velocity zones, impact of jets (orifices, pressure drop plates);
- Behind objects (recirculation zones, re-attachment zones).

This test section should combine several of the above indicated flow types at velocity challenging the current design limits.

#### 2.1 Experimental background

At SCK•CEN currently an experimental setup was developed to investigate the erosion on a rotating disk and is ready to start operation in the near future. No experimental data are available yet. As this experiment focuses on the velocity magnitude, it will give only limited info on more complex flow fields.

The available loops at SCK•CEN were screened to allow to fit in the extra erosion test section with the aim as described before.

#### 2.1.1 Description of the loop

The EU-SMR-LFR project is the strong consortium composed by well-known European partners: SCK•CEN, Ansaldo Nucleare, ENEA and RATEN [11].

The important contribution of the SCK•CEN is on lead-coolant and material research. The perform this research the SCK•CEN operates several lead loops to study the behaviour of the liquid lead on materials and components. One of these loops is called "Hydrobear" to test hydrostatic bearings. The loop is represented in the following figure:

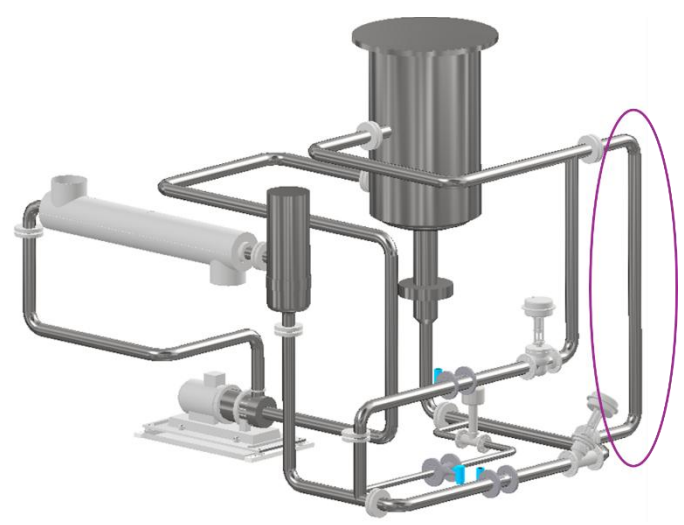


Figure 4: Liquid lead experimental loop; the circle indicates where the test-section could be placed [12].

The purple mark indicates the vertical tube called Gulliver, where the test section subject of this study will be placed in. The valve settings can be chosen to combine operations of the bearing and the erosion tests. As long as the bearing tests do not need the full mass flow rate.

#### 2.1.2 Test-section

The test section is composed by a cylindrical tube of internal diameter 101.6 mm and a length of about 2 m. Inside it, it is possible to insert the obstacles introduced in Table 2 which could create the targeted flow conditions.

#### 2.1.3 Test operating conditions

The test section will be operated at a constant mass flow rate and isothermal. The temperature of the liquid lead is taken equal to 380°C (the cold plenum temperature of the SMR-LFR coolant) and the associated physical properties important for the analysis are evaluated as follows (with the temperature in K):

$$\rho = 11291 - 1.165 * T \left[ \frac{kg}{m^3} \right] \tag{1}$$

$$\ln(\eta) = \frac{1004.3}{T} - 7.5988 \left[ Pa * s \right] \tag{2}$$

The density, evaluated with Miller, has a value of 10536 kg/m $^3$  and the viscosity, with Kutateladze, of 0.00233 Pa\*s [4].

### 2.2 Simulation setup

First, the optimisation of the three different flow obstacles in the test section is made separately to limit the calculation efforts and the many possible combinations of the parametric cases.

CFD models can be used to optimize any design following the proper criteria. In fact, CFD is a tool that solves the Navier Stokes equation for fluid flow into a simulation domain created by a 3D drawing tool and divided into many cells. Thanks to this tool, the simulations are very important to understand the hydraulic behaviour of the fluid inside specific geometries and conditions, and with this information it is possible to create the best design for the specific purpose.

In this context, it is possible to investigate the design parameters' sensitivity and analyse where the fluid reaches limiting condition (erosion-corrosion related). The limited condition assumed in this analysis is based only on an average velocity of 2 m/s, while other limiting parameters are not known. These unknown limiting parameters are wanted to be obtained from the experimental setup developed in this analysis. These type of CFD analysis are important to build the proper design, but also to compare the successive experimental results with the known fluid dynamic. In fact, with this last concept, it is possible to couple the erosion-corrosion cause-effect.

When specific properties are look for and there are many free parameters, the characterisation of the design space becomes complex. Therefore, following a systematic and mathematical procedure called Design Of Experiment (DOE) and the use of a Response Surface Methodology (RSM) can be applied while using a parametric CFD model. In this thesis the general purpose CFD code Ansys Fluent 2024 R1 is used.

In this case the steps are the following:

- 1. The first step is to create a geometrical model (draw in the CAD tool within the ANSYS package called Discovery) and create the geometrical input in a parametric way;
- 2. A complete CFD analysis is done with Fluent on this first design and the physical outputs are defined;
- 3. Still in Fluent a manual parametric analysis is done with the "one factor at a time" (OFAT) approach;
- 4. A DOE analysis is finally pursued;
- 5. A RSM is created and analysed to understand what the values of the parameters are to reach the searched hydraulics properties.

If the geometry has only a few design parameters, the analysis stops at the third point to not increase too much the computational cost and the time requested to complete a DOE analysis. In this thesis the analysis stops at the OFAT step because of that.

As mentioned previously, the simulation analysis will be important not only to assess the design of the test section but also in a second moment, to couple the cause-effect of erosion-corrosion. This in practice means to find a correlation between the damage on the surface with the studied parameters such as local velocity, shear stress or turbulence intensity. So, the goals of the numerical simulation are two: find an optimal design and do an accurate analysis of the results that might cause damage on the structures in final experimental step.

For these reasons, it is important to have an accurate numerical model where the information, such as shear stress and velocity, is well analysed locally. This goal is pursued with Ansys Fluent 2024 R1 programme, a fluid simulation software, which has advanced physics modelling capabilities, which include turbulence modelling.

Now with the following sections the procedure is better explained, and the methodology is also introduced.

#### 2.2.1 Ansys Fluent setup

Ansys gives the opportunity to create the project step by step, thanks to Component Systems which are linked all together inside Ansys Workbench, the graphical users environment from which it is possible to manage all the project.

First, the geometry, and consequently the CAD model, needs to be created. In this work, this is accomplished using the Discovery 2024 component system. Within Discovery, it is possible to assign geometrical values as parameters, which is particularly useful given the iterative nature of the analysis required.

Before the mesh programme is launched, the interface of Ansys Launcher appears and here it is possible to insert how many parallel solver processors are wanted to use and the solver option. The workstation used has 20 processor cores and to permit to have faster simulations it is chosen to work with 18 of them, leaving 2 free for whatever other programme is in use during the solving. Concerning instead the solver options, it is chosen the Double Precision one, because the variety of the length scales where a single precision may not be adequate to represent the node coordinates [13].

In the double-precision solver, each floating-point number is represented using 64 bits, instead of 32 used by the single-precision solver. The extra bits increase the precision but also the range of magnitudes that can be represented, but the negative aspect of double precision is the use of more memory.

Secondly, the meshing process must be carried out, and Ansys Fluent Meshing is selected as the component system due to its user-friendly interface. It enables mesh generation through a straightforward workflow, while integrating the full capabilities and features of previous equivalent programs.

Thirdly, the setup and solution stages are performed within Fluent. If needed, output parameters can be defined directly in Fluent. Once all component systems are configured in Workbench, a Parameter Set is automatically generated—thanks to the prior definition of input and output parameters. This allows users to view, in tabular form, all geometric and output parameters associated with each simulation.

#### 2.2.2 Computational domain

The computational domain of each simulation is based on the test section outer tube inside which the obstacle in the study is located. For each obstacle simulation not all the length of the tube is considered, to not increase too much the computational power, but for each of them are taken:

- A length before the obstacle to understand if the velocity profile imposed at the inlet work correctly;
- A length after the obstacle to avoid inflow at the outlet plane of the domain.

#### 2.2.3 Models

The physics models set for the simulation are the following:

- Space: 3D Model, no symmetry can be applied. This because the flow is strongly influenced by different jets and so, also if the geometry can be symmetric, the flow has not perfect hydraulic symmetric profiles.
- Time: Steady State, as a first approach. Later it will be tested if there is not an unsteady driver<sup>1</sup>.
- Solver: Pressure-based.
- Flow: Coupled Flow.
- Viscous regime: Turbulent. With an inlet velocity of 0.8 m/s and considering the reduction in flow area thanks to the obstacles, the flow is characterised by a turbulent behaviour.
- Turbulent model:  $k-\omega$  SST Model. This method can solve with high-accuracy the boundary layer (thanks to the property of the  $k-\omega$ ) and integrate the  $k-\varepsilon$  model in the turbulent mix to improve the calculation.

Remembering about the incompressible flow assumption, it is possible to explain why there is the needs to have a pressure-based solver. It is needed to couple velocity and pressure, since the continuity equation for an incompressible flow does not contain the pressure term. So, the pressure equation is derived from the continuity and the momentum equations to permit that the velocity field, corrected by the pressure, satisfies the continuity itself. Since the governing equations are nonlinear and coupled, the solution requires an iterative process: all the equations are solved iteratively until the results stabilize and convergence is achieved. In this context the coupled flow is used to solve simultaneously momentum and pressure-based continuity equation. In this way the solution converges faster than with a segregated model, but the memory required is more because both the solution for velocity and pressure have to be stored [13].

<sup>&</sup>lt;sup>1</sup>The cylinders' array case-study is an intrinsic unsteady problem, and for this reason the transient is studied but a complete analysis is done in the Chapter 3.

#### 2.2.4 Mesh generation

The mesh generated by Fluent Meshing, as said before, follows a precise workflow.

The first thing to set is the Surface Mesh, where it is possible to insert also local mesh refinement; the second step is the one about the Boundary Layers, which have to be inserted to model accurately the viscous sublayer and as final step the Volume Mesh has to be built.

For the surface mesh the Minimum Size is taken as the smallest size of the geometry and instead the Maximum one as the Maximum Cell Length of the Volume Mesh  $(S_n)$ , which is chosen as the lower boundary layer width. This is calculated as:

$$S_n = x * \frac{1 - r^n}{1 - r} \tag{3}$$

Where x is the lower inflation layer first height, r is the growth rate and n is the number of inflation layers. Usually with the First Height method to construct the inflation layers, it is not fixed the growth rate but the transition rate (TR), so:

$$r = TR^{\frac{1}{n-1}} \tag{4}$$

#### 2.2.4.1 Viscous sublayer

When using the k- $\omega$  SST model it is very important to have a proper mesh. In fact, when this model is selected Ansys Fluent automatically can solve the viscous sublayer if the y<sup>+</sup><1, because the first node of interpolation is inside the layer. If the mesh is not accurate near the walls, it evaluates the viscous sublayer with hybrid method (1<y<sup>+</sup><30) or with pre-defined wall functions (y<sup>+</sup>>30). But because in this work it is needed an accurate analysis of the viscous sublayer, the mesh has to be properly defined. To do that it is necessary to do a preliminary analysis with k-  $\epsilon$  model to find an approximation of the highest wall stress, and then it is possible to evaluate analytically the first layer of the mesh near the interested walls (also called "inflation layer"):

$$y = \frac{y^+ * \mu}{\rho * \sqrt{\frac{\tau_w}{\rho}}} \tag{5}$$

Where  $\mu$  is the dynamic viscosity and  $\rho$  is the density of the liquid lead. Imposing  $y^+=1$  it is possible to find the first layer height. Usually, a first grid can be generated with these inflation layers and a contour of  $y^+$  can be created to verify if it is everywhere near or lower than 1. If it is not  $y^+$  has to be re-evaluated with the new wall shear stress obtained with the previous mesh; the process continues iteratively until an  $y^+\approx 1$  on all the walls is obtained.

In this work the attention is on the obstacles and on how the erosion-corrosion take place on their surfaces, while the information on the wall of the main pipe of the test section is considered of less importance. For this reason, some computational power is saved thanks to the decision to not put a strict inflation layer on this last wall, but only on the obstacles' ones. This can be done because, as previously discussed, the viscous sublayer is always evaluated but maybe with less precision, but the solution it is still acceptable.

#### 2.2.5 Assumptions

Some assumptions for the overall flow are done and are the following:

- 1. Turbulent liquid lead flow, in steady state conditions;
- 2. The flow is incompressible;
- 3. The fluid enters the tube with fully developed velocity profile and uniform temperature;
- 4. The walls are smooth.

In the following table the main information for the computational setup is summarised:

Table 3: simulation computational setup.

Methods	RANS, k-ω SST model	
Time dependence	Stationary	
Meshing strategy	Polyhedral cells with near wall prism layers	
<b>Boundary conditions</b>	Inlet	Velocity: 0.8 m/s <sup>2</sup>
	Outlet	Pressure: 0 Pa
	Walls	No slip walls

#### 2.2.6 Numerical analysis

It is important not only to obtain results with the analysis but also to understand if these results are obtained in a rigorous and correct manner. In fact, a software as Ansys Fluent can give the tools to solve the non-linear partial differential equations of the Navier Stokes, but CFD requires careful assessment of numerical solution accuracy. To be accurate are needed two important passages to read in a correct way the provided solution:

- 1. Verification, which assess the verification of the correct way of equation resolution. In the case study analysed here, it is possible to achieve the verification comparing the results with expectations based on a theory background.
- 2. Validation, which prove if the correct equations are solved but it needs comparison with experiment which are out of the scope of this thesis.

The validation of the CFD results includes the analysis of discretization and modelling errors; it is possible to assume that using a validated code with appropriate convergence criteria, iteration errors can be excluded.

So, first of all, as convergence criteria, and so defining when to stop the iteration process to solve the non-linear equations, the residuals are set at 10<sup>-3</sup>. This because can be proven that "the rate of reduction of error is the same as rate at which the residual and the difference between successive iterates are reduced" [14], and reducing the error of about 2-3 order is enough for this case-study.

The discretization error instead is the difference between the solutions obtained with the exact solution of the equations and the exact solutions of the discretized equations. The concept is that also if the solver solves the discretized equations perfectly, these equations are always approximation of the real ones. So, it is needed to understand the quality of the approximation: it is described in terms of its order of approximation, which relates the truncation error of the approximation to the grid spacing.

<sup>&</sup>lt;sup>2</sup> In 2.4 Analysis setup it is well explained how the velocity inlet condition is imposed.

In the first moment, to solve the problem, it is decided to have first order decomposition of the equations to solve easily an unknown convergence behaviour. Then when the problem starts to be clearer, it is possible to increase the order to achieve a most precise solution, and in this study the order is increased to the second one for the momentum, the pressure and turbulence equations.

The truncation error of a spatial derivative is proportional to  $(\Delta x)^p$  where  $\Delta x$  is the spacing imposed by the grid settings and p the order of approximation. In this analysis this error is not analyse, in fact "is sufficient to show the change in the computed quantity of interest for a series of grids (preferably three). If the change is monotonic and the difference decreases with grid refinement, one can easily estimate where the grid-independent solution lies" [14].

#### 2.3 Design method

Test section design of this type is a multidisciplinary field where fluid-dynamic, structures and control are studied together. The test section in fact has not a pre-defined design, it must be designed from scratch to achieve the desired results and then it has to be optimized to have as much results as possible.

By optimizing the test section design, it is possible to achieve a balance between fluid-dynamics and operational requirements in line with the capabilities of the loop where the test section will be placed.

#### 2.3.1 One Factor At Time (OFAT)

As said at the beginning of paragraph 2.2, after the simulation of the initial design of each obstacle it is necessary to understand if the parameters are well defined and how varying one of them the solution varies. This can be helpful to do a preliminary control to modify the CAD or the simulation if something is not working as expected, but also to understand the range of the geometrical parameters to insert the right range of values in the next steps.

To do that the input and output parameters are defined as explained in the previous sections and thanks to the ability of Workbench to create a parameter analysis it is possible to create multiple simulation to be run varying one input parameter each time. Then the simulations can be launched all together and the CAD will be updated each time, and a new solution (with the same grid) is achieved. In this way the output parameters can be easily seen, and it is immediately understandable what is going on.

Sometimes there are many geometrical parameters and they influence more than one physical output parameter, this parametric analysis is not enough to characterize and optimize the design. In this work only this analysis is pursued and it is enough to construct an accurate design.

### 2.4 Analysis setup

Explaining the erosion-corrosion phenomena three factors are underlined to be important: velocity of the fluid, turbulence intensity and impingement angles. In the various designs these factors are explored, but before some considerations are formulated.

Concerning the velocity is important to remember that the no slip condition on the walls impose a zero velocity on them and so it is necessary to look at the velocity just after the boundary layer of the wall. Usually, it is looked to the maximum velocity, to localize it and then couple this information with the erosion-corrosion phenomena.

The turbulence level can be assessed using the Turbulent Kinetic Energy (TKE), which is associated with turbulent eddies and reflects fluctuations in the velocity components. In his work, Nešić identified critical areas within the experimental section where damage was clearly evident. By plotting pathlines, it became apparent that these regions were characterized by the presence of large vortices. Subsequently, the TKE distribution was analysed revealing that it was high in these critical zones. This study aims to follow a similar approach.

Considering the impingement angle, Ansys Fluent does not permit its visualization and so where the fluid is strongly accelerated and where it impacts straight on the wall, it is considered the angle of the wall as impingement angle.

The shear stress is analysed, also if it is an effect of velocity and impingement angle; this is done because it can give access to immediate information about erosion-corrosion.

#### 2.4.1 Fragmented and full geometrical simulation

Firstly, with the boundary conditions described in Table 3, a fully developed velocity profile is constructed, and it is exported as inlet conditions for each of the geometry described in Section 2.1.2, to standardize each of them. The inlet boundary condition used is characterized by the three velocity components, the turbulent kinetic energy k and its specific dissipation rate  $\omega$ .

Secondly, because it is wanted to know how the geometries influence the others, the inlet condition will be the output one of the previous geometries maintaining all the other assumptions equals. Again, the inlet boundary condition is a velocity one, as before.

Thirdly, the full simulation is run with all the obstacles together, to understand if doing a separated analysis can be a good idea or if the no-linear and turbulence effect are too effective and so it is necessary to fully simulate the test section.

The numerical analyses are done considering the separated geometries, this because the computational cost could be very expensive if the whole test-section geometry is studied all together during the OFAT analysis.

# Chapter 3 – Array of cylinders in crossflow

In this chapter the first configuration of the corrosion erosion set up is developed. An array of tubes is placed in cross flow into the test section. The cylinder array in crossflow is chosen as geometry to analyse deeply the effects of acceleration of the flow, the shear stress and the impact angle. This configuration is representative of flow in a heat exchanger in common LFR designs.

#### 3.1 Simulation setup

This geometry is used to investigate velocity limits, particularly the current standard of 2 m/s, aiming to exceed it by more than a factor of two.

#### 3.1.1 Geometry

The aim is to accelerate the fluid flow in order to investigate how high velocities influence shear stress, and consequently, the erosion-corrosion behaviour of the material. To achieve this, solid cylindrical obstacles are arranged in staggered columns, one behind the other: this staggered placement forms an equilateral triangular lattice in the cross-section of the pipe. As a result, the spacing between consecutive columns is comparable to the lattice size, providing only a short distance for the fluid to travel before directly striking the next column. This configuration takes to assume a perpendicular impact thanks to the alignment of the openings between the cylinders in the front column compared to the solid cylinders in the column behind, forcing the fluid to impact the downstream cylinders at an approximately 90-degree angle.

The idea is to achieve these results in terms of maximum velocities between the cylinders:

Table 4: Target velocities on the central	plane of the c	vlinders' columns.

Cylinder column	Target maximum velocity [m/s]			
а	1,5			
b	2			
С	2,5			
d	3			
е	3,5			
f	4			

The geometrical parameters which can influence these target velocities can be summarized as follows:

- Distance between the cylinders in each column, called transversal pitch  $p_T$ ;
- Distance between the last cylinders of the column and the main tube;
- Radius of the cylinders in the same column and in the ones before the column in study;
- Distance between two columns, called longitudinal pitch  $p_L$ ;
- Numbers of cylinders for each column.

Because the parameters are too many some of these are related between each other.

Firstly, it is decided to have full cylinders (to significantly reduce the number of design possibilities) and to create a regular triangular staggered layout. Thanks to this last decision the number of cylinders for each column is related with the ones of the other columns to be able to create a regular triangular pattern: in a couple of following columns the number of cylinders between them will differ by one. It is possible to call N and n these two numbers to obtain:

$$n+1=N \tag{6}$$

Then these two numbers of cylinders will be repeated for each couple of columns. The diameter of the pipe is divided by N to obtain the maximum diameter of the cylinders which can fit in the pipe in column,  $D_{max}$ .

Secondly, the decision to create the pattern for the configuration of  $D_{max}$  helps to find the centre for each cylinder in the vertical direction. Thanks to the trigonometry it is possible to find also  $p_L$  compared to the first column, in such a way to construct equilateral triangles:

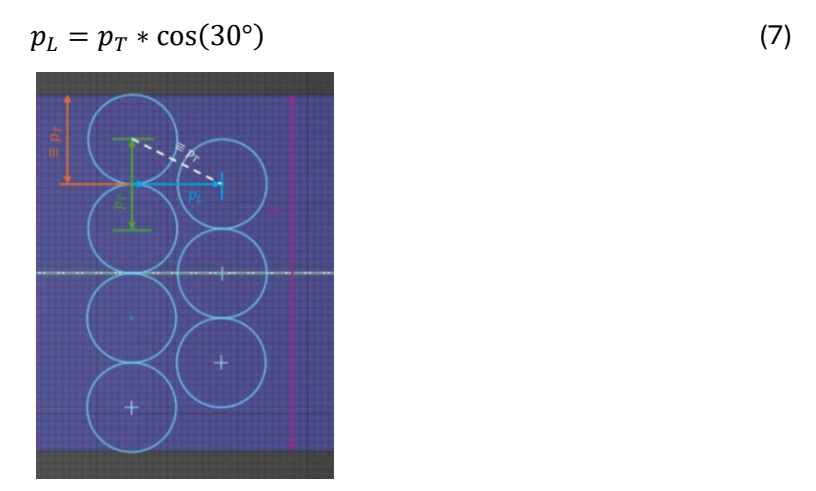


Figure 5: Geometry construction of the array of cylinders.

In this way the only free parameters are N and the radius of the cylinders of the six columns.

#### 3.1.2 Mesh generation

The flow is wanted to be well-described between the cylinders and on them, for this reason inflation layers have to be used on their surfaces, and they are evaluated as described in Section 2.4.1. The mesh parameters are the following:

Table 5: Mesh settings for the array of cylinders.

Туре	Local refinement	Location	Values [mm]
Surface mesh	/	All the surfaces	0,5-4
	Face-size	Cylinders' surfaces	0,5
		Cylinders' surfaces, a	2*10 <sup>-3</sup>
Inflation layers	First Height	Cylinders' surfaces, b	1,75*10 <sup>-3</sup>
	Size	Cylinders' surfaces, c	1,75*10 <sup>-3</sup>
		Cylinders' surfaces, d	1,25*10 <sup>-3</sup>

		Cylinders' surfaces, e	0,75*10 <sup>-3</sup>		
		Cylinders' surfaces, f	0,75*10 <sup>-3</sup>		
Volume mesh	/	All the volume	4 (polyhedral, growth 1,25)		

The number of inflation layers are in every location 25 with a transition ratio of 0,3, concerning instead the surface mesh the growth rate is 1,2. The mesh generated with these settings is shown below:

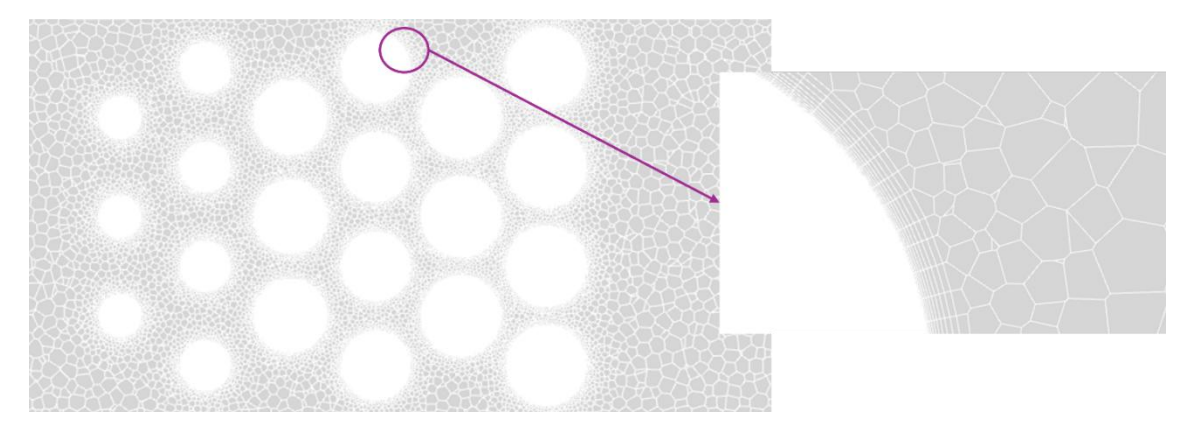


Figure 6: Mesh generation on the plane YZ with x=0 with inflation layers zoom.

The criteria for y<sup>+</sup> are satisfied and it can be seen with a contour of it on the walls:



Figure 7: y<sup>+</sup> contour on the cylinders.

As it is shown y+ is greater than 1 only on the conjunction between the main pipe and the cylinders, this because, as explained in Section 2.4.1.1, the main pipe has not inflation layers.

### 3.2 Design and hydraulic results

#### 3.2.1 Design

The design of this configuration of obstacles is obtained by some trials on the values of the diameters and the number of cylinders. It is important to have a minimum diameter of the cylinders of about 9-10 mm to not have problems concerning the vibrations during the crossflow.

The firsts attempts were done with a triangular staggered layout based on a N of 6, but these configurations take to have very high pressure drop.

The second trial was done with N equal to 5 and with diameters of the cylinders between 9 and 15 mm. In this way the maximum velocities were closer to the targeted values.

The next step was to construct the triangular staggered layout with N of 4 and, based on the flow area evaluated before, the diameters of the new cylinder columns were evaluated. Then an iterative process is pursued to refine better the diameters considering the maximum velocities achieved in a common area, the flow area of each column at the intersection of the centres of the cylinders (where usually is expected the maximum velocity of the column). This procedure is called One Factor At Time and it is well explained in Section 2.3.1. Some of the design points are reported here below:

Table 6: Design points of the array of cylinders, where R is the radius of each column expressed in mm and V the maximum velocity registered in m/s.

DESIGN POINT	R <sub>a</sub>	$R_{b}$	R <sub>c</sub>	$R_{d}$	$R_{e}$	$R_{f}$	$\mathbf{V}_{a}$	$V_{b}$	<b>V</b> <sub>c</sub>	$V_{d}$	$V_{e}$	$V_{f}$
1												
2	4,5	6	8,5	8	9,5	9	1,4961	2,2286	2,5262	3,0748	3,4642	3,7986
3	4,5	5,5	8,5	8	9,5	9,5	1,4788	2,1562	2,5035	3,0.128	3,4355	4,2096
										3,0432		
										3,0515		

To have the lowest possible velocity with this configuration it is decided to put the lower number of cylinders of the configuration at the beginning of the array.

The chosen configuration is the following:

Table 7: Final configuration of the cylinders' array.

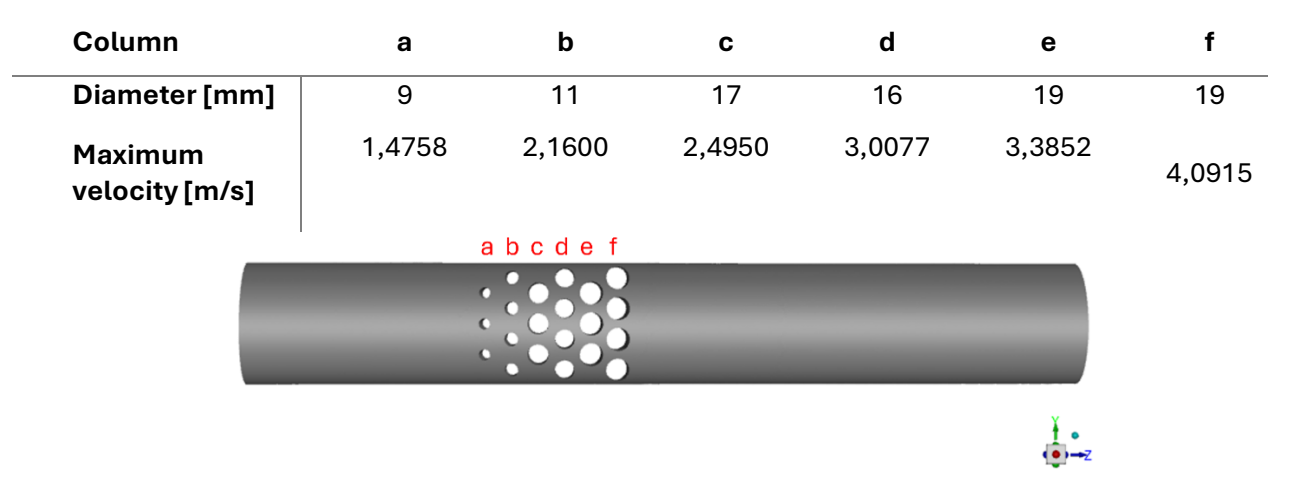


Figure 8: Final geometry of the array of cylinders.

#### 3.2.2 Hydraulic

#### 3.2.2.1 Hydraulic requirements

Because the design is based on the velocity as output parameter, it is necessary to look how its field is developed and especially between the cylinders:

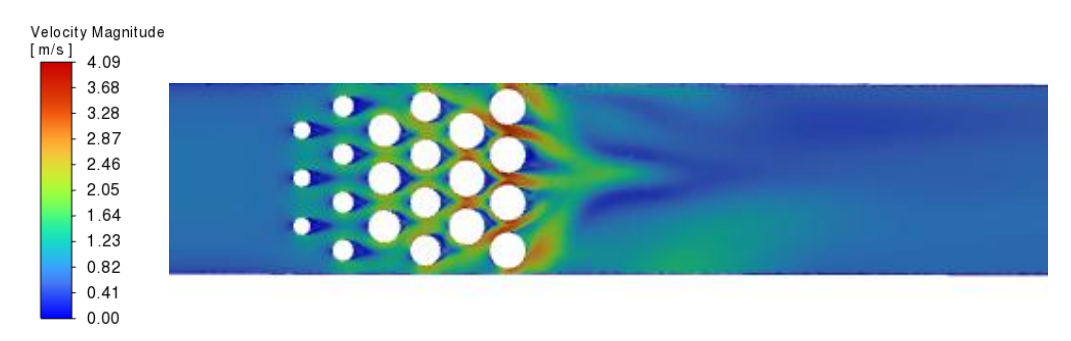


Figure 9: Velocity contour on the YZ plane at x=0 of the array of cylinders.

As expected, the maximum velocities are registered in between the cylinders of the same column, and this velocity contour shows also how behind the cylinders the recirculation zone is formed. Usually, the recirculation zone studied with only one cylinder is two diameters long [14], in this case it is lower because the influence of the following cylinders' columns.

It is also important to compare to two hydraulic limits on velocity and pressure: the velocity has not to overcome 5-6 m/s while the pressure has to be under 1 bar for this configuration. As can be seen in the Figure 9 the velocity maximum value is around 4 m/s which means that the limit is not exceeded. To evaluate the pressure drop it is plot of the static pressure along the plane YZ in x=0 is done:

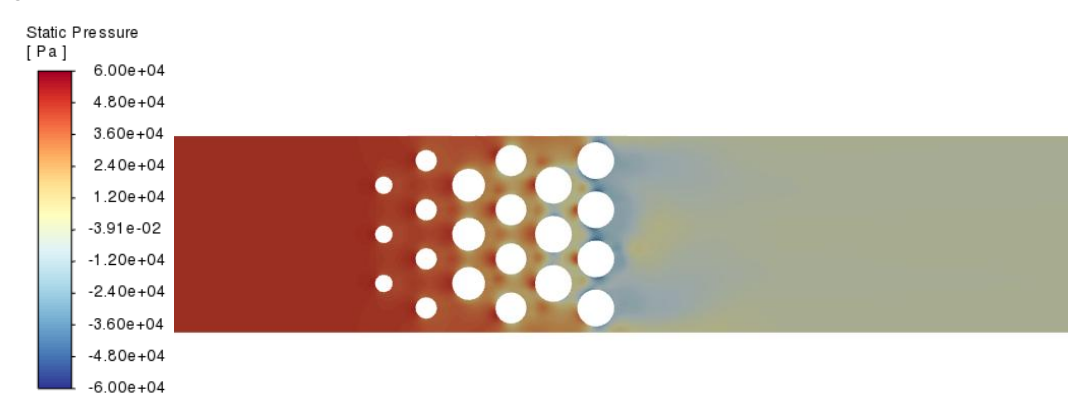


Figure 10: Contour plot of the static pressure on the YZ-plane at x=0 of the array of cylinders.

The pressure reaches a maximum of almost 0,6 bar, which is acceptable, while its distribution along the tube and in between the array of cylinders is perfectly coherent with the physics. Low-pressure regions can be observed downstream of each cylinder, due to flow separation and the formation of wake zones. This configuration therefore ensures that pressure levels remain within acceptable limits, but also produces a physically realistic pressure distribution, confirming the reliability of the adopted simulation model.

#### 3.2.2.2 Hydraulic results

#### 3.2.2.2.1 Velocity distribution

Always concerning the velocity, it is possible to understand something about the flow behaviour with the velocity vectors:

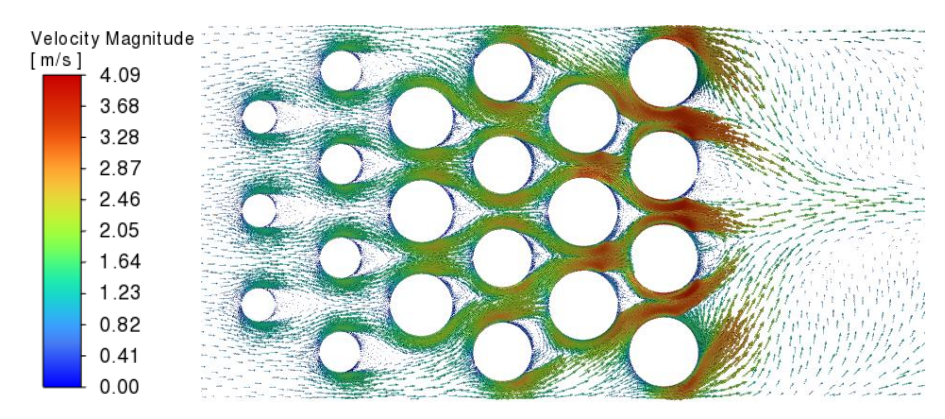


Figure 11: Velocity vectors on the YZ plane at x=0 of the array of cylinders.

In the last columns the recirculation zone is no more perfectly symmetric compared to the cylinder itself as in the first two columns, in fact it is strongly deformed by the jets created by the previous columns and the ones adjacent. This can be an indication of the unstable flow behind the last column (Von Karmann swirls).

Because the velocity reaches the maximum ranges of value in the restriction between each column it is interesting to see the distribution of the velocity profile along these planes:

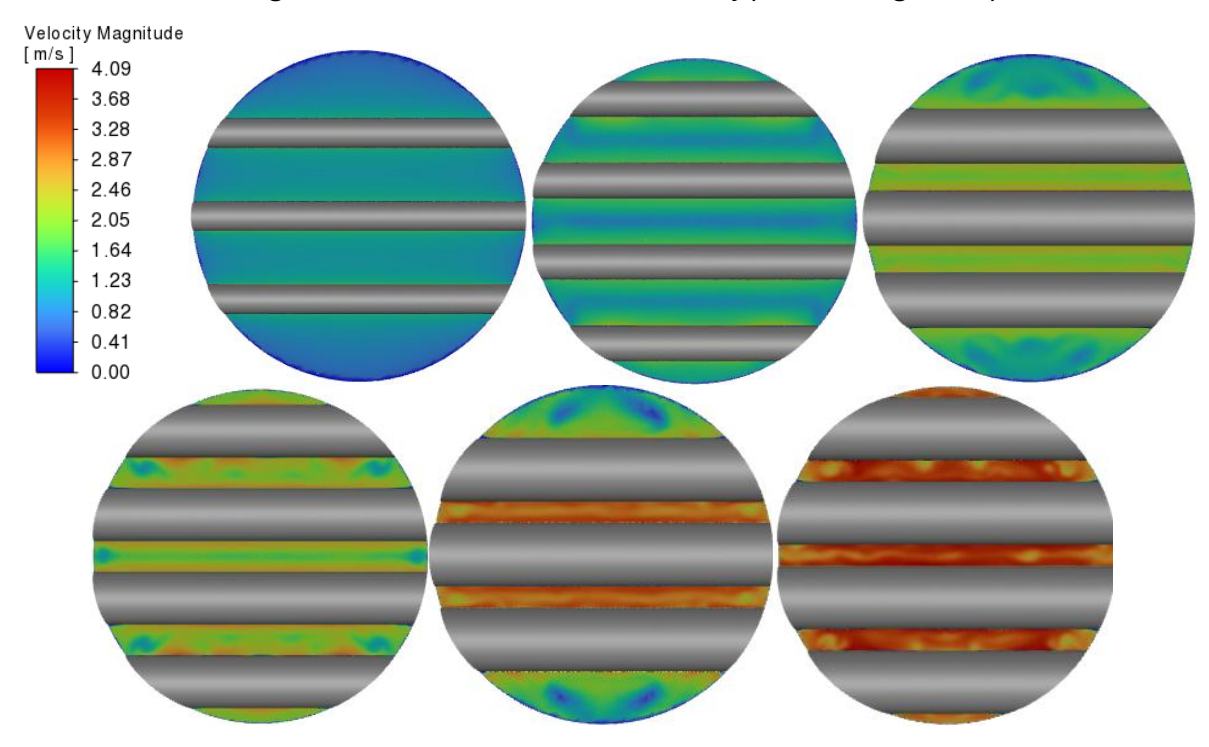


Figure 12: Velocity profile on the planes XY at z equals to the centres of symmetry of the columns of pipes.

From the above XY velocity profiles and the YZ vector plot in Figure 11, it is clear that in the first few pipe columns, the velocity distribution is relatively uniform and undisturbed, with well-defined high-velocity regions between the pipes. However, as the flow progresses downstream along z, wake interactions and turbulence become increasingly dominant. The last few columns show higher levels of velocity fluctuations, with broader wake regions and a more chaotic velocity field. This transition reflects both the cumulative pressure loss and the enhanced mixing caused by repeated flow separations and vortex shedding.

#### 3.2.2.2.2 Turbulence distribution

It is very important to understand the amount of the turbulence parameter and how it develops inside the geometry. Below it is possible to look at the TKE plot along YZ and the information from this plot can be easily coupled with the information of Figure 9:

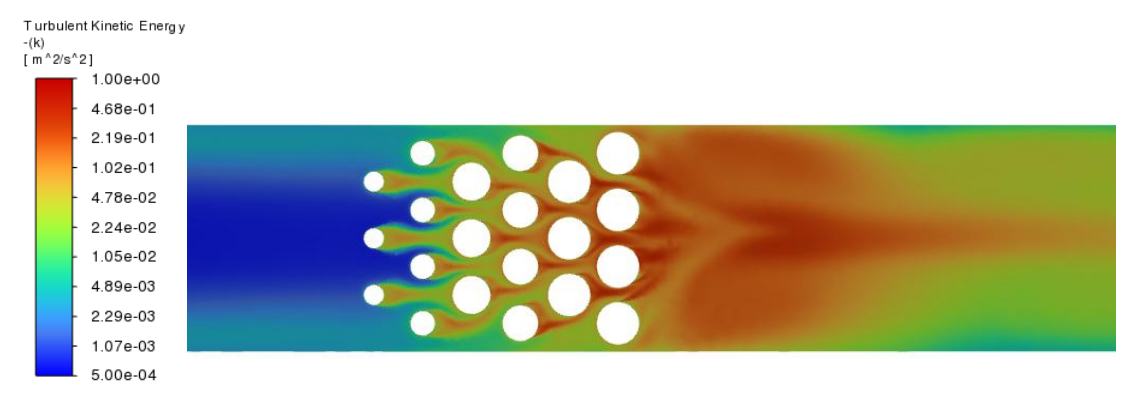


Figure 13: Contour plot of the TKE on the YZ-plane at x=0 of the array of cylinders.

The TKE distribution shows strong and extended regions of turbulence downstream of the cylinders, especially in the central area, where interactions between wakes are most intense. The velocity plot further supports this by displaying broad, low-velocity wake zones and significant asymmetry, indicating strong flow separation and deflection. These patterns confirm that reverse flow across the array enhances turbulence generation while significantly diminishing the momentum of the flow downstream.

It is also necessary to plot the streamlines of the flow to look if and where the flow can reattach to the surfaces of the cylinders. Lines creating vortex are produced only at the end of the configuration so where the column f is placed:

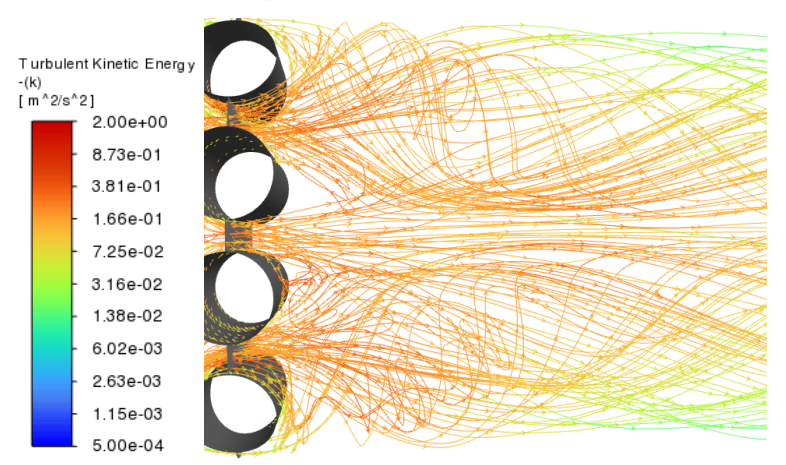


Figure 14: Path-lines of the TKE after the last column of cylinders.

Here near the wall of almost all the four cylinders the flow is turning back towards the surfaces, and this can create an enhancement of the erosion corrosion.

#### 3.2.2.2 Shear stress distribution

These information on the velocity are important because the acceleration of the velocity is the driving force of the wall shear stress increasing on the cylinders' surfaces.

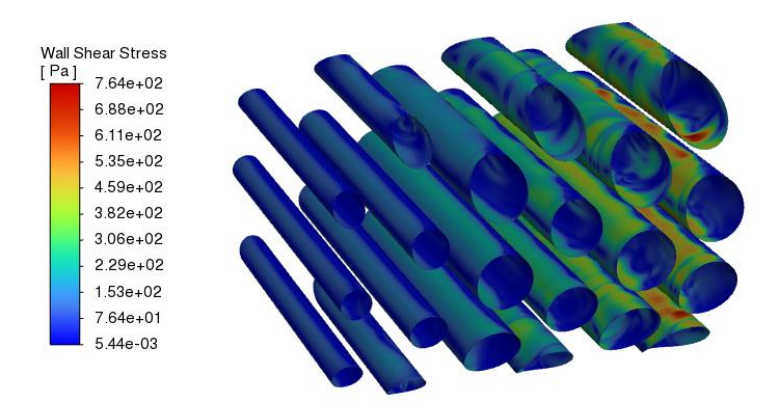
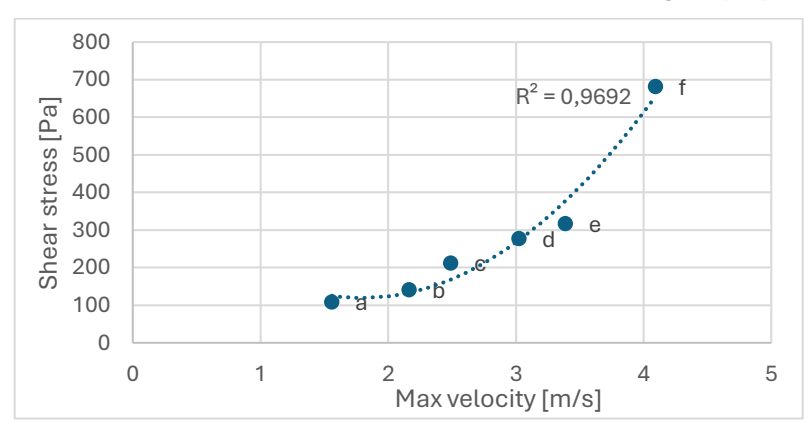


Figure 15: Wall shear stress on the cylinders array surfaces.

As can be seen by Figure 15 the wall shear stresses are really low behind the cylinders compared to the values in the flow direction, corresponding to the recirculation zone. This is expected because there the velocity is near to zero. The shear stress instead increases a lot on the last columns because the flow accelerates along the direction of the flow itself: a higher magnitude of the velocity takes to have a higher gradient of it along the vertical direction because what change is only the maximum value of the velocity itself, while the minimum velocity in every surface is zero thanks to the wall condition. In this way the maximum shear stress is located obviously in the last column, and it is equal to 764 Pa.

Because the wall shear stress is not directly related to the velocity, but it is proportional to the gradient of it in the perpendicular direction compared to the surface, the maximum shear stress and the maximum velocity could be not located in the same point. In fact, it is what happens, and it can be shown that for each column of cylinders, where is located the maximum velocity the corresponding wall shear stress is well related to it with a second-degree polynomial:



Graph 1: Wall shear stress function of the maximum velocity evaluated for each column of cylinders.

This can happen when the jets influence the behaviour of the entire flow, as happens here.

Concerning the pressure drop it is about 0,46 bar, which is considered acceptable considering that the request done for the entire design configuration of all the obstacles is 2 bar.

### 3.3 Numerical results

## 3.3.1 Convergence

As said in section 2.2.6 Numerical analysisthe convergence criteria are set for all the variables of the method at 0,001, but not all of them reach it. In fact, as illustrated in Figure 16, the turbulence kinetic energy k stabilises only at  $2*10^{-2}$  as residual; it is an expected behaviour of k because it is directly linked to the fluctuations of the velocities and it is strictly not linear, so it is more difficult for this parameter to converge numerically. Figure 16: Residuals of the steady state simulation of the array of cylinders.

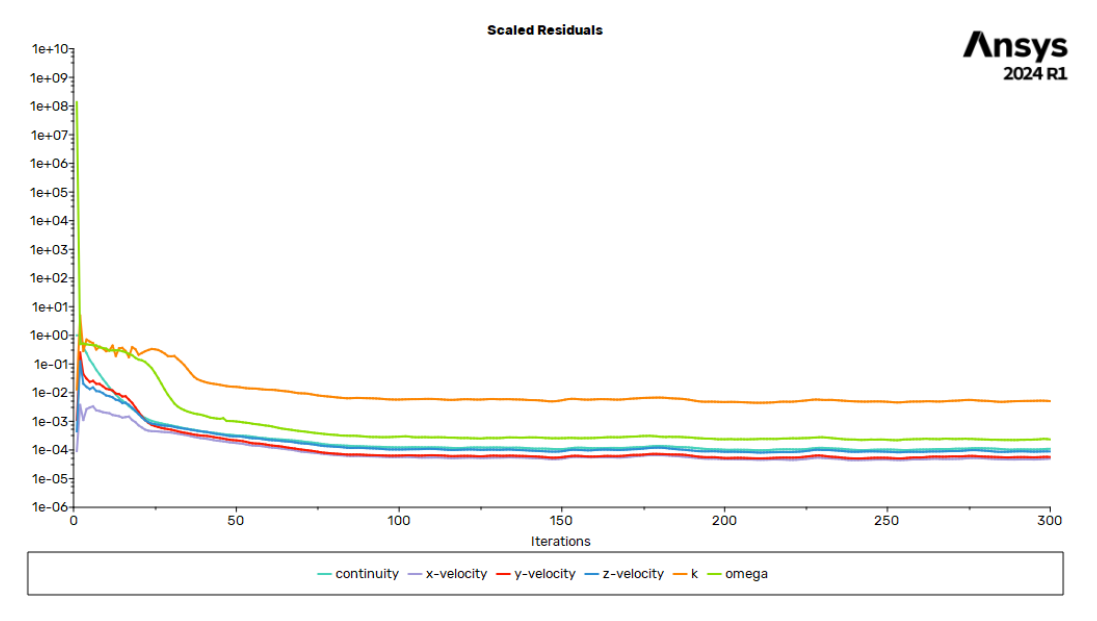


Figure 16: Residuals of the steady state simulation of the array of cylinders.

But the stabilisation of the values of the residuals after almost one hundred iterations suggest that the solution reach a quasi-stationary state acceptable for the scope and it can be confirmed from the stabilisation of the physical properties such as the pressure. In fact, can be seen that the pressure reaches a stable value of around 46038 Pa also around the one-hundredth iteration.

## 3.3.2 Grid independence analysis

To understand if the problem is not influenced too much by the grid and so a general solution is achieved, a grid independence analysis is done. Other two meshes are considered, one finer and one coarser. A remark must be made because in the case studied it was quite expensive computationally to re-fine the mesh. It is not possible to reduce the general cell size by a factor of 2 for different meshes. Because of that it is necessary to scale the mesh parameters of the following value:

$$x = \left(\frac{\text{memory of the pc}}{\text{memory in use by Fluent during the case study simulation}}\right)^{\frac{1}{3}}$$

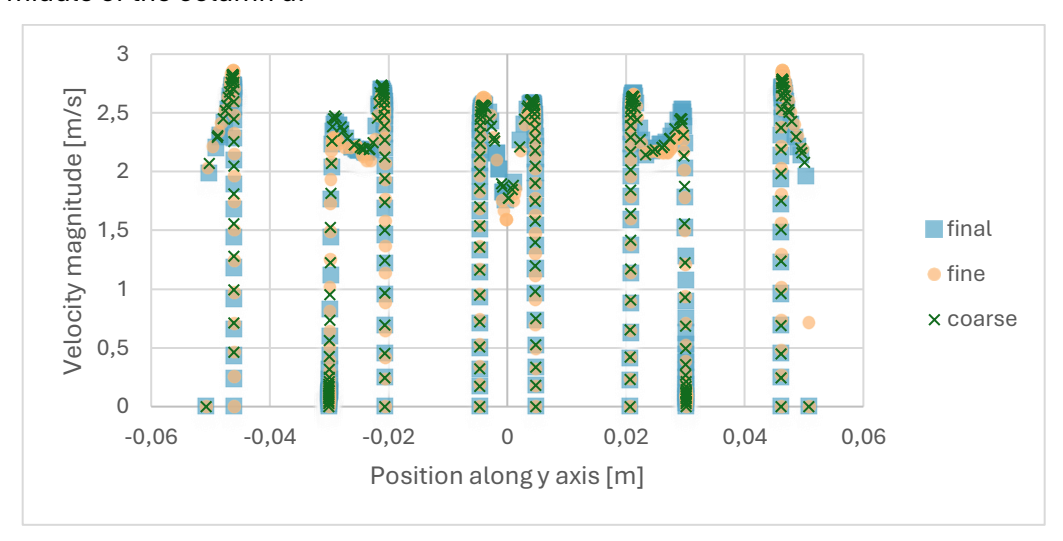
The third square is from the fact that the problem is in 3-dimensional. In this way the memory of the pc is not overcome, and the simulation can run. In the case of the problem here studied x is equal to 1,25. The three meshes are generated with the following parameters:

Table 8: Mesh independence parameters of generation.

	Surface mesh	Face-size	Volume mesh
Case-study	0,5 - 4 mm	0,5 mm	4 mm
Fine	0,4 – 3,2 mm	0,4 mm	3,2 mm
Coarse	0,625 - 5 mm	0,625 mm	5 mm

The inflation layers are not modified to not influence too much the y+ values reached.

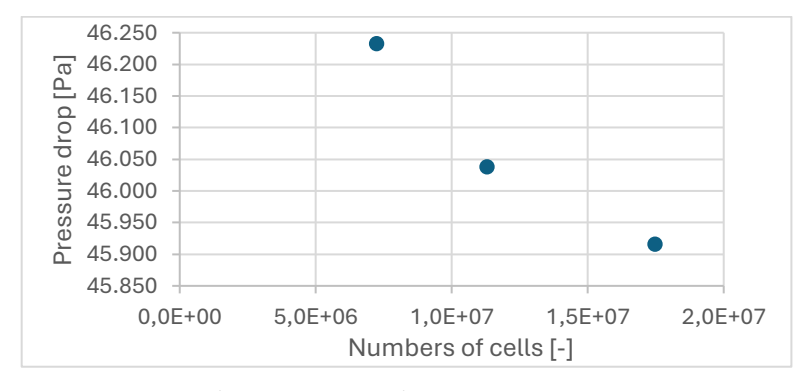
Now what can be interesting to see is how the results are impacted by these changes on the mesh. To do that it is possible to plot on a xy-diagram the velocity profile of the flow on the cross-section in the middle of the column d:



Graph 2: Velocity profile along column d cross-section with three different meshes: the case study (final), the fine and the coarse ones.

As can be easily understood, the results do not vary much on the different meshes and they are almost the same near the wall; this last observation means that the inflation layers can achieve in a good way the gradient of the velocity and they show slightly more variation in between the cylinders where the cells are coarser.

As written in Section 2.2.6, it is necessary only to compute an interesting quantity, as can be in this case the pressure drop, and look how it changes for the three generated grids to evaluate the grid independence. This can be evaluated in the following graph:



Graph 3: Pressure drop along the cylinders' array function of the number of cells through the mesh refinement.

The change is decreasing monotonic with the increasing number of cells, and this means that the solution is converging to the mesh independence. The changes of the pressure drop between the different meshes is only less than 1% (400 Pa / 46000 Pa).

Because of these results the conclusion that the solution is grid independent can be reasonably confirmed.

## 3.4 Unsteady nature of the problem

One of the extensively and basic engineering problems is the flow around a singular circular cylinder. This case study is of particular fluid-dynamic interest, because from it some important phenomenon rise, like turbulent transition, separation of the flow and vortex shedding [15].

These interesting phenomena take to have a challenging problem to solve from a CFD point of view, and when there is no more only one cylinder, but a bundle like in this study, the flow is more difficult to characterise. In fact, from a singular cylinder in backflow under steady flow, it is expected a well-known behaviour which is function of the Reynolds number. Different regimes can take place, as can be seen in Figure 17, influenced by the impact of the vortex shedding: a vortex street is formed in the wake region where vortices take place and they shed, inducing pressure variations in the structure [16].

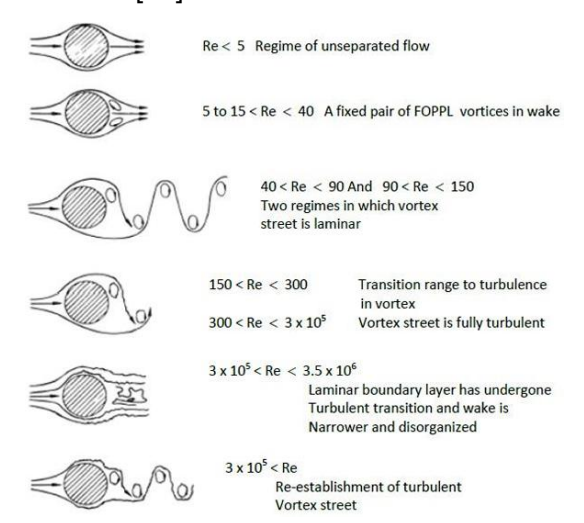


Figure 17: Regimes of fluid flow across a circular cylinder [17].

In this work, the Reynolds characterising the pipe is around 1,2\*10<sup>5</sup>, so the vortex in the case of a single cylinder, is fully turbulent and it is well defined by Von Karman (Karman vortex) and they have a periodic behaviour in the shedding and so also in the pressure variations.

The vibrations can be in parallel and transverse direction compared to the flow and they are characterised by a well-known frequency called "vortex shedding frequency",  $f_w$ . This frequency can be expressed by the dimensionless Strouhal number as follows:

$$Sr = \frac{f_w * L_{characteristic}}{v}$$

Where v is the velocity of the flow [16]. This dimensionless number represents the ratio between inertial forces due to local acceleration, and so the unsteadiness, and convective inertial forces, due to point-to-point velocity variation. It is a very important coefficient to solve an unsteady and

oscillating problem, because it has been established for a wide range of case studies and from it is possible to determine  $f_w$ .

As said before, in this work the problem is more complex than the one explained above and so it is not possible to assume a priori the behaviour of the flow. Because of that it is necessary to simulate this unsteady problem and evaluate how the steady-state and the unsteady solutions differ between them.

### 3.4.1 Unsteady simulation setup

This analysis, as the numerical one, is done considering only the array of tubes geometry, again for a computational cost reason.

The Strouhal number introduced in the section before is interesting in this analysis because it is well-studied for different configurations and situations. In the study pursued by Xi et al. [18], a cylinders' array like the one described in this work is evaluated. Also, if the two cases have not the same configurations and flow conditions, a first evaluation of the Strouhal number can be taken to have an order of magnitude of it, and for Xi et al. it is equal to 0,2. In this way a frequency of 1,57 Hz is calculated, which means a period of 0,635s and considering that the guide of Ansys recommend having 20 iterations every oscillation, the time interval of simulation becomes the following:

$$\Delta t = \frac{0,635}{20} \sim 0,03 \ s$$

For the setup of the transient simulation the following actions are considered:

- The solver is switched from Steady to Transient;
- The initial condition is taken as the steady state one;
- The methods for the Pressure-velocity Coupling are set to SIMPLE, as recommend by Ansys Fluent guide for small  $\Delta t$ ;
- The number of steps for interval of time is set to 20.

Then a good consideration to do is to evaluate the amount of time that the fluid control volume stays inside the pipe before completely exit, it is called "residence time". The residence time in the simulation is around 8 s, so it is interesting to simulate a little bit more than this time. For this reason, and to wait the formation of the oscillations of the transient, is simulated a time of 12 s.

## 3.4.2 Unsteady solution

The results for the unsteady solution can be represented in numerous ways: with "unsteady statistics", which Fluent evaluates the properties as an average in time, or with the values in any time interval.

It is interesting to see how the velocity profile change in time, as can be seen in these figures:

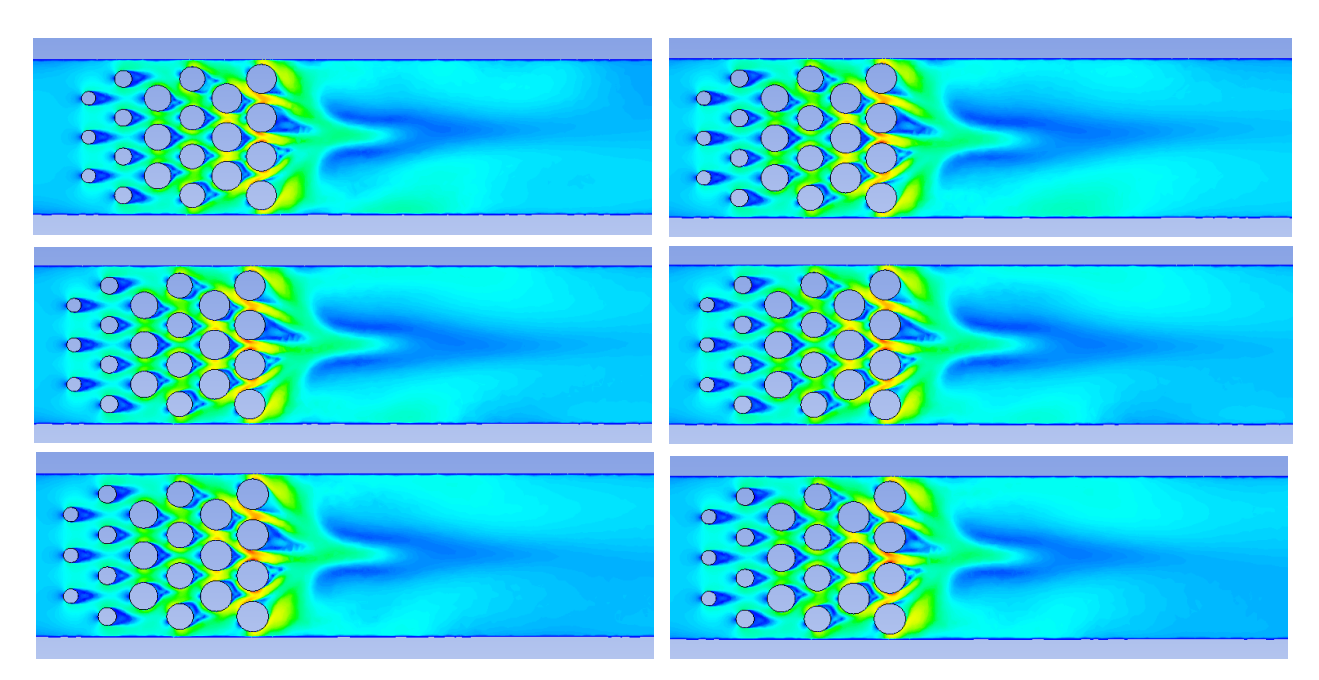


Figure 18: Evolution in time of the velocity profile along YZ plane. From top left to right: 0,3s, 2,7s, 5,1s, 7,5s, 10,2s and 12s.

The behaviour is not periodic as expected, thanks to the influence of all the cylinders on each other. It is interesting to note what happen behind the last column: here the vortices are created but eventually stabilise.

It is necessary to confront the results of the steady state and unsteady simulations to understand what condition and values consider to properly design the test section. Because of that the following diagram is constructed, where the velocities are evaluated as the maximum in each middle cross-section of the columns:

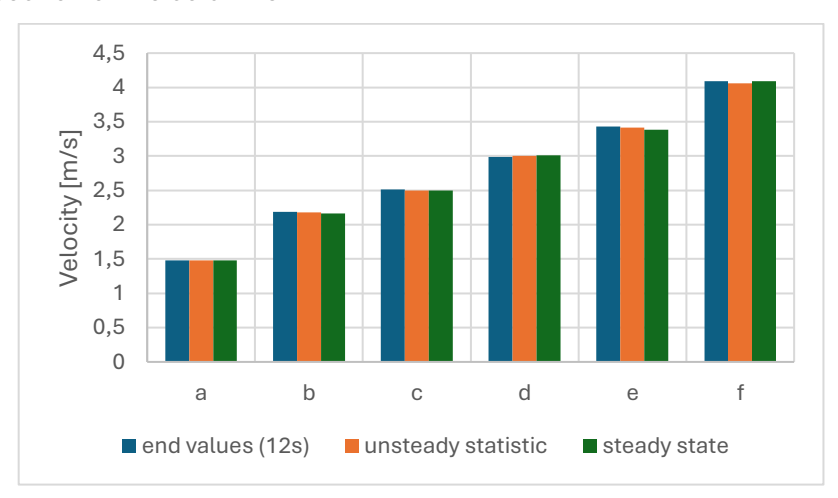


Figure 19: Velocities evaluated as the maximum in each middle cross-section of the columns.

As can be seen the target velocities are not significantly affected by the fluctuations: the evaluation done on the steady state assumption can be taken as valid for the case study.

# Chapter 4 – Plates with holes

The geometry represented by the plates with holes is studied to analyse the effects of acceleration of the flow in holes, which is a very impacting phenomenon. In fact, this phenomenon affects the same holes and in particular the restrictions, but also what stays behind them thanks to the strong jets created.

This is a classical geometry studied since plate with holes and grids are usually common in every field. In fact, they are used to homogenise the flow and to increase the pressure drop when the space is little to create certain flow distributions within difference parts of the reactor core to obtain more homogenous core outlet temperatures.

## 4.1 Simulation setup

## 4.1.1 Geometry

As said previously, this geometry is known to create high pressure drop and due to the imposition of the limit of 2 bar on the entire test section, it is needed to be careful. Because of that, two main ways to design the plates with holes can be taken into account:

- 1. Plates with a high number of holes with small diameters;
- 2. Plates with a low number of holes with larger diameters.

As previously mentioned, it is useful to study what happens behind the grid, where strong jets are created. These jets are a consequence of this design but also an opportunity in this case because the objective of this study is to understand what happens under critical conditions. To take advantage of these jets it is important to have after them a solid wall to study the shear stress and the pressure drop; to obtain this other plates with holes not aligned with the previous one are created: where there are the holes in the first one, in the second has to be present the plate's wall.

Between the two plates it is taken as general design parameter a distance equivalent to the hole diameter.

#### 4.1.1.1 Geometry of the Design I

With this configuration it is chosen to have regular triangular pattern of holes in each *plate A* and the second one is shifted compared to the first one to achieve what said before.

To design the centres of each hole it is considered a diameter of 8 mm, which means that maximum twelve holes can be aligned along the cross section of the tube. Considering that between each couple of holes in the previous plate in the following one a hole must be present; it is possible to have the result illustrated in Figure 20. A minimum distance from the border is defined and evaluated as follows:

$$\frac{101,6 \ mm - (8 \ mm * 12 \ holes)}{2} = 2,8 \ mm$$

Figure 20: Initial configuration to create the pattern, in yellow the one for the plate A and in blue for the plate B.

With the tool "Fill Pattern" with option "Offset" are created the designs of the plates as explained.

#### 4.1.1.2 Geometry of the Design II

To ensure that solid wall sections in *plate B* correspond to hole locations in *plate A*, it is necessary to create a specific configuration considering that the diameter of the holes now will be much higher than before. If four holes are selected for *plate A* and three for *plate B*, to maximize the number of jets studies on the inlet of *plate B*, a geometry like the following one can be designed:

- holes at the vertices of two triangles, one in *plate A* and one in *plate B*, reversed compared to each other but with the same centre;
- an additional hole is added to *plate A*, located above or below the hole at the upper vertex of its triangle.

In this way the holes do not overlap or, if the radius of the holes is high, the overlapping is limited.

## 4.1.2 Mesh generation

In these geometries it is wanted to analyse the impact of the radius of the holes and of the restrictions and the typologies of the latter, but also what are the effects on the surface of the plates itself. Because of that, both the plates and the holes have to be described through the use of inflation layers and the construction of the mesh follows what it is said in Section 2.4.1.

#### 4.1.2.1 Mesh of the Design I

The generated mesh has these parameters of surface and volume mesh:

Table 9: Mesh settings for the Design I of plates with holes.

Туре	Local refinement	Location	Values [mm]
Surface mesh	1	All the surfaces	0,5-6
	Face-size	Plates and holes surfaces	1
	Face-size	Restrictions' surfaces	0,1
	Edge-size	Sharp edge A	0,1
	Edge-size	Sharp edge B	0,05
		Plates and holes surfaces in A	4,5*10 <sup>-4</sup>
Inflation layers	First Height Size	Plates and holes surfaces in B	3,5*10 <sup>-4</sup>
iintation tayers	Filst Height Size	Restrictions' surfaces in A	6,5*10 <sup>-4</sup>
		Restrictions' surfaces in B	5,5*10 <sup>-4</sup>
Volume mesh	/	All the volume	6 (polyhedral, growth 1,25)

In this case the Maximum Size of the surface mesh and the Maximum Cell Length of the Volume Mesh  $(S_n)$  are taken as the minimum size of the geometry, while Minimum Size of the surface mesh as one hundred times  $S_n$ . This variation is done because the first layers of the inflations are really low, and it takes to have very small  $S_n$ .

The number of inflation layers is 10 with a transition ratio of 0,272, concerning instead the surface mesh the growth rate is 1,2.

The inflation layers on the plates and holes have also as advanced options:

- "Ignore Boundary Layers At Acute Angles: NO", to have completed boundary layers also on narrow edges;
- "Modify Surface Mesh At Invalid Normals: YES", to obtain uniform normal along which the inflation layers are constructed, also where the normal changes abruptly.

#### The result of it is the following:

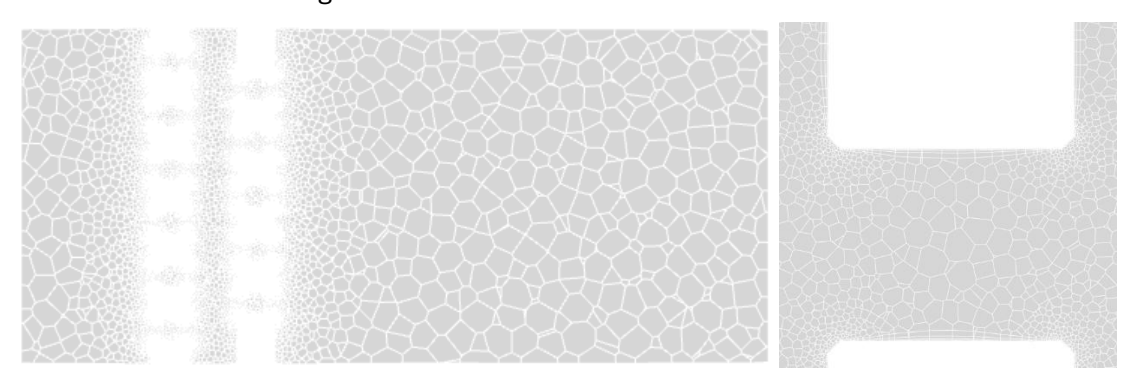


Figure 21: Mesh generation on the plane YZ with x=0 on the left of the first design of plates with holes, zoom on two holes on the right.

#### The quality of the mesh is resumed here:

Table 10: Quality mesh parameters of the first design of plates with holes.

Quality mesh parameter	Recommended values	Actual values
Skewness	< 0,7	0,61
Minimum orthogonal quality	0,1	0,004
Orthogonal quality	> 0,1	0,884

The only value which does not compared to the recommended values is the minimum orthogonal quality, but it is underlined the localization of this bad quality, and it corresponds to the connection between plates and principal tube which has not inflation layers and where the information is not interesting in the pursuit of this analysis.

The  $y^+$  requirements for the k- $\omega$  SST turbulence model have been satisfied by iteratively refining the mesh, specifically by adjusting the first layer thickness based on the maximum wall shear stress observed, as explained in Section 2.4.1:

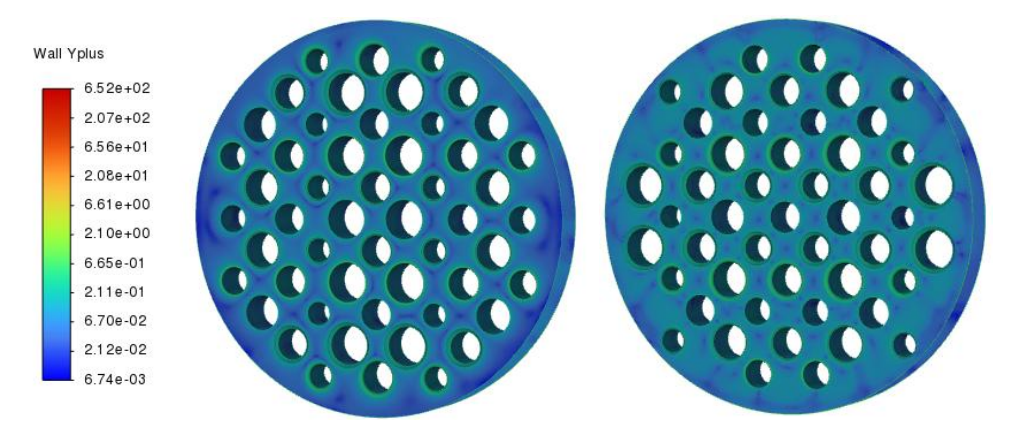


Figure 22: y+ contour of the plate A on the left and on the plate B on the left for the first design.

### 4.1.2.2 Mesh of the Design II

The mesh parameters are the following:

Table 11: Mesh settings for the Design II of plates with holes.

Туре	Local refinement	Location	Values [mm]
Surface mesh	1	All the surfaces	0,2-6
	Face-size	Plates and holes surfaces	0,2
	Face-size	Restrictions' surfaces	0,1
	Edge-size	Sharp edge A	0,1
	Edge-size	Sharp edge B	0,05
		Plates and holes surfaces in A	5*10 <sup>-4</sup>
Inflation lavora	First Hairle Cina	Plates and holes surfaces in B	4*10 <sup>-4</sup>
Inflation layers	First Height Size	Restrictions' surfaces in A	5*10 <sup>-4</sup>
		Restrictions' surfaces in B	4*10 <sup>-4</sup>
Volume mesh	/	All the volume	6 (polyhedral, growth 1,25)

The same comment of Design I can be done also here for the inflation layers and for the sizes.

The mesh generated with these settings is shown below:

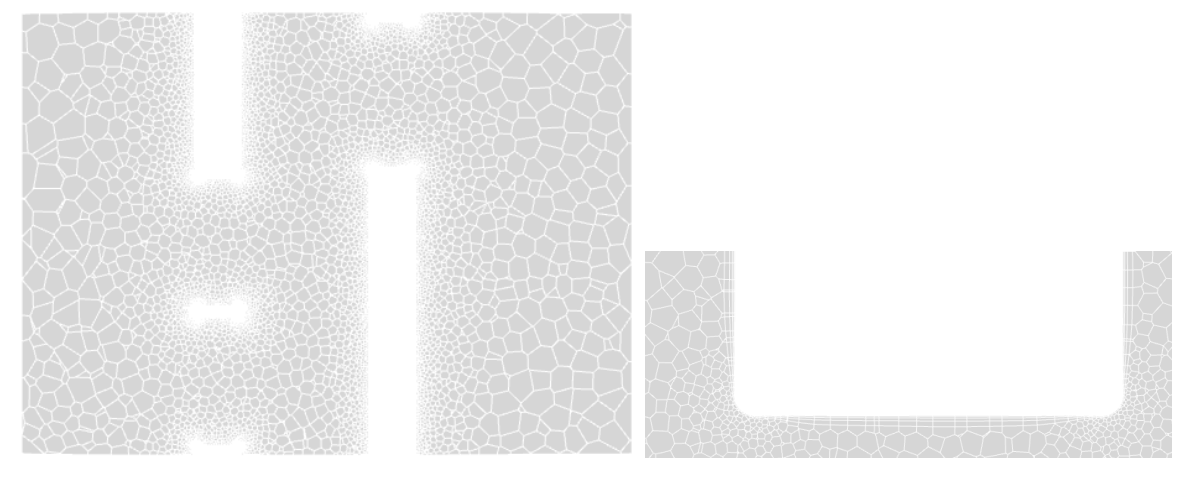


Figure 23: Mesh generation on the plane yz with x=0 on the left of the second design of plates with holes, zoom on hole 3 on the right.

The quality parameters for this mesh generation are the following:

Table 12: Quality mesh parameters of the second design of plates with holes.

Quality mesh parameter	Recommended values	Actual values
Skewness	< 0,7	0,57
Minimum orthogonal quality	0,1	0,07
Orthogonal quality	> 0,1	0,91

Again, the minimum orthogonal quality is lower than the recommended one as before but, compared to the Design I, here the values is very near the limit and it is acceptable.

It is also interesting to see how the surface mesh is generated on the different holes' restrictions:

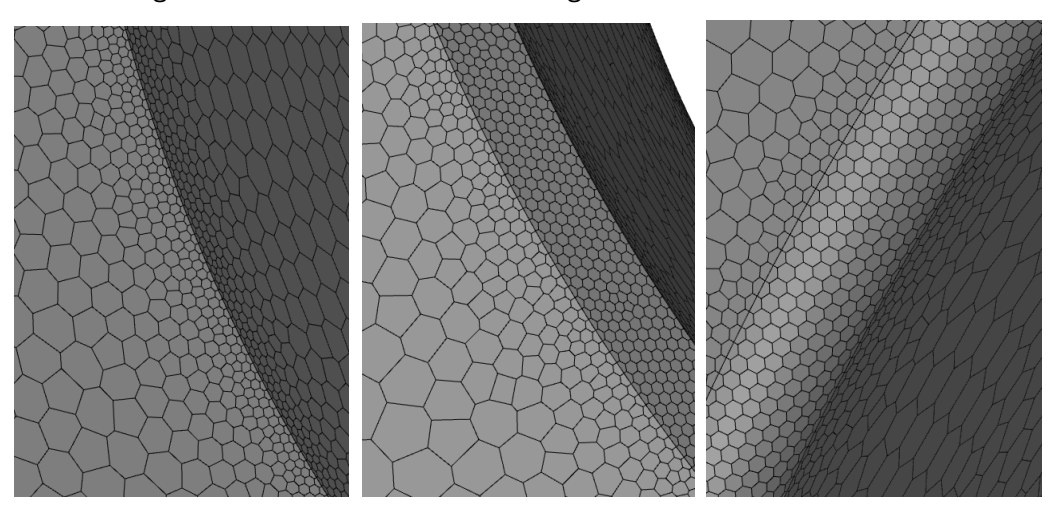


Figure 24: Surface mesh of the different types of edges, respectively sharp, chamfer and rounded on the plate A.

The sharp edge has cells of 0,1 mm around the border, while the rounded and the chamfer has cells of the same size in all their surface: the edge-size and the face-size worked correctly.

Remembering the criteria for the  $k-\omega$  SST on  $y^+$ , it is satisfied thanks to the iterations done on the maximum stress registered and the first layer height modification.

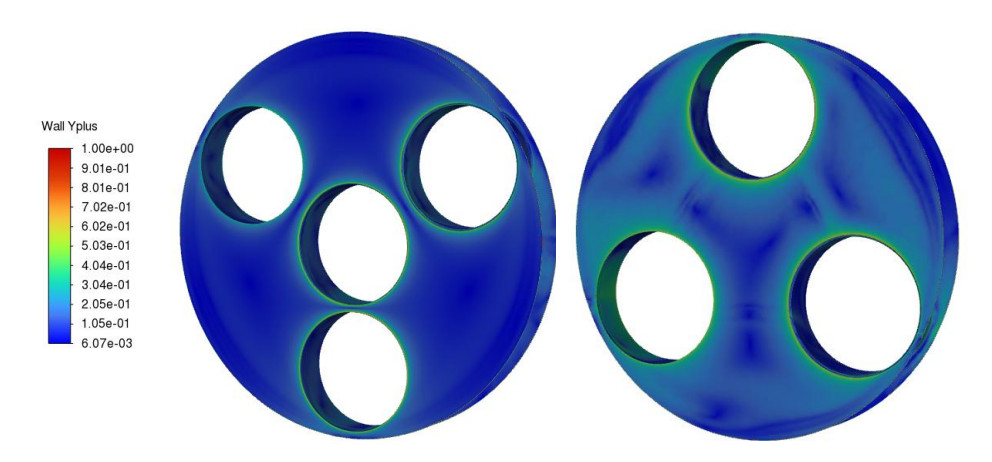


Figure 25: y+ contour of the plate A on the left and on the plate B on the left for the second design.

## 4.2 Design I: high number of holes, small diameters

For both the designs of the plates with holes the analysis is done without the use of DOE method, because here the goal are not hydraulic results but understand the behaviour of the flow on the different holes remaining in certain hydraulic limits. These limits are in velocity, trying to not increase the velocity up to 5-6 m/s, and in pressure, remembering that the total pressure drop of the test-section has to be maximum 2 bar. Because of that some diameters of the holes are evaluated; the limits are controlled to not be overcome and then a deeper study is done on the effects of the flow on the geometry.

## 4.2.1 Design results

Here it is interesting to analyse how the restriction can affect the velocity acceleration and the shear stresses. Due to that the diameter of the holes is changed in a range of  $\pm$  25% and the restrictions are changed in type and radius.

Table 13: Changes of the holes' diameter in the plates.

#### Diameter changes [mm]

Plate	Column 1	Column 2	Column 3	Column 4	Column 5
Α	7	9	8	6	10
В	10	6	8	9	7

Table 14: Changes of the type and the radius of the restriction in the plates. The types are represented as R for the rounded one, C for the chamfer and E for the original Edge.

#### Restriction changes [-; mm]

Plate	Row 1	Row 2	Row 3	Row 4	Row 5
Α	R; 1	C; 1	Е	R; 0,5	C; 0,5
В	R; 0,5	C; 0,5	Е	R; 1	C; 1

Along the main column and the main row, the holes remain unchanged.

The two grid's scheme can be represented as follows:

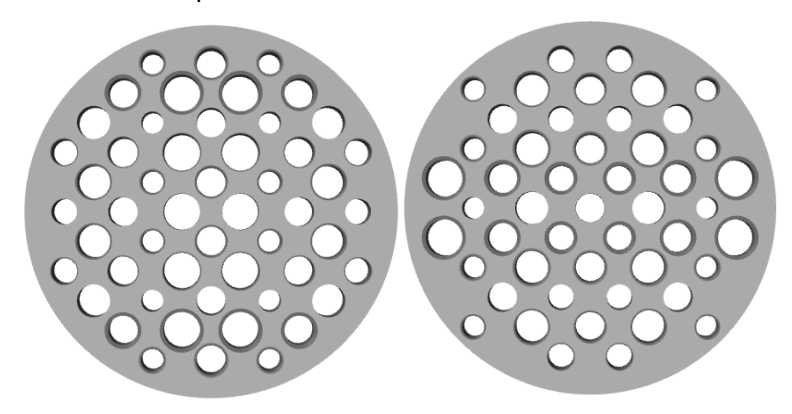


Figure 26: Plates with holes' first designs, respectively plate A and B.

### 4.2.2 Hydraulic results

#### 4.2.2.1 Hydraulic limits

The first thing to do after having built the CAD of the design is to control the hydraulic limits imposed for the geometry.

As first thing, for the plates with holes, it is important to understand how much the pressure drop is and here it is evaluated as area weighted on the inlet: it is about 0,45 bar. It can be also visualized through a contour plot of the static pressure on the plane along the length of the geometry:

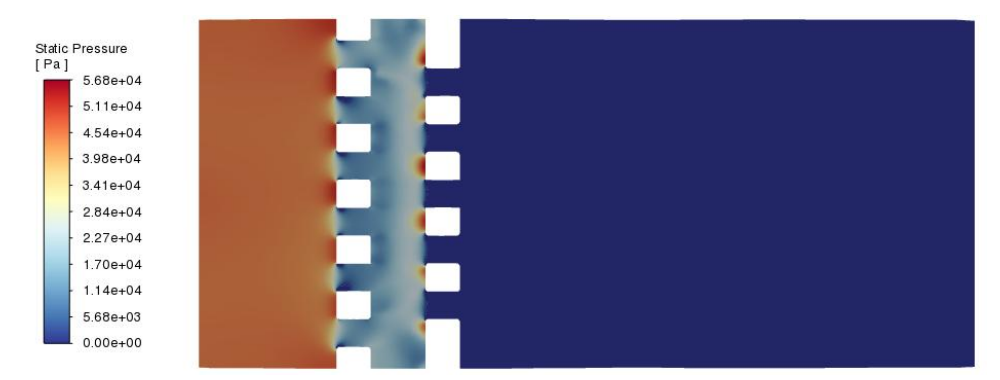


Figure 27: Contour plot of the static pressure on the YZ-plane at x=0 of the plates with holes first design.

In the contour plot of static pressure, it is possible to observe correctly that the pressure is higher at the inlet in order to drive the flow through the domain. When the fluid encounters obstacles and restrictions, it accelerates and due to Bernoulli's principle, there is a decrease in static pressure. Conversely, in regions where the velocity decreases, such as after the grids, the pressure tends to increase for the same reasoning. Moving towards the outlet, the pressure drops until it reaches the boundary condition imposed at the outlet, which is set to zero (gauge pressure).

The velocity is also a limiting characteristic, and it can be visualized in the same plane:

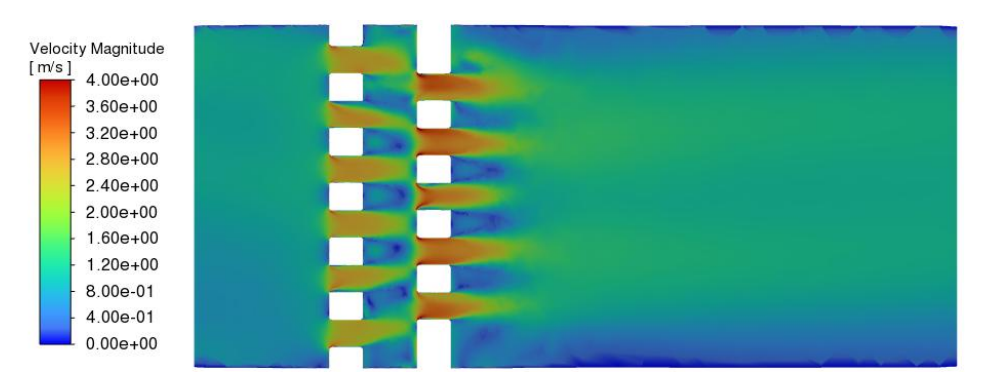


Figure 28: Contour plot of the velocity on the YZ-plane at x=0 of the plates with holes first design.

What it is interesting to look now is the maximum velocity, which is 4 m/s compared toing the imposed limits, and where it is localized: the range of higher velocities is localized inside the holes and near the restrictions as expected.

With these firsts results it is possible to continue the analysis on the geometry because it respects the limits, and the physics expected.

#### 4.2.2.2 Stress distribution

The result of the simulation which is interesting in the aim of this work is the distribution of the shear stresses.

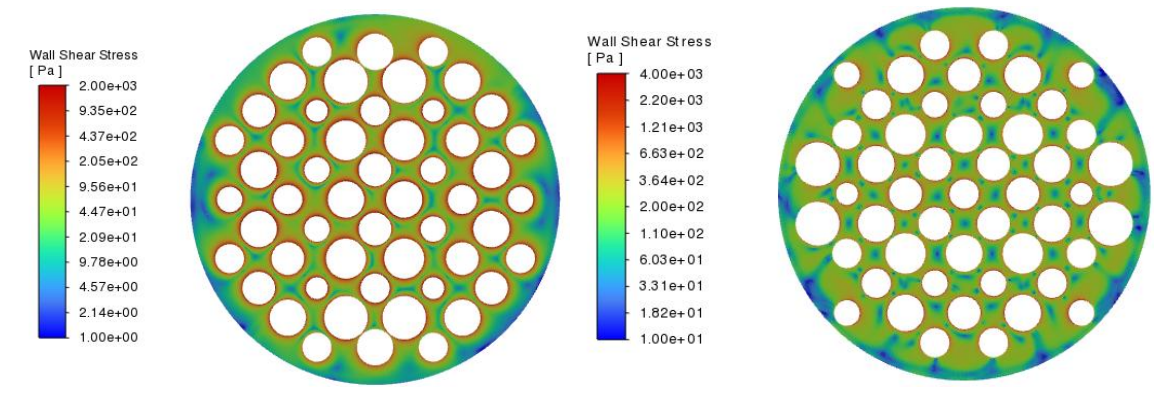


Figure 29: Contour of the shear stress in the inlet walls of plate A and B, respectively, of the Design I.

The lower limit is modified for both the contours plot to have a better visualization of the results, but the wall shear stress has a minimum about 0,5 and 5 Pa respectively for inlet A and inlet B. The main difference between the two contours is that in the second one is well visible the influence of the first one: between the holes of *Plate B* there are some minimum values of wall shear stress since the fluid there impacts perpendicular and so the shear stress is null.

At this stage, it becomes quite difficult to clearly interpret the global behaviour resulting from the different design parameters. Despite significant variations in hole radii and restriction types, the resulting differences in shear stress are relatively small; this suggests that the high level of flow disturbance tends to homogenize the effects, reducing the flow's sensitivity to these geometric changes. As a result, the considerable effort invested in designing and manufacturing such complex plate geometries does not seem to be justified by a proportional improvement in performance.

For these reasons, a second design was conceived and implemented, aiming to achieve a similar pressure drop while using fewer holes and introducing a lower level of flow disturbance.

## 4.3 Design II: low number of holes, larger diameters

## 4.3.1 Design results

To maintain almost the same pressure drop and range of velocities of the configuration before, it is necessary to evaluate its flow area. Considering four holes for the *plate A* and three for the *plate B*, it is possible to construct a structure as follows:

Table 15: Diameter evaluation for the Design II.

	Flow area Design I [mm²]	Diameter Design II [mm]
Plate A	2668,783	33,65
Plate B	2348,341	29,34

The diameter evaluated are rounded to the next integer and so for the *plate A* the diameter of the three holes is 34 mm and for *B* is 30 mm.

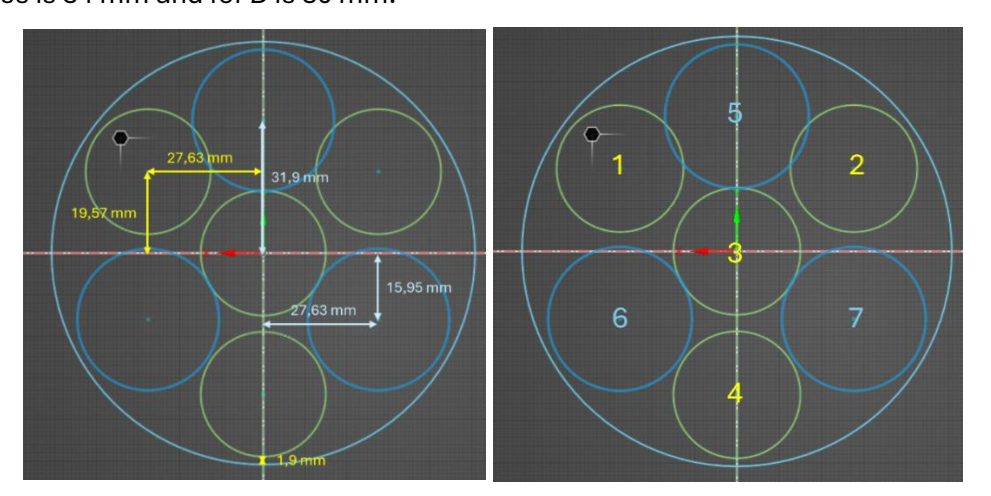


Figure 30: Design II of the plates with holes, in yellow the plate A and in blue the plate B.

#### Concerning the restrictions the following scheme is applied:

Table 16: Changes of the type and the radius of the restriction in the plates. The types are represented as R for the rounded one, C for the chamfer and E for the original Edge.

Hole's number	1	2	3	4	5	6	7
Restriction type	Е	С	R	R	R	С	E
Radius [mm]	-	0,5	0,5	0,25	0,5	0,5	-

## 4.3.2 Hydraulic results

#### 4.3.2.1 Hydraulic requirements

As said before it is important to not overcome the limits on velocity and pressure, so it is important to previously analyse them.

Concerning the velocity the maximum value is around 5,3 m/s which means that the limit is reached but is not exceeded. The pressure along the plane YZ is the following:

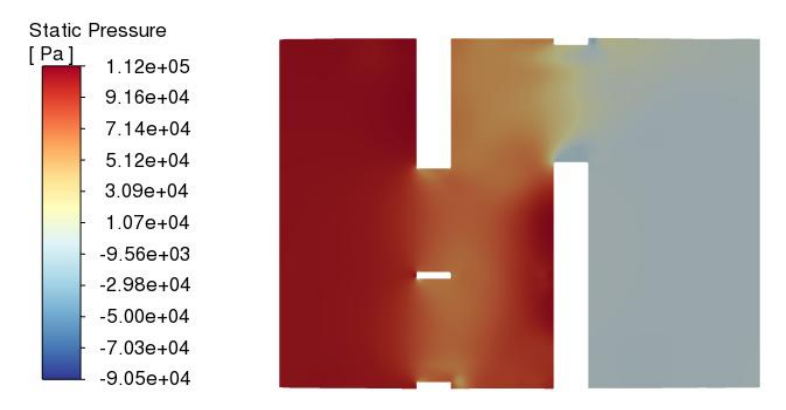


Figure 31: Contour plot of the static pressure on the YZ-plane at x=0 of the plates with holes second design.

The pressure is correctly higher where the velocity is lower to push it through the length and the area weighted average pressure drop is around 1,05 bar, so with only this geometry half of the pressure drop permitted in all the test section is achieved. This is acceptable provided that the other geometries in the test section generate significantly lower pressure drops, as is intended in this project.

This geometry is much more limiting than the one constructed with the Design II, concerning both the velocities and the pressure drop, but it will permit to study in a better way the global and local behaviour with less disturbance of the fluid.

#### 4.3.2.2 Hydraulic results

#### 4.3.2.2.1 Velocity distribution

From the following contour plot it can be understood that behind the wall of the *plate A* and *B* there is a recirculation zone where the velocity is near to 0 and so it is expected a low stress, and a high pressure drop there.

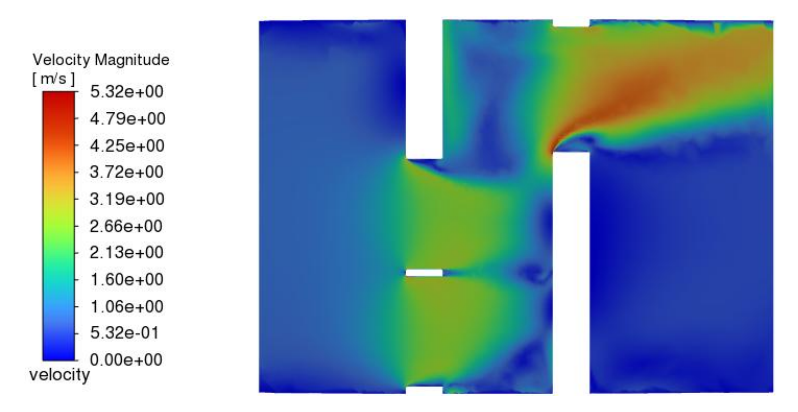


Figure 32: Contour plot of the velocity on the YZ-plane at x=0 of the plates with holes second design.

It can be understood from the Figure 32 that from the inlet of the holes are present detachment points of the fluid where in some cases has not time to reattach in the length of the holes. Because of that, in these cases, it is expected on the walls of the holes lower shear stress compared to the ones at the inlet restriction of the holes themselves, but a higher disturb created by the turbulence phenomena. In fact, it will be necessary also to study the turbulence parameters in these zones to understand more clearly what happens.

It can be interesting to understand also the velocity distribution before the plates with holes to then couple this information with the one of the shear stresses and corrosion-erosion. To do that, as the velocity on the wall is zero, it is necessary to understand where the hydraulic boundary layer is located; it can be done plotting the velocity profile along a line perpendicular to the wall and look where the velocity is stabilizing. The fluid profile in the plane parallel to the plate with holes will be not homogeneous because it is influenced by the following geometry and also by the inlet condition, so the choice of the point where to insert the line to look at the profile is not obvious. Different lines in different points are considered to have an average of the boundary layer thickness³ which is near to 5 mm for every case.

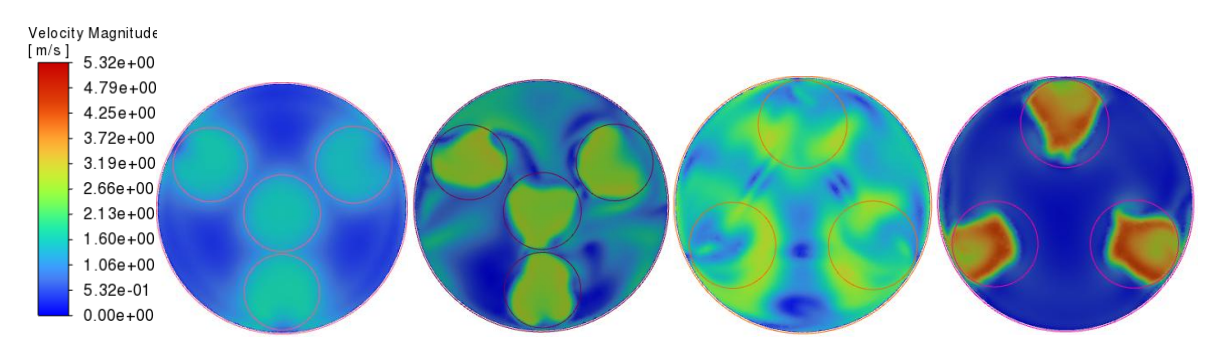


Figure 33: Velocity contour plot at plane parallel to the wall of the plates with holes, placed at a distance of 5 mm compared to the latter. From right to left, front A, back A, front B and back B.

It is possible to look in the front A that the velocity distribution is affected by the presence of the plate A itself, while in the back of the same plate obviously the velocity is higher at the holes exit as also happens in back B. While in front B the velocity is affected by the following plate B, but less effectively thanks to the jets exiting from plate A.

#### 4.3.2.2.2 Turbulence distribution

As said before, talking about the velocity distribution along YZ, it is interesting to study what happens inside the holes and outside them. To do that it is possible to look at the turbulence kinetic energy along YZ:

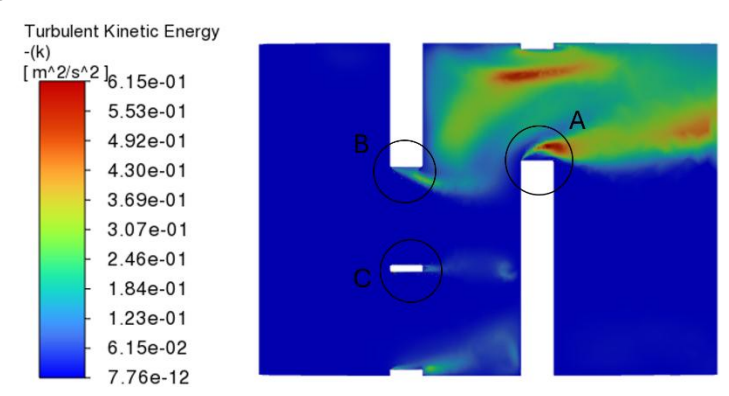


Figure 34: TKE plot along the plane YZ at x=0.

Considering the plot of the velocity in Figure 32, it is possible to see that the turbulence is intense where the velocity is lower especially where some detachment from the wall occurs. As shown in

<sup>&</sup>lt;sup>3</sup> It has to be noted that the one called now "boundary layer thickness" is not properly it, because here the velocity does not reach a constant plateau, but the maximum velocity is taken as the maximum one reached in the section.

Figure 35 to Figure 37, regions of low velocity near the solid boundaries correspond to high TKE zones, particularly in areas where boundary layer separation is present. These detachment zones generate strong shear layers and recirculation, which in turn increase turbulence production.

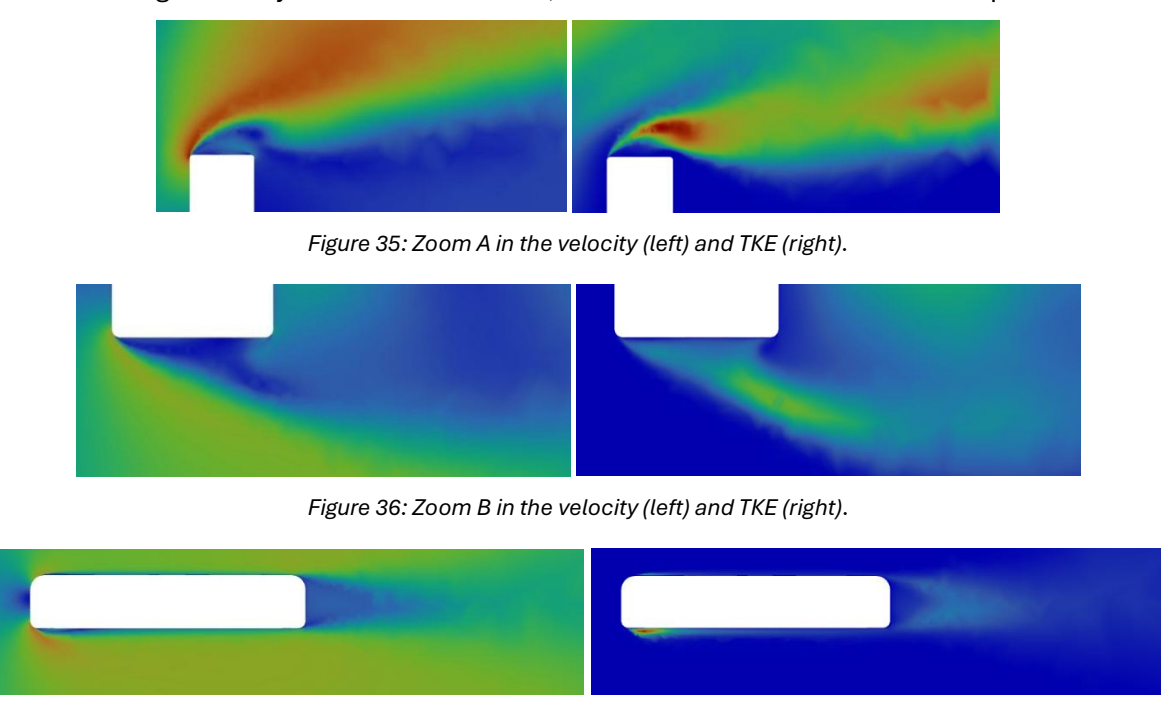


Figure 37: Zoom C in the velocity (left) and TKE (right).

From all the zooms, it can be seen that where the fluid detaches from the wall, the turbulent parameter starts to increase. It reaches its maximum values in the recirculation zones, where the velocity approaches zero; this drop in velocity is due to the turbulence effects, as vortices redistribute momentum and locally cancel out the velocity components.

The interface between high- and low-velocity regions acts as a turbulence generator, remembering that turbulence is not only associated with flow separation but also with strong velocity gradients. These effects are clearly visible in Zoom A, where the curvature of the flow around the obstacle promotes detachment, and in Zoom C, where a wake structure develops downstream the wall. Overall, these plots highlight the coupling between flow separation, recirculation and TKE, confirming that the turbulent kinetic energy is higher where momentum loss and flow instabilities are greatest.

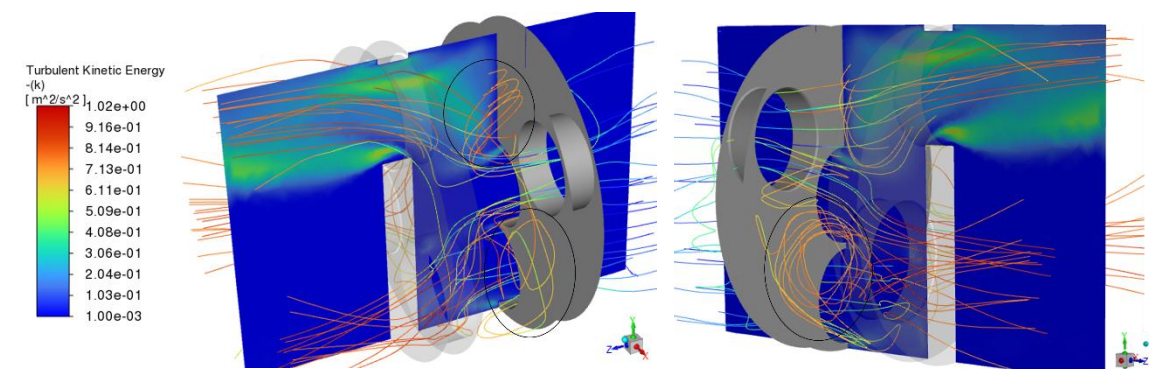


Figure 38: Streamlines and contour of the TKE.

Thanks to Figure 38 it is visible where the turbulence can affect the back wall of the *plate A* (black circles) and that inside the holes of *plate B* the turbulence is very high so a possible strong erosion in this zone can due also to that.

Regarding the back wall A and the front wall B, Figure 39 presents the contour plots of the TKE on two planes: one located 0,5 mm downstream of plate A, and the other 0,5 mm upstream of plate B. These planes allow the evaluation of turbulence distribution in close proximity to the solid surfaces.

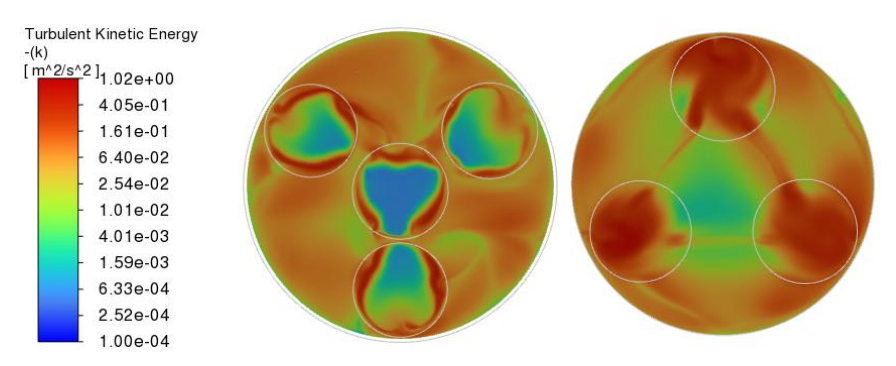


Figure 39: TKE contour plot on a plane after the plate A and on a plane before plate B (distance from them of 0,5 mm).

As expected from the evaluation of Figure 38, from the plot above it is evident that the walls are subject to significant turbulence. The information derived from these plots can be particularly valuable in identifying critical areas for erosion rate measurements. Note that the regions within the holes are not considered for this analysis, as the flow behaviour there is more complex and affected by additional geometric factors, studied in 4.3.2.2.4 Influence of the restrictions.

#### 4.3.2.2.3 Shear stress distribution

As said in the introduction of the erosion-corrosion parameters, the main component which take to increase this phenomenon is the shear stress.

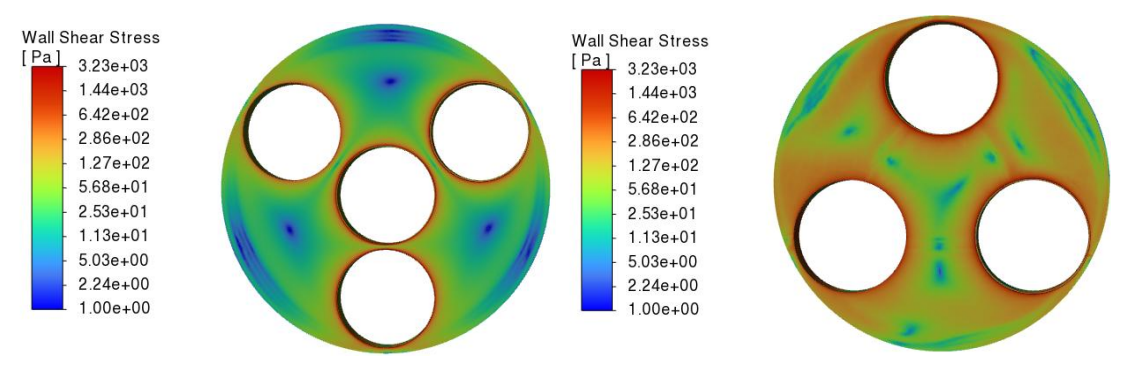


Figure 40: Contour of the shear stress in the inlet walls of plate A and B, respectively, of the Design II.

From the above figure it is possible to see that where the flow arrives perpendicular to the wall the shear stress is near to zero (here is 1 Pa only to re-scale the colormap due to the exponential behaviour). Instead, getting closer to the holes the fluid has some distortion, and it impacts on the wall not perfectly perpendicular and so creating some shear stress which is maximise to the restriction zone. This is totally expected, but now it is quantified. As said always in Section 1.3.1.3, where the wall shear stress is maximum, the normal one is minimised and it can be shown by the static pressure plot:

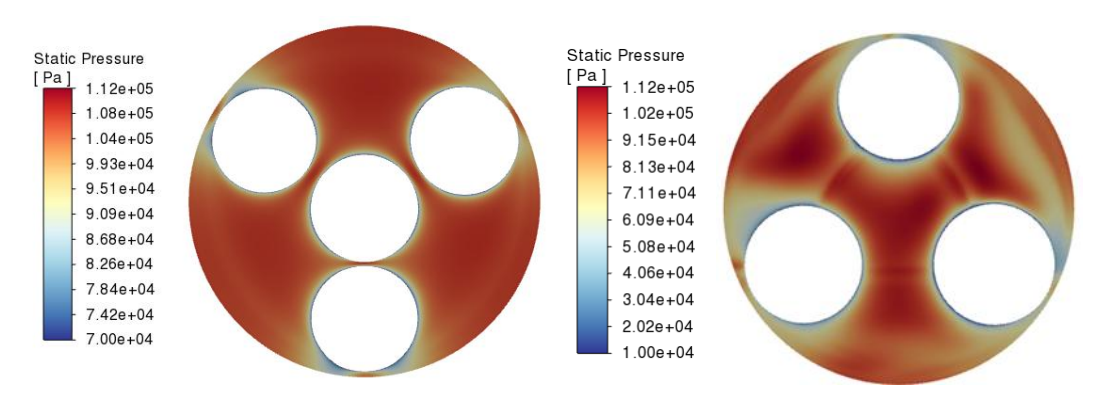


Figure 41: Contour of the pressure in the inlet wall of plate A and plate B respectively.

In Figure 41 where the jets impact the *plate B* the pressure is quite high, and it reflects perfectly in the opposite way the shear stress plot.

Considering the holes it is important to understand the values of the shear stress:

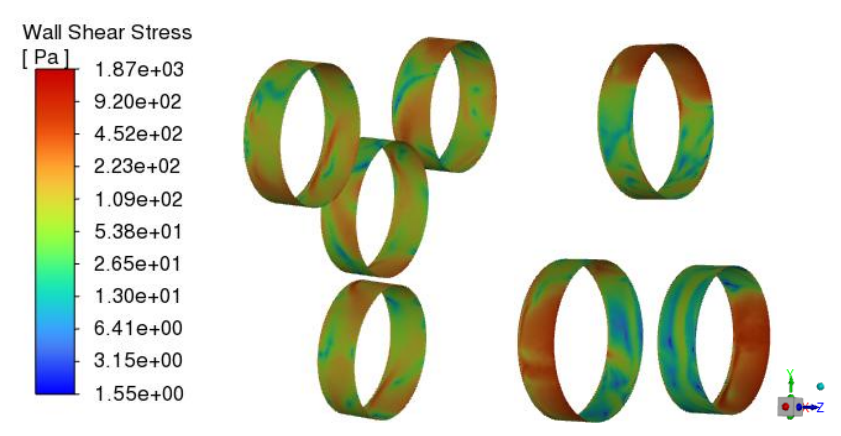


Figure 42: Contour of the shear stress in the wall of holes A and B respectively.

This contour plot reflects perfectly the velocity one in the sections of both the holes: where the velocity is changing a lot near the wall, which means the gradient of the velocity is higher, also the shear stress on the wall is higher.

#### 4.3.2.2.4 Influence of the restrictions

Because the shear stress is very important considering the erosion-corrosion phenomena and it is maximised on the restrictions, it is important to deeply understand what happens locally on them. Some zooms on them can be reported here and in the next sub-section the limits will be reported:

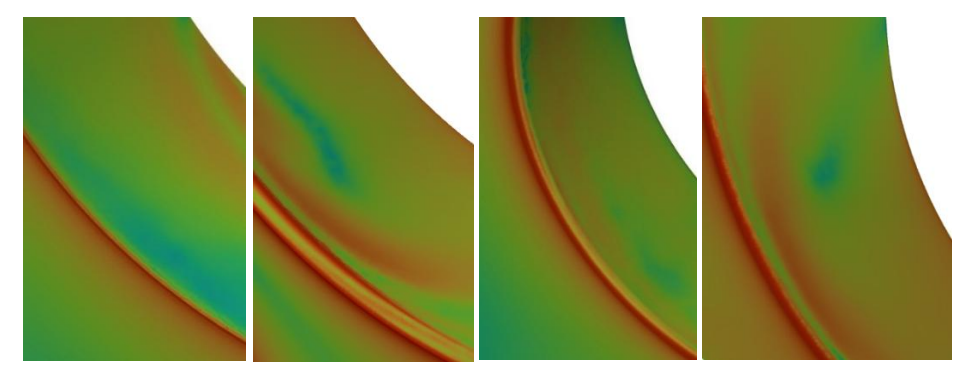


Figure 43: Zoom of the shear stress contour on restriction 1, 2, 3 and 4 in plate A.

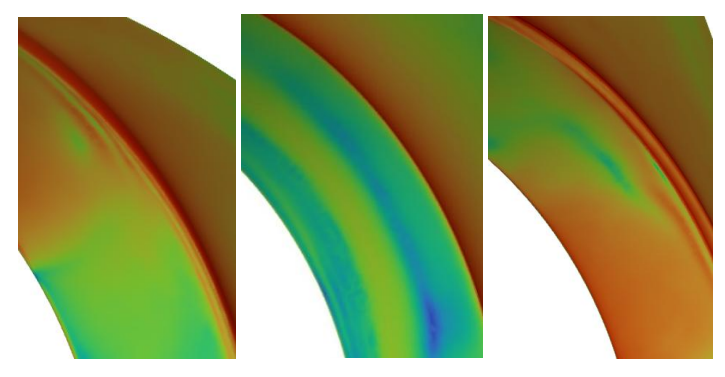


Figure 44: Zoom of the shear stress contour on restriction 5, 6 and 7 in plate B.

In this design it is only possible to look the effects of the types of finishing of the restrictions and not the ones created by the holes' radius because in each plate they are the same.

Considering the maximum velocities, they are registered in the boundary layer of the restriction's inlets, and it is possible to register the stress on the wall locally. For the *plate A* the following data are collected:



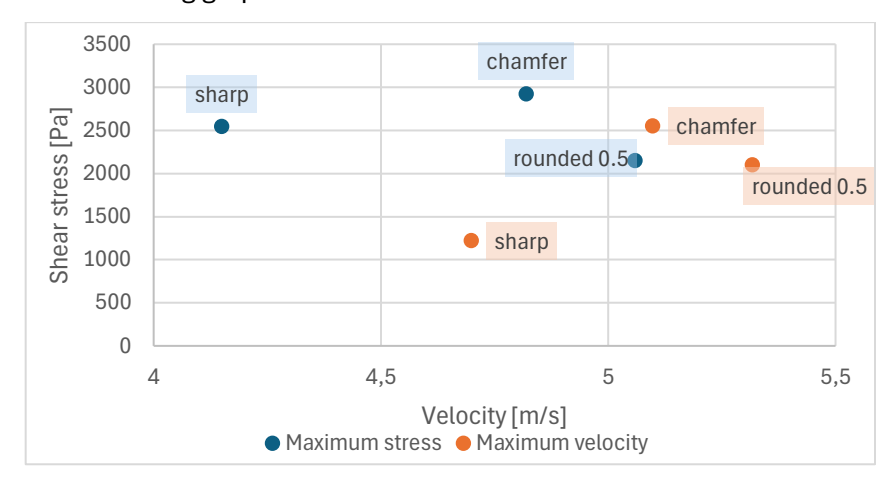
Graph 4: Maximum velocity and stress versus local shear stress in the plate A.

The results are the following concerning the maximum values:

- Rounded 0,25 mm edge shows the highest velocity (~4,2 m/s) and highest shear stress (~2300 Pa). This indicates that the smaller rounded radius facilitates a more focused, faster flow, likely with higher local acceleration and wall interaction.

- Chamfer 0,5 mm results in moderate velocity (~3,6 m/s) and relatively high shear stress, suggesting a decent flow acceleration with significant surface interaction.
- Rounded 0,5 mm has the lowest shear stress (~1400 Pa) and a lower velocity (~3,5 m/s), supporting the idea that a smoother and longer transition reduces flow acceleration and wall shear.
  - At almost the same velocity the chamfer edge has obviously a higher stress than the rounded higher radius edge.
- Sharp edge shows a lower velocity (~3,1 m/s) but still high shear stress (~1800 Pa), likely due to flow separation or turbulence at the discontinuity.

For the *plate B* the following graph is obtained:



Graph 5: Maximum velocity and stress versus local shear stress in the plate B.

Again the sharp edge reaches its maximum stress at low velocity and it reaches a lower maximum velocity compared to the other edges due to its discontinuity. Now the rounded achieves higher velocity and no more the same at lower maximum stress compared to the chamfer one, which means that here its capability to drive the flow more gently is amplified.

Where the restriction is an edge, the maximum velocity is registered inside the holes and not on the edge, but here it is taken into consideration the maximum velocity near the edge. The following image represents where the maximum velocities are localized near the wall:

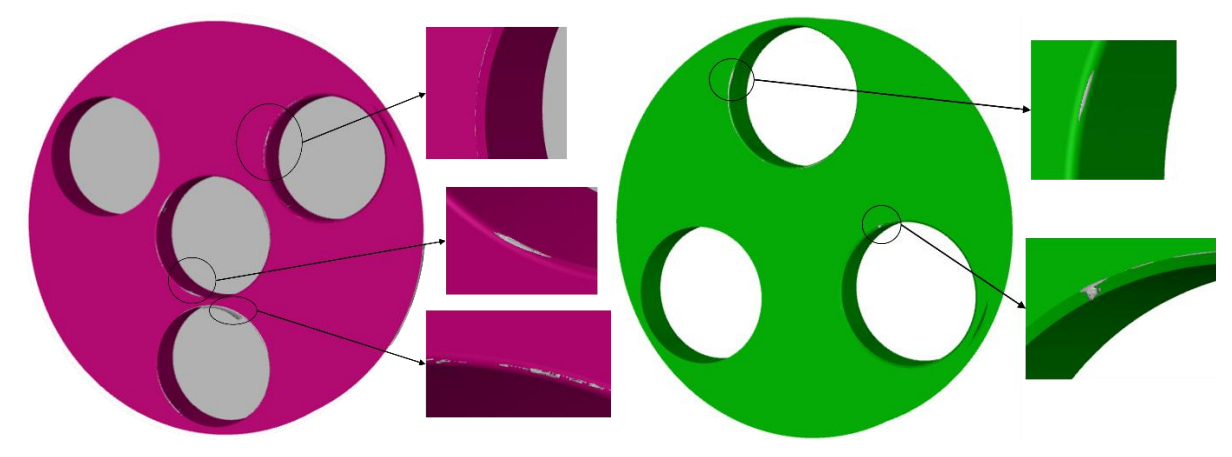


Figure 45: Maximum velocities localized near the wall at the restrictions.

Can be seen easily that in the chamfer edge the maximum range of velocities are localized at the inlet corner of the edges as also with the rounded one, as expected.

Concerning the maximum stress locations, they do not correspond at the same coordinate of the maximum velocities, but they appear in the same way along the edges' borders:

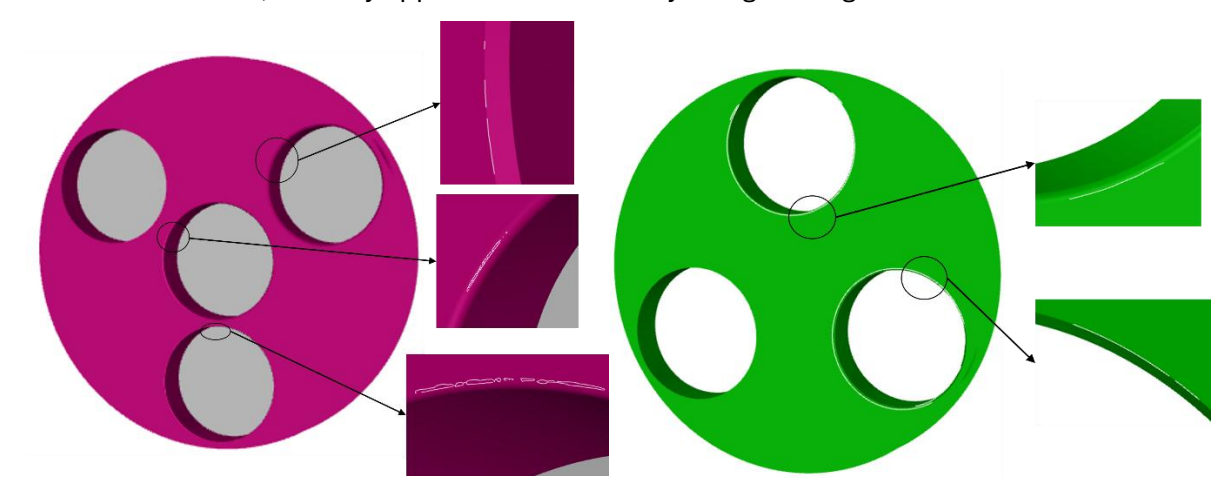


Figure 46: Maximum stresses localized near the wall at the restrictions.

### 4.4 Numerical results

## 4.4.1 Convergence

Also, in this case the kinetic turbulent parameter does not reach the convergence criteria of 0,001, in fact it decreases only until 0,01. As for the previous case, all the other parameters converge at almost 50 iterations so much before the hundreds done. Because of that the comment about the convergence is the same as the array of cylinders. Figure 16: Residuals of the steady state simulation of the array of cylinders.

## 4.4.2 Grid independence analysis

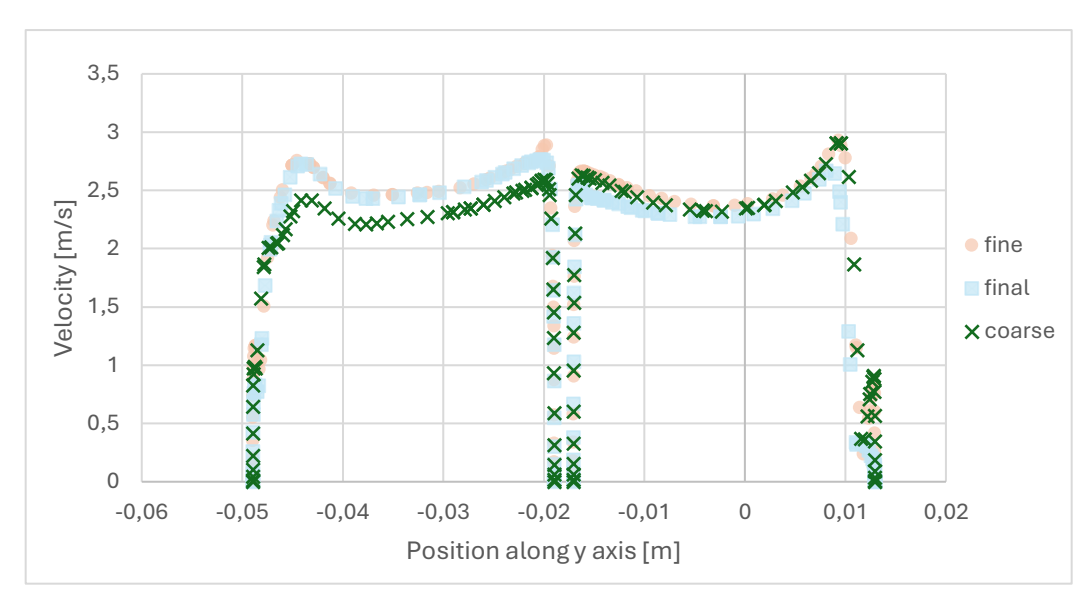
As done in Section 3.3 a grid independent analysis is pursued. Here the multiplication factor is taken again equal to 1,25 and the parameters become as follows:

Table 17: Mesh independence parameters of generation.

	Surface mesh	Face-size	Volume mesh
Case-study	0,2 - 6 mm	0,1-0,2 mm	6 mm
Fine	0,16 – 4,8 mm	0,08-0,16 mm	4,8 mm
Coarse	0,25-7,5 mm	0,125-0,25 mm	7,5 mm

The inflation layers are also there not modified to not influence too much the y+ values reached.

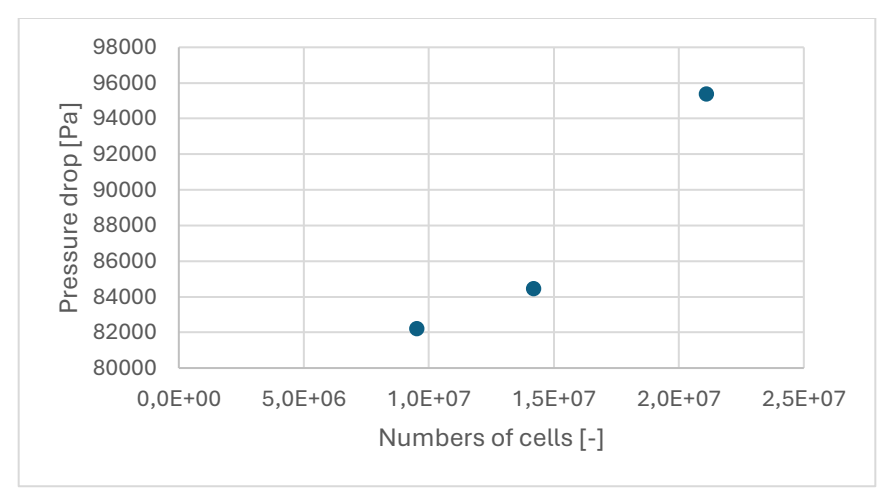
In this case on a xy-diagram the velocity profile of the flow is taken along y-axis in the middle of the holes A, at x=0:



Graph 6: Velocity profile along the holes A y-axis with three different meshes: the case study (final), the fine and the coarse ones.

The results tend to be the same near the wall, this because the parameters which influence y+ do not change, while in the fluid inside the holes away from the walls the meshes are a little bit different. This is much more visible in the hole 4 where the coarse mesh registers lower velocities compared to the other two more accurate meshes. This can be because there the velocity has a strong gradient and the coarse mesh is not able to do a good measure.

As done for the array of cylinders the pressure drop is the studied quantity to evaluate the grid independence:



Graph 7: Pressure drop along the plate with holes geometry as a function of the number of cells through the mesh refinement.

A mesh independent solution is obtained if the pressure drop, increasing the number of cells, approaches an asymptotic value reducing the delta at each step. This is not happening here, so the solution is mesh dependent and because of that the results have to be analysed being conscious that they can be affected by the choice of mesh parameters.

# Chapter 5 – Inclined squared plates

The configuration with inclined plates allows to study the flow behaviour at specific impacting angles. This study is necessary because the flow can impact on the walls of the infrastructure with different angles at high velocities and it is important to assess if jets with certain impact angles should be avoided.

## 5.1 Simulation setup

The concept of using inclined squared plates emerged when the impact angle became a key parameter to control, and this configuration proved to be easy to manufacture. It is essential to accelerate the flow and guide it in a direction parallel to the pipe axis; therefore, the impact angle corresponds to the inclination of the plate. This setup can be achieved by placing the plates immediately downstream of the perforated plate and aligning them with the holes, allowing the flow to accelerate through the holes and directly strike the disks.

## 5.1.1 Geometry

As introduced in Section 1.3.1.2, the most critical impingement angle is 45°. In this configuration three inclined squared plates can be considered and so three different inclination angles.

The 90° angle represents the case where the flow, after passing through the *plate A*, impacts almost perpendicularly onto a second perforated plate. Since 45° is the critical angle, it is deliberately selected for analysis.

Then it is reasonable to study what happens in between 0° and 45° where the shear stress will be higher, so a 30° angle inclination is chosen; then to enlarge the studied margin, without create too much pressure drop, it is possible to choose an inclination of 60°.

## 5.1.2 Mesh generation

The shear stress has to be studied on the faces of the inclined plates and so inflation layers have to be used on their surfaces. The mesh parameters are the following:

Table 18: Mesh settings for the inclined plates.

Type	Local refinement	Location	Values [mm]
Surface mesh	/	All the surfaces	0,02-4 (growth 1.2)
	Curvature	Disks' surfaces	0,1-1
		Disk surfaces, E	1,8*10 <sup>-3</sup>
Inflation layers	First Height Size	Disk surfaces, F	1,6*10 <sup>-3</sup>
		Disk surfaces, G	1,7*10 <sup>-3</sup>
ı			

Volume mesh / All the volume 4 (polyhedral, growth 1,25)

In this case, for the surface mesh, the Minimum Size is taken as  $S_n$  and the Maximum one as the smallest size of the geometry, because  $S_n$  is very low due to the little inflation layers.

The number of inflation layers are everywhere 20 with a transition ratio of 0,272. The mesh generated with these settings is shown below:



Figure 47: Mesh generation on the plane yz with x=0 on the left, on the right a zoom on plate E.

The criteria for y<sup>+</sup> are satisfied and it can be seen with a contour of it on the walls:

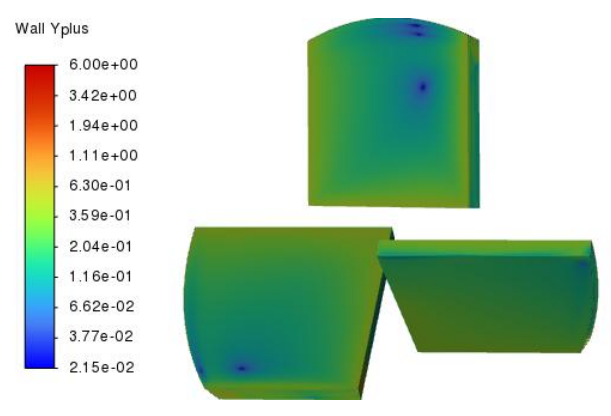


Figure 48: y+ contour on the plates.

As result y+ is greater than 1 only on the conjunction between the main pipe and the plates as happen also for the previous geometries.

## 5.2 Design and Hydraulic results

## 5.2.1 Design

The inclined plates are designed to be larger than the holes in *plate B* in order to increase the impact area. As previously mentioned, it is important for the flow to directly impact the inclined plates immediately after exiting *plate B*, in order to take advantage of the acceleration gained. Therefore, the centres of the inclined plates are positioned 40 mm downstream from the hole outlets and are aligned with them.

Each inclined plate has sides of 50 mm and a thickness of 4 mm.

Then the plates have the following inclination:

Table 19: Inclined plates' geometrical configuration.

Disk Angle [°] Rotated around Sign of rotation Angle surface-z axis [°]

Е	30	y-axis	Negative	60
F	60	x-axis	Negative	30
G	45	x-axis	Positive	45

Considering all these parameters, the design for the inclined plates is represented by Figure 49.

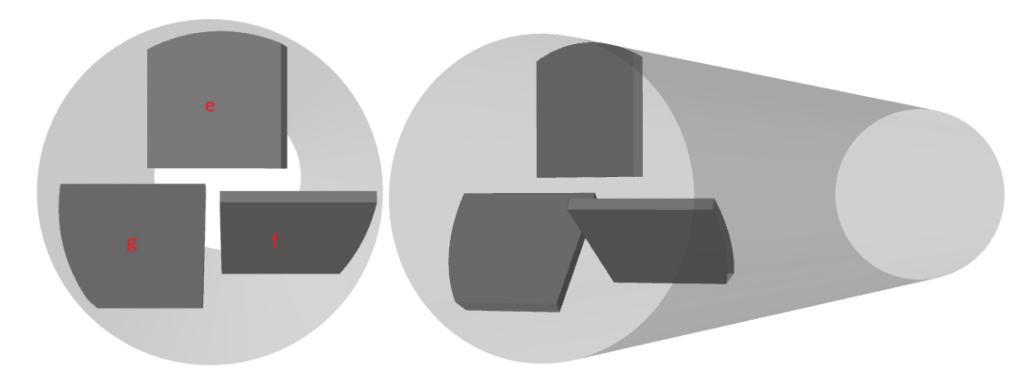


Figure 49: Design of the inclined plates.

## 5.2.2 Hydraulic

### 5.2.2.1 Hydraulic requirements

It is important firstly to understand which velocity and pressure values are obtained to be sure that the geometry satisfies the global hydraulic requirements of the test section.

The maximum velocity achieved in this geometry is 2,83 m/s and the pressure weighted on the inlet surface gives a resulting pressure drop of about 0,13 bar, perfectly in line with the design requirements.

The design has also to satisfy the requirement about the impact on the plates surfaces which has to be straight and parallel to the flow main direction, so along z. Also, with the inlet condition now considered, and so the developed hydraulic profile, this is respected as can be seen in the following path-lines plots:

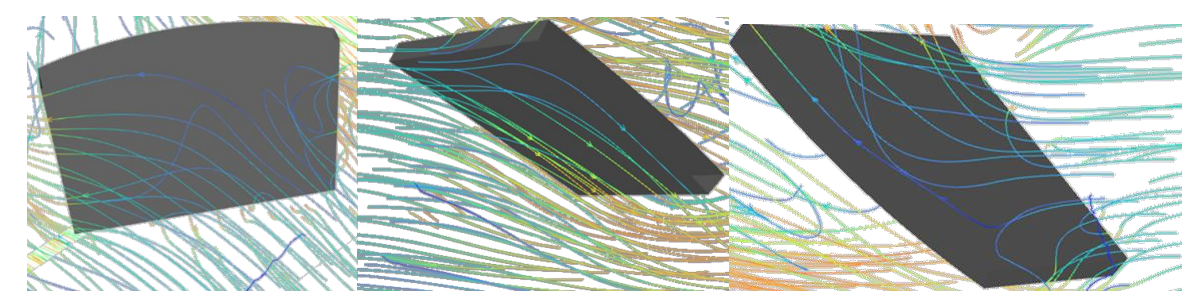


Figure 50: Path-lines coloured by velocity magnitude on the plate E, F and G (front-side).

### 5.2.2.2 Hydraulic results

#### 5.2.2.2.1 Velocity distribution

The velocity distribution in the z=0 plane can be seen in the following contour plot:

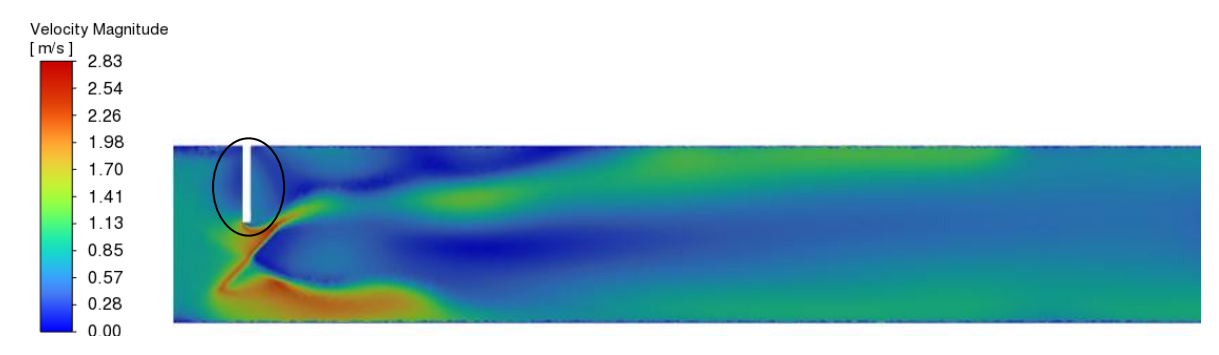


Figure 51: Contour plot of the velocity along the plane YZ at x=0, where the circle indicates the plate E.

It can be easily understood that the velocity increases where the plates are located and it is also visible that the fluid detaches at the edges of the plates creating some recirculation behind it.

The velocity distribution in front of the disks is evaluated at the boundary layer thickness and are visualized here:

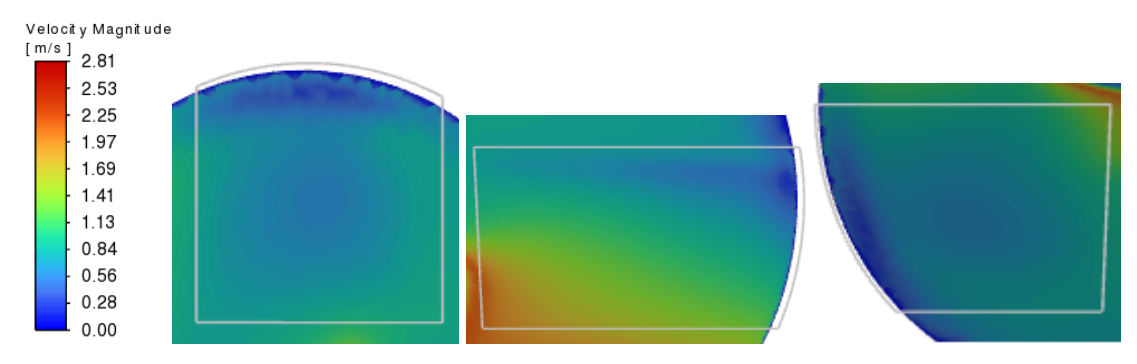


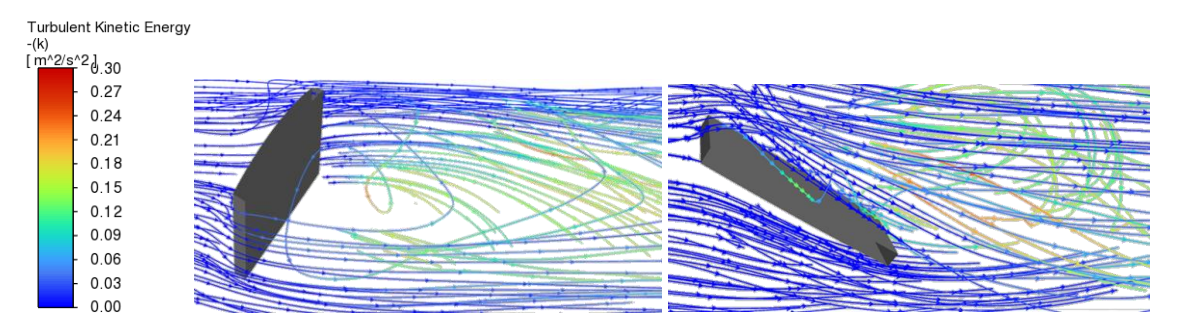
Figure 52: Velocity magnitude on front-planes parallel to the disks and placed at the boundary layer distance before the disks themselves. In the figure, from the left, are shown plate E, plate F and plate G.

Looking at Figure 50, where the fluid directly impacts the disks, so on the right-top side of E, on the top side of F and on the downside of G, the velocity shown in Figure 52 is near to zero.

#### 5.2.2.2 Turbulence distribution

As said in the introduction, the shear stress is not the only parameter which is wanted to be analysed to predict where erosion may occur on surfaces. It is necessary to analyse also the turbulence parameters to have a better understanding of it and to not forget the areas where maybe the shear stress seems low but maybe the erosion will be very impacting.

To do that it is necessary to look if some turbulence phenomenon is taking place in the volume, like a recirculation zone. To recognise where recirculation is taking place it is possible to visualize the path-lines and colour them with the value of turbulent kinetic energy:



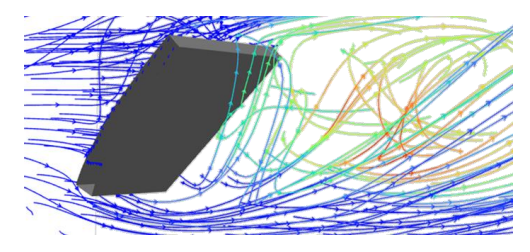


Figure 53: Path-lines coloured by TKE in the back-face of every disk. From left to right E, F and G.

Looking at these figures above it can be understood that the vortex is created mostly after disk E and G, where also the kinetic energy is higher, and here it can affect the erosion-corrosion phenomena. We can have a better look at the turbulent effect with a contour plot of the same quantity on planes parallel to the disks positioned at a distance of 5 mm:

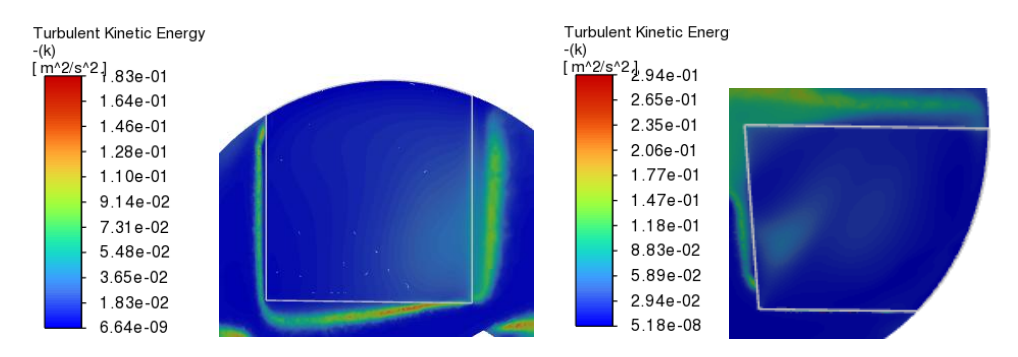


Figure 54: Back view of the TKE plot on the surfaces parallel to the plates placed 5 mm after these ones.

It can be seen that the higher TKE is near the boundaries of the plates where the flow is detaching from the front-surface, and it starts to give rise to turbulence. It can be shown also on the YZ plane:

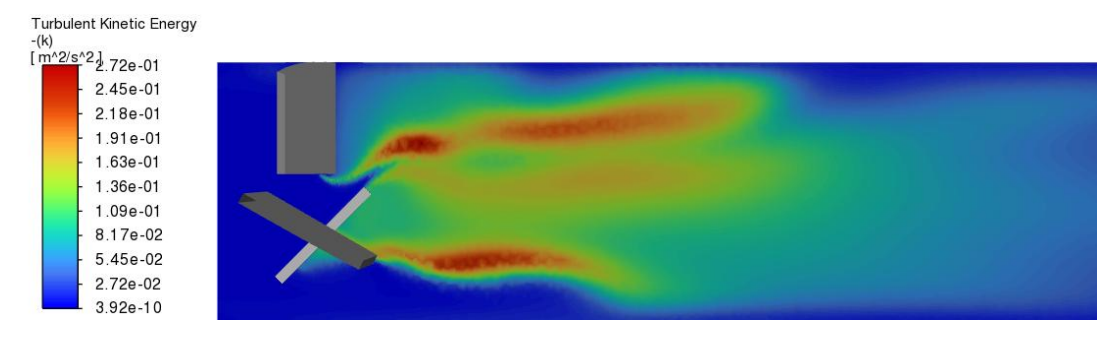


Figure 55: TKE on the YZ plane.

#### 5.2.2.3 Impingement angle influence

It is interesting to see the pressure distribution on the front surfaces of the plates:

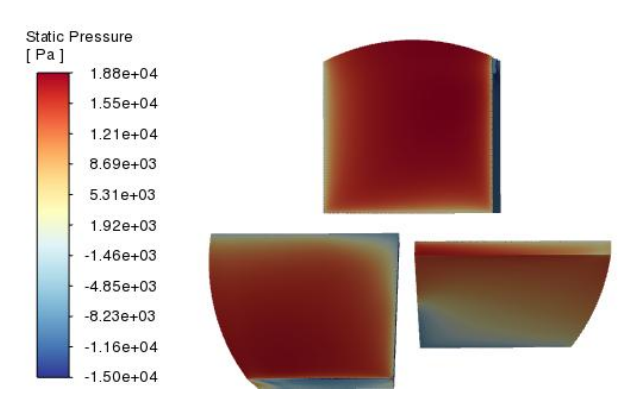


Figure 56: Static pressure contour plots of front surfaces of the inclined plates.

This plot shows the static pressure due to the jet impingement on the surfaces of the plates. Here an explanation of what is happening on these surfaces:

- The incoming flow has a certain initial energy composed by pressure and velocity;
- Where the incoming flow first strikes the plates namely, the bottom surface of plate G, the upper surface of plate F, and the right-hand side of plate E, as can be seen in Figure 50 part of the initial energy is converted into static pressure;
- Here a stagnation zone is formed, where the velocity is null and the pressure increases;
- After the impact the flow is deviated and it accelerates along the surface, so the pressure decreases and the kinetic energy of the fluid increases;
- During this deviation part of this energy is dissipated thanks to viscosity, creating higher shear stresses on these parts of the plates, and turbulence.

Following this reasoning on the pressure distribution, it is expected a higher shear stress distribution in the parts of the plates which are not directly impacted. In fact, for this geometry it is interesting to understand how the shear stresses vary with the inclination of the plates, to then be able to couple the information shear stress-erosion at a certain impacting angle which is known be more effective compared to the perpendicular force.

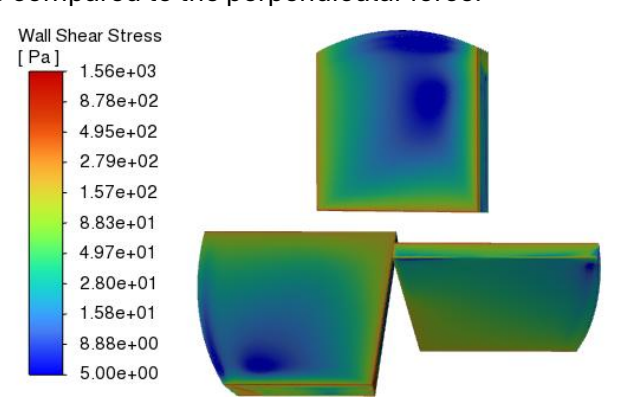
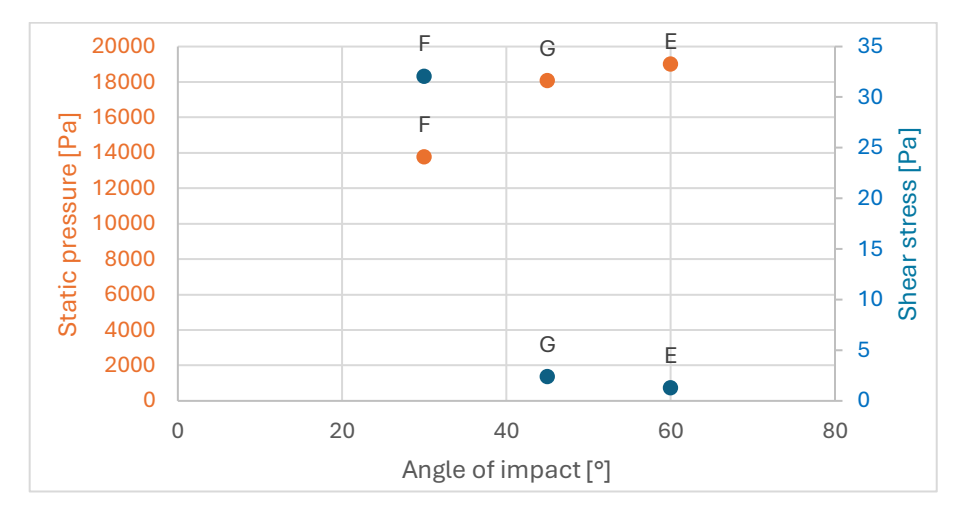


Figure 57: Wall shear stress contours on the front plates' surfaces.

As expected, the shear stress is very low where the fluid directly impacts, to then increase along the surface where it is deflected to reach then the maximum at the edges of the plates which the analysis is not interested in. While the static pressure, which represents the normal stress, has the opposite behaviour.

As said in the introduction, where the impact angle between surface and fluid main direction is lower the shear stress is high and the normal one is low. It is expected to have these results where

the fluid directly impacts as discussed before, so on the right-top side of E, on the top side of F and on the downside of G.



Graph 8: Stress versus angle of impact on the surfaces of the inclined disks.

The Graph 8 represents exactly the expected behaviour. In this case, the top side of the disks F is the place where the shear stress characterizes better the behaviour of erosion-corrosion considering that it is known the perfect angle of impact and it is the highest one so the rate of corrosion can be easily seen.

### 5.3 Numerical results

## 5.3.1 Convergence

In the study of the inclined plates the continuity reaches a value of almost 0,2, one hundred times larger than the one accepted as a criterion: this value stabilise around the 50<sup>th</sup> iteration until the 300<sup>th</sup> one. A report flux on the net mass flow rate evaluated at the inlet and outlet gives a difference of 4,47\*10<sup>-3</sup> kg/s, but considering the mass flow rate in the inlet of the domain of the inclined disks which is 62,529 kg/s the relative error on the mass balance can be evaluated as follows:

$$\epsilon_{rel} = \frac{\dot{m_{net}}}{\dot{m_{in}}} * 100 = \frac{0,0047}{62,529} * 100 = 0,0075\%$$

A value of relative error in the mass flow rate of 0,0075% is low and it means that the residual of the mass conservation is high due to numerical issues as too strong relaxation factor and poor local mesh quality. From a physical and engineering perspective the solution arrives to a convergence.

The mesh quality is poor only where the inclined disks touch the external tube surface and considering the absence of layers on this wall the numerical issue can depend by that. Figure 16: Residuals of the steady state simulation of the array of cylinders.

## 5.3.2 Grid independence analysis

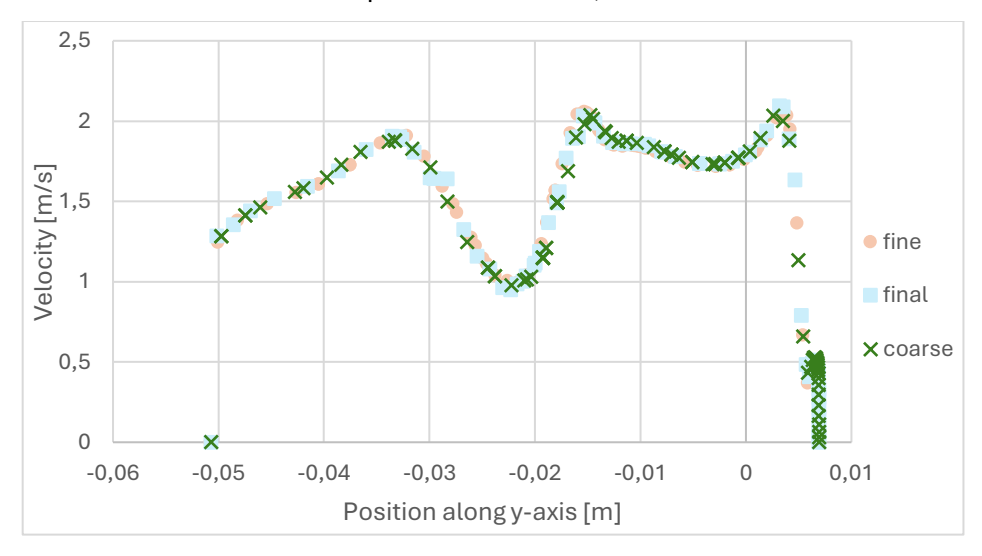
The multiplication factor for the grid independence analysis is taken again equal to 1,25 and the mesh parameters are now the following:

Table 20: Mesh independence parameters of the inclined disks case study.

	Surface mesh	Face-size	Volume mesh
Case-study	0,02 - 4 mm	0,5 mm	4 mm
Fine	0,016 – 3,2 mm	0,4 mm	3,2 mm
Coarse	0,025 - 5 mm	0,625 mm	5 mm

The inflation layers are also there not modified to not influence too much the y+ values reached.

In this case on a XY-diagram the velocity profile of the flow is taken along y-axis interpolating the z-coordinate where the centres of the plates are located, at x=0:



Graph 9: Velocity profile along the y-axis for the inclined plates with three different meshes: the case study (final), the fine and the coarse ones.

The velocity profiles stop to the coordinate 0,0069 where the *plate E* is located and where obviously the imposed velocity is zero on all the wall until the tube wall. The high distance between the values at the coordinate y=-0,0508 and the next value on the nearest coordinate indicates how the mesh is constructed, without inflation layers on the tube wall: correctly the coordinate of the fine mesh is the nearest to the -0,0508 one and the coarse one is the most far one.

The three profiles are perfectly coherent between them, thanks to the fact that they are closely overlapped which is a signal of mesh independence.

# Chapter 6 – Full test section simulation

At this stage of the work, when all the geometries are being characterized with the same boundary conditions it is necessary to understand how they interact with each other. Because of that it is necessary to simulate the geometries of the obstacles together in the same simulation or importing the effects of the previous geometries as inlet conditions.

It is important to note that, since all simulations are based on RANS models, instantaneous turbulent fluctuations are not resolved in both the full geometry and the segmented domains. However, in the full domain simulation the mean turbulent quantities, and so here k and  $\omega$ , evolve consistently along the entire geometry, naturally accounting for the interactions between obstacles. In contrast, in the segmented approach the turbulent boundary condition is statically imposed at the inlet of each sub-domain and as a result, it may not fully reproduce the mean turbulent field that would develop dynamically in the full configuration because the inlet is not conditioned by the downstream. In this chapter the analysis is concentrated before on a deep understanding of the full geometry results and then comparisons between the full and the segmented geometries are done.

### 6.1 Full test section characterisation

The full geometry studied in this chapter has the same mesh of the previous obstacles' geometries, to maintain an acceptable  $y^+$ , with 19092778 cells and the characterising parameters of the mesh are the following:

Table 21: Quality mesh parameters of the full test section.

Quality mesh parameter	Recommended values	Actual values
Skewness	< 0,7	0,58
Minimum orthogonal quality	0,1	0,02
Orthogonal quality	> 0,1	0,89

Concerning the geometry the distances between the obstacles are represented as follows:

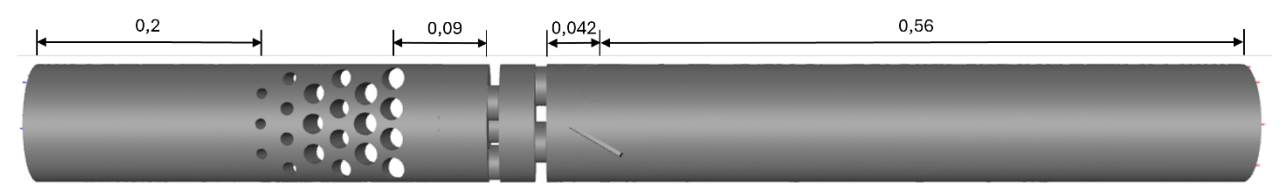


Figure 58: Full geometry test section along z axis, with relative distances between the obstacles and a full length of 1,042 m.

Compared to the analyses done in the previous chapters the things which are changed are only the outlet locations to not have backflow in the fragmented geometries while all the other measures are the same.

The total pressure drop has to compared to the maximum value of 2 bar and at the outlet of the test section it is measured a pressure drop of about 1,53 bar, so the limit is satisfied.

### 6.1.1 Array of cylinders

The hydraulic requirements are satisfied for this geometry and the analysis done on Chapter 3 remains valid. In fact, considering this geometry the results of the full geometry simulation must be confronted with the one studied in Chapter 3 because the inlet remains the same, while what change is the outlet condition. In the fragmented geometry the outlet condition imposed after a length of 0,7 m was 0 Pa, while in the full one obviously it is represented by the following geometries present in the length of the test section.

The range of values of the properties is imposed on the full geometry section of the cylinders array as the fragmented one.

#### 6.1.1.1 Velocity distributions

The velocity distributions of the fragmented and full geometry are reported below:

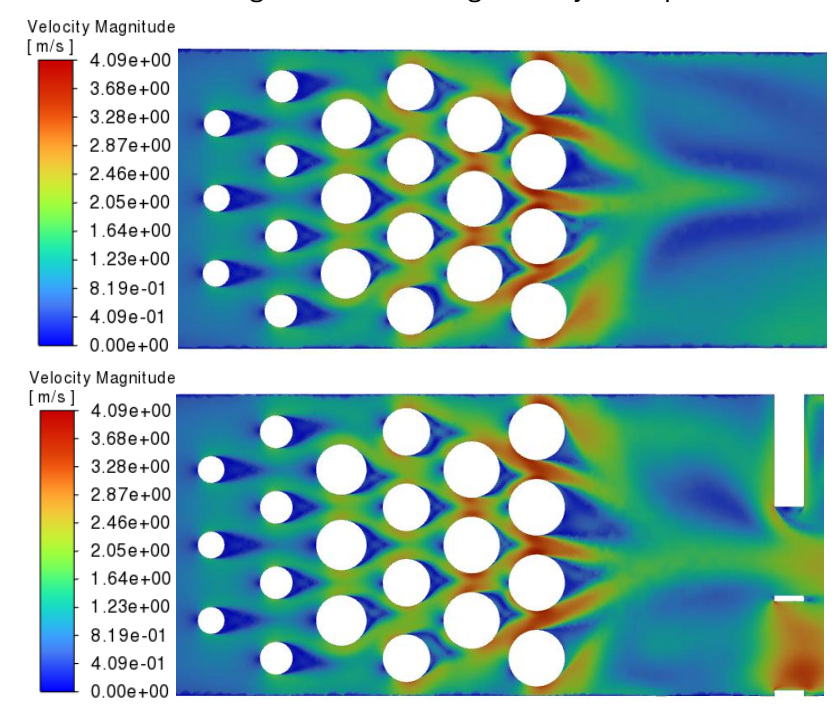


Figure 59: Velocity distribution along YZ plane at x=0 of the cylinders array. Above the profile of the fragmented velocity, below the profile of the full geometry.

As can be seen the velocity distribution along the first five columns is almost the same, what is changing is obviously the profile after the last row. Here if there are no other obstacles which can affect the field, velocity can shed. While in the full geometry domain, the plate with holes imposes restrictions to the fluid flow: this influences the shedding and the main behaviour of the fluid before it. In Figure 59 in the full geometry the wake after the two central cylinders of the last row are larger and longer, while the two cylinders near the main wall have a wake where the velocity gradient is larger.

This can be explained by the fact that the presence of the perforated plate downstream of the cylinders introducing additional flow restrictions gives as a result an acceleration of the velocity gradients. These larger gradients increase shear and promote local instabilities, which in turn amplify turbulence production, particularly near the wall and in the wake of the central cylinders. In contrast, in the fragmented geometry, the absence of downstream obstacles allows the flow to expand and decay more freely, as said before.

#### 6.1.1.2 Turbulence distributions

Because the plate with holes influences the velocity profile behind the last row it is important to study the turbulence distribution there, because as said in Chapter 3, is also the place where the fluid reattaches on the wall of the cylinders. For the full domain it is expected a distribution on the plane YZ at x=0 almost equal considering the first columns of cylinders while for the last one, especially on the backside, it is expected, thanks to the observations on the velocity done before, for the full geometry a larger turbulence intensity compared to the fragmented one.

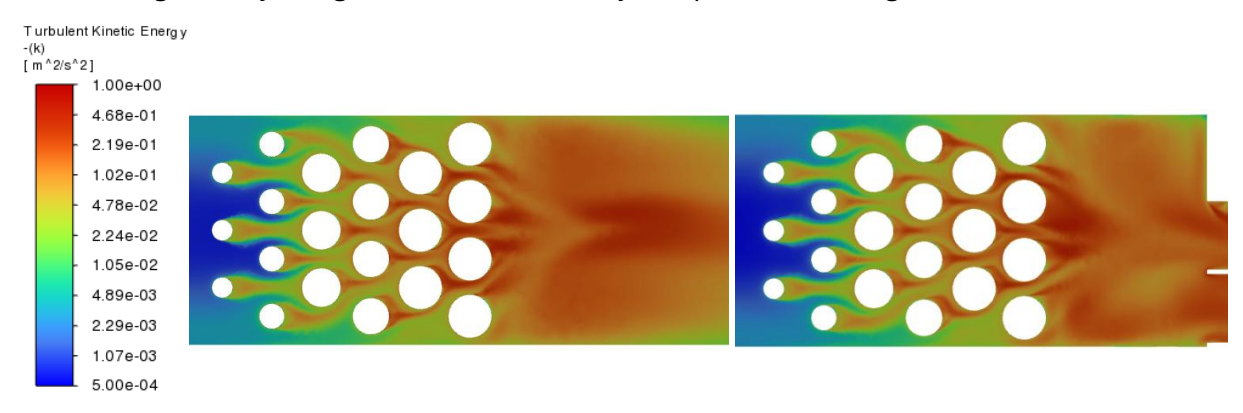


Figure 60: TKE distribution along YZ plane at x=0 of the cylinders array. On the left the fragmented profile, on the right the full geometry one.

It is confirmed from the Figure 60 that the turbulence is larger in the full geometry and this must be taken into account considering the role of turbulence on erosion-corrosion.

#### 6.1.1.3 Shear stress distribution

Because the velocity profile is similar between the columns of cylinders, the shear stress also will be similar because it depends on the gradient of the velocity itself: only the last column is affected by the next obstacle.

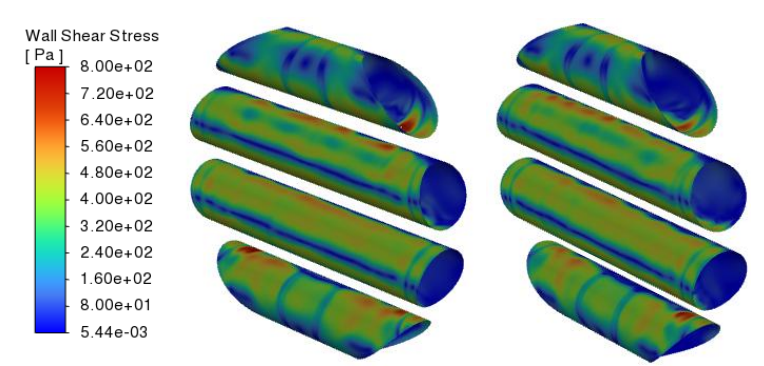
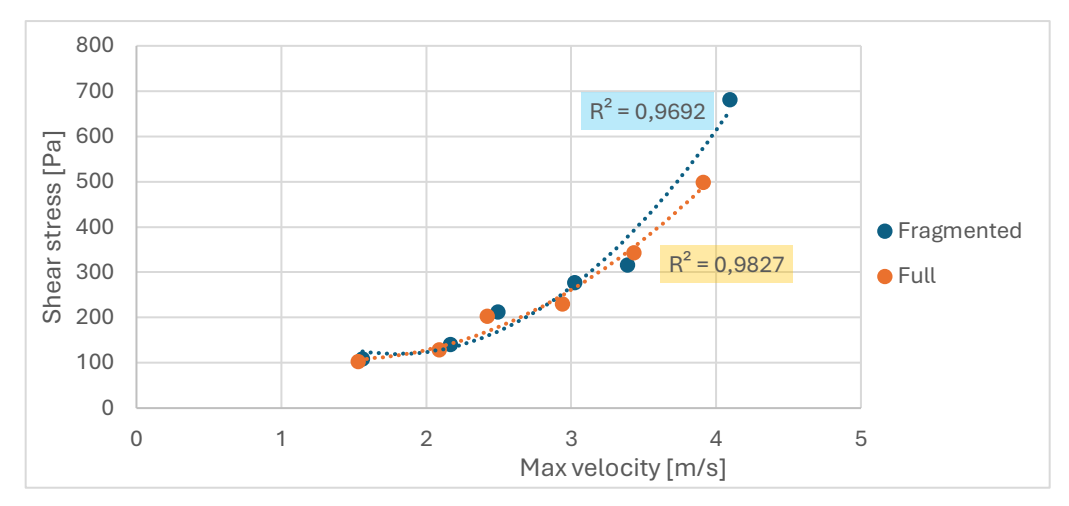


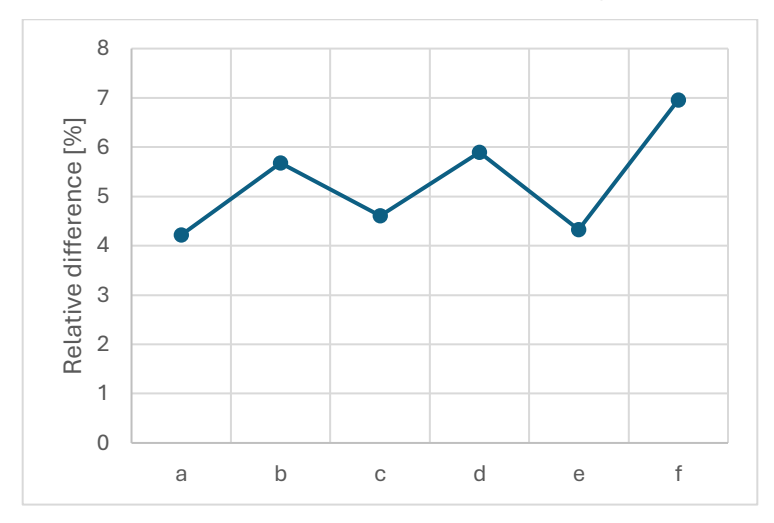
Figure 61: Shear stress distribution the cylinders of the column f; on the left the fragmented profile, on the right the full geometry one.

The above figure shows that the maximum shear stresses are registered almost in the same region, while obviously the values are a little bit different.



Graph 10: Wall shear stress function of the maximum velocity evaluated for each column of cylinders.

As can be shown in the graph above, the maximum velocities registered near the wall of the pipes and the corresponding local shear stress have a second order polynomial behaviour also for the full geometry. It is possible to quantify how much the full and the fragmented geometries differ on quantities such as shear stress, but this has to be done not locally but in an averaged way:



Graph 11: relative difference between area-averaged shear stress in fragmented and full geometries.

This graph represents the relative difference between the fragmented and full domains, and as can be understood the difference is not high and it is in between 4 and 7%. The discrepancy tends to increase slightly downstream, reaching a maximum at obstacle f, which may indicate cumulative effects due to the lack of fully developed upstream flow interactions.

#### 6.1.2 Plates with holes

For the last two obstacles it is important firstly to characterize the properties of the full geometry to be able to couple the information with the experimental ones, and then a comparative analysis can be done to understand if can be possible to save computational power and time simulating one type of obstacles per time.

### 6.1.2.1 Hydraulic requirements

For the design of these obstacles the two important parameters were the maximum reached velocity and the correspondence of the hole-wall in the two plates to make the fluid directly impact on the second wall exiting from the first one.

Firstly, the maximum reached velocity is around 5 m/s while concerning the direct impact of the fluid on the second wall the following vectors' plot gives the velocity vectors on the plane parallel to the inlet of the *plate with holes B* at 5 mm:

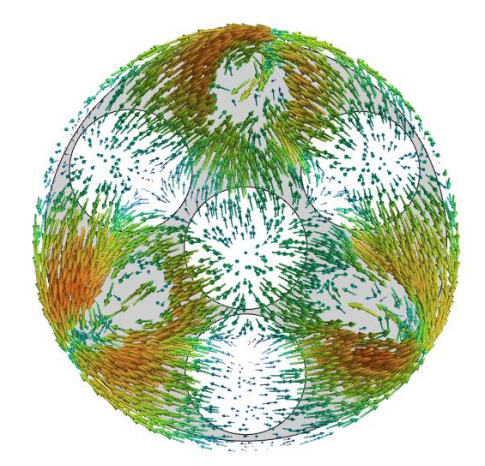


Figure 62: Velocity vectors on a plane XY at a distance of 5 mm before the inlet of plate B.

It is visible that the fluid impact perpendicularly the wall exiting from the previous plate with holes, so the design is confirmed.

### 6.1.2.2 Hydraulics results

## 6.1.2.2.1 Velocity distribution

As confirmed before the maximum velocity is near 5 m/s and it is acceptable. The distribution of the velocity along the length can give also an idea on where to look for turbulence intensity and stress development, as done in the sections before. Again, in the holes is present a detachment of the fluid and so a probable recirculation zone near the wall of them and these seems more accentuated compared to the profile studied in Section 4, also if the velocity range is similar.

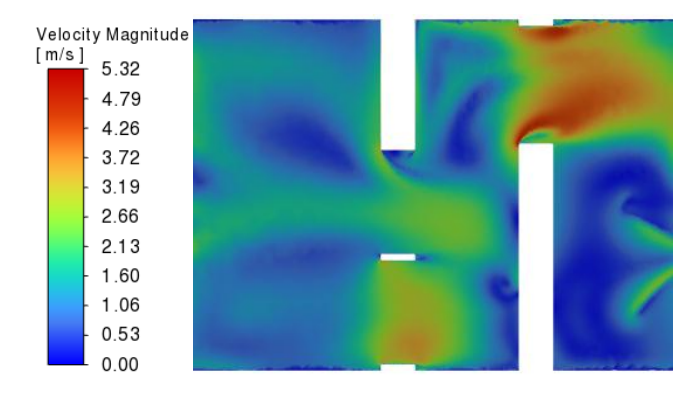


Figure 63: Velocity contour on YZ plane at x=0 on the plate with holes domain (full geometry).

As done in Section 4 it is useful to plot the velocity contour before and after the plates with holes to couple the information erosion corrosion-velocity.

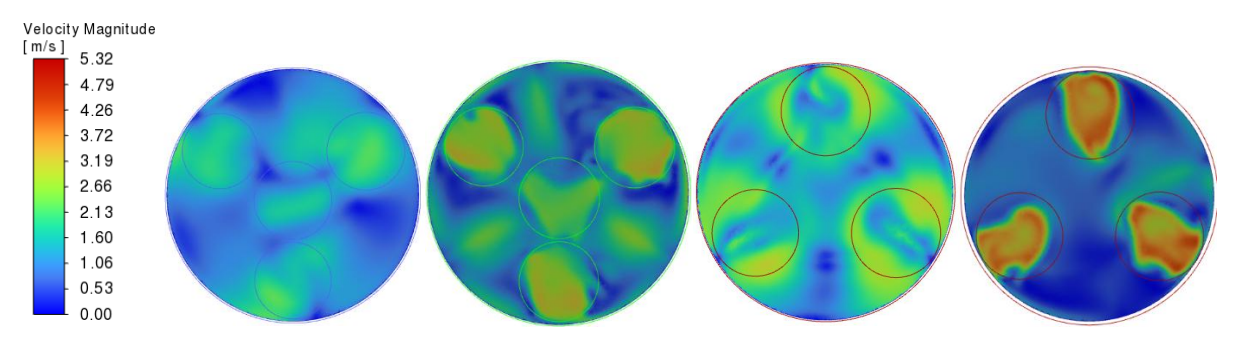


Figure 64: Velocity contour plot at plane parallel to the wall of the plates with holes (full geometry), placed at a distance of 5 mm compared to the latter. From right to left, front A, back A, front B and back B.

In the back of *plate A*, it is interesting to see how the *plate B* influence the distribution: at the location of the holes of B the velocity near the outlet of A is higher, which can mean that there can be some recirculation or instability phenomenon.

#### 6.1.2.2.2 Turbulence distribution

Firstly, it is interesting to look at what happen again at plane YZ in x=0 to couple the information velocity-turbulence intensity:

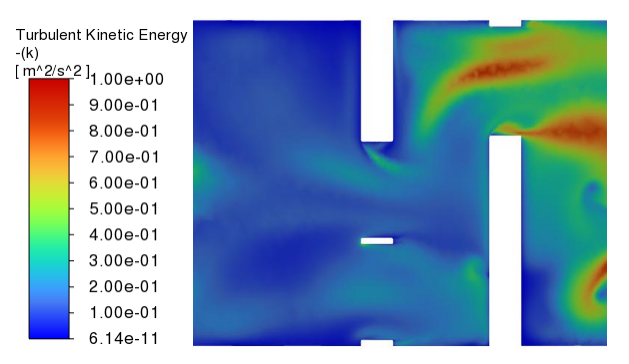


Figure 65: TKE contour on YZ plane at x=0 on the plate with holes domain (full geometry).

Again, regions of low velocity near the solid boundaries are corresponding to high TKE zones and in these regions, it is important to focus the attention.

The location where to look for turbulence are evidenced looking at the velocity - *outlet A*, *inlet B* and *outlet B* - and at the TKE contour - holes' walls.

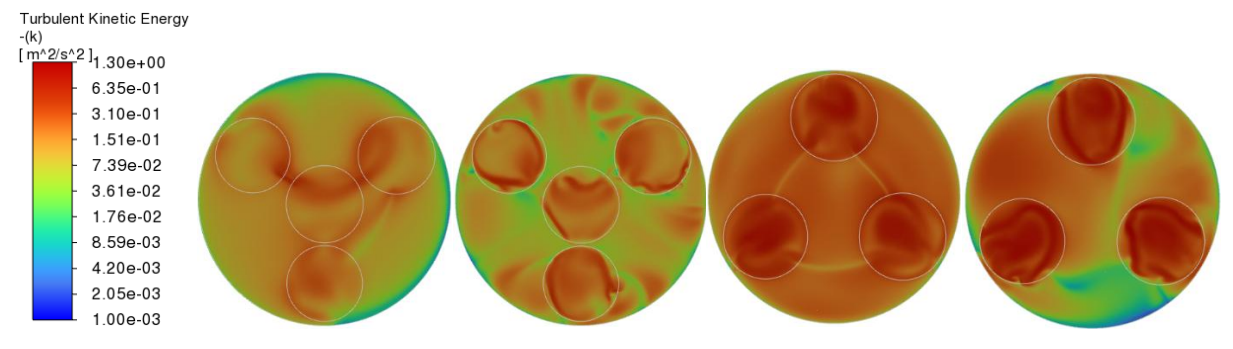


Figure 66: TKE contour plot at plane parallel to the wall of the plates with holes (full geometry), placed at a distance of 0,5 mm compared to the latter. From right to left, front A, back A, front B and back B.

In back A it is visible that where the velocity is higher in Figure 64, the TKE is lower which is a signal of recirculation and shear stress. In fact, a higher velocity means a more perpendicular velocity vector compared to the wall, and so lower TKE and shear stress, while after the impact on the wall the velocity vector aligns with the wall and here the circulation and the shear stress are higher.

As expected in the *front of B* the TKE is very high, again because the fluid impact on the wall and then come back towards the *back A*, but in *front B* is higher because is the first impact of the fluid.

#### 6.1.2.2.3 Shear stress distribution

Thanks to the previous discussion it is easy to understand where the shear stress can be higher, but it is important to quantify them.

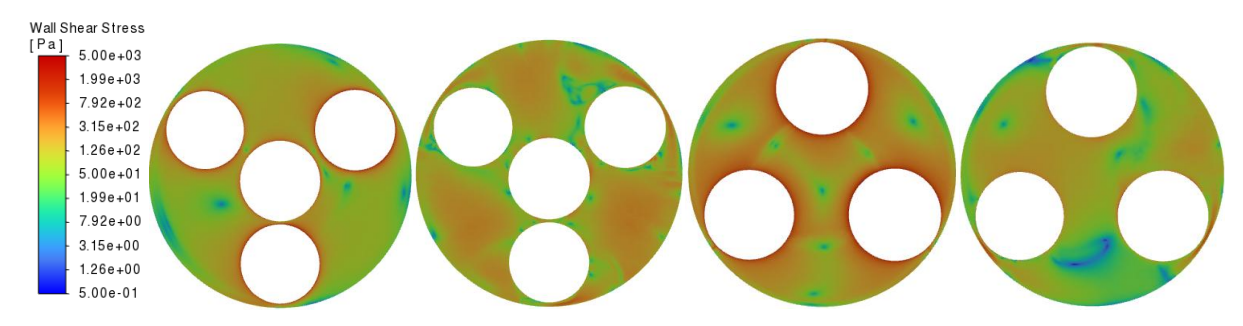


Figure 67: Wall shear stress contour plot at plane parallel to the wall of the plates with holes (full geometry). From right to left, front A, back A, front B and back B.

In the inlet faces the restrictions have obviously a higher shear stress distribution, while in general on the wall the maximum shear stress is registered on *front B*. In the *front B*, the shear stress has a distribution opposite to the TKE one, which underline the needs to have both the quantities measured because are both important for the phenomenon studied.

Another zone which is subjected to strong velocity gradients, according to Figure 63, is the holes' one:

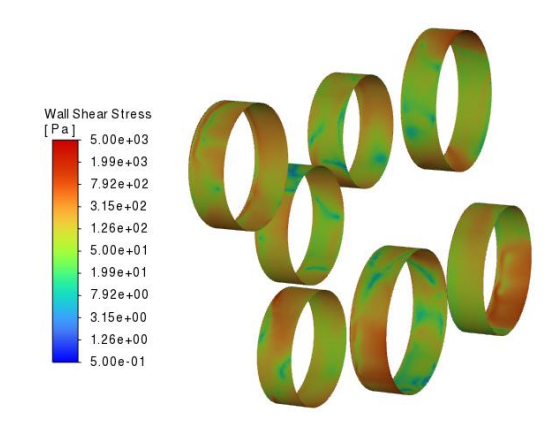
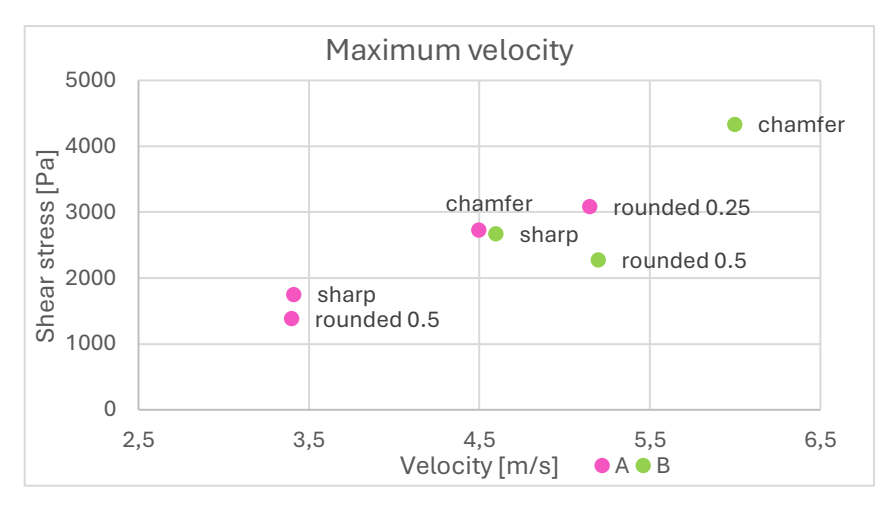


Figure 68: Wall shear stress contour of the holes' walls (full geometry).

### 6.1.2.2.4 Influence of the restrictions

How qualitatively the stress is distributed on the restrictions is well characterised in Section 4.3.2.2.4, while in this section it is important to give and localize for this case, where the boundary conditions are changed, the actual maximum shear stresses and velocities.



Graph 12: Maximum velocity versus local shear stress (full geometry).

As shown in Section 4, in *plate A* the rounded restriction with the smallest radius (0,25 mm) yields the highest local velocity and shear stress values, while the chamfer one produces elevated values, though slightly lower than the rounded 0,25 mm. The rounded edge with a larger radius (0,5 mm), however, shows a distinct behaviour: in Section 4 (uniform inlet velocity), it reached the highest velocity and lowest shear stress among the configurations, while here, due to the upstream disturbance introduced by the cylinder array, its performance is altered. The local velocity at that restriction is no longer the highest, also because the non-uniform inlet profile leads to a redistribution of the velocity peak away from the tube centre where this hole is located.

For plate B, a similar trend is observed: in Section 4, the rounded 0,5 mm edge achieved the maximum velocity, while the chamfered edge caused a higher shear stress for a lower velocity. In this configuration, the behaviour is consistent with that previously observed for plate A: the sharp and chamfered restrictions result in increased local stress due to stronger gradients, while the rounded one mitigates them more effectively.

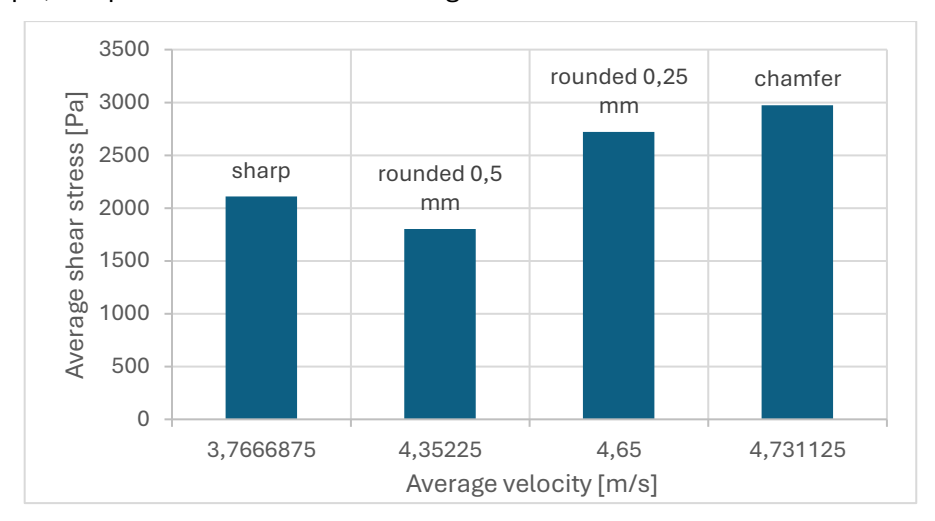


Graph 13: Maximum stress versus local velocity (full geometry).

A similar analysis applies when the maximum shear stress locations are used as reference points. For both plates A and B, the trends observed in the velocity-stress relationship remain consistent with the one discussed above: configurations that promote higher local velocities also tend to exhibit elevated shear stresses, particularly in the case of chamfer restrictions. Rounded

geometries, especially with a larger radius, help reduce stress concentrations even when velocity is high, confirming their role in flow smoothing.

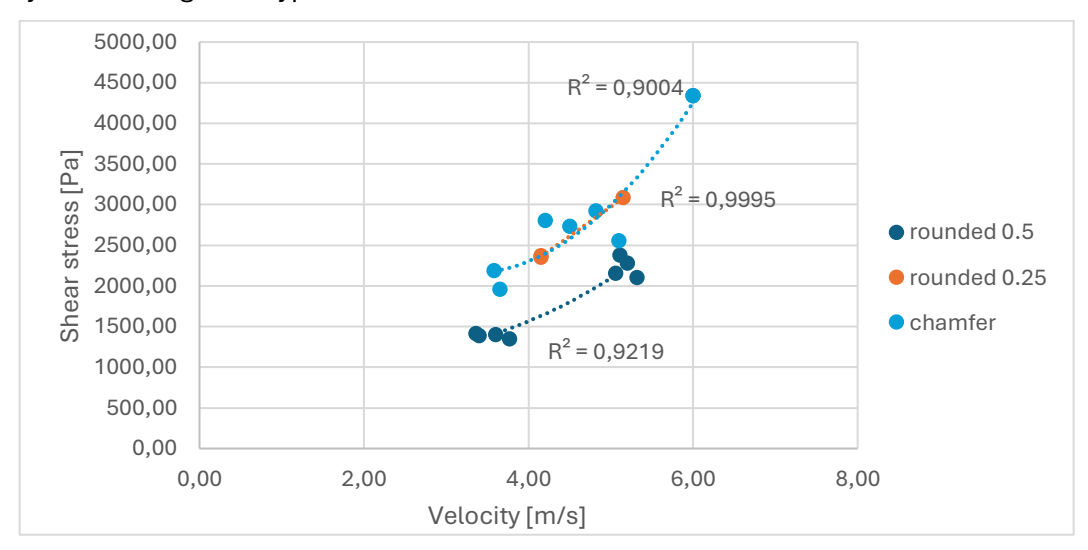
Now the data collected for the types of restriction are a useful number to characterize qualitatively the behaviour of the restriction types. Without looking specifically to the values of the next graph, it is possible to look their average behaviour:



Graph 14: Averaged maximum coupled shear stress and velocities compared to the type of restriction.

In this graph all the maximum coupling between shear stress and velocity points are averaged by the number of points. As said the chamfer restriction achieves the highest values of both the variables, while the rounded one with the lower radius achieves high shear stress at high velocities. The sharp restriction confirms to not help to develop a high velocity but for this low velocity the shear stress associated are high.

Always qualitatively it is possible to understand the behaviour of the shear stress compared to the velocity considering each type of restriction:



Graph 15: Maximum shear stress-local velocity points and maximum velocity-local shear stress points for the three types of restriction from the simulation with uniform velocity profile (Section 4) and for the total domain.

Graph 15 shows the second-degree polynomial fits for the velocity–shear stress relationship for each restriction type. The fits yield  $R^2$  values above 0,9 in all cases, confirming a quadratic correlation between local velocity magnitude and wall shear stress. The lower  $R^2$  for the rounded 0,5 mm edge, compared to the 0,25mm, suggests that in this configuration the stress response is more complex, possibly due to smoother gradients and less pronounced shear peaks. This correlation can be useful to estimate shear stress levels from velocity measurements in similar flow conditions.

It is also important as said before to evaluate where the maximum values of shear stress and velocity are to then focus the attention on them when the erosion-corrosion effect will be observed:

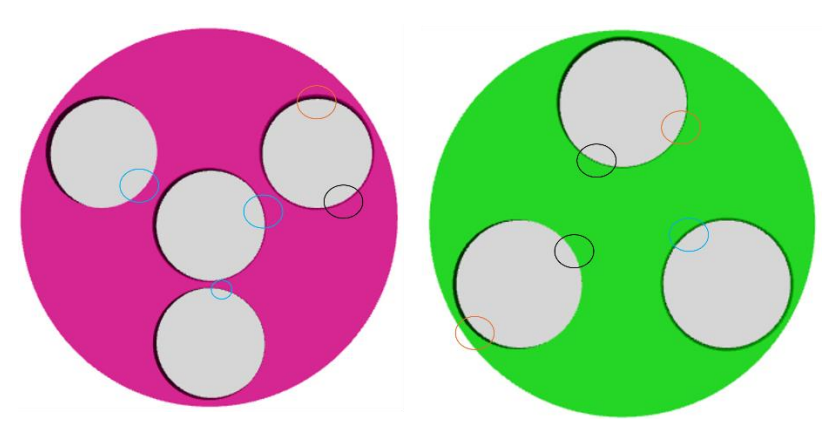


Figure 69: Plate with holes front view, where the black circles individuate maximum velocity, the orange one the maximum shear stress and the cyan one if the maximum shear and velocity coincide in the zone.

## 6.1.3 Inclined squared plates

## 6.1.3.1 Hydraulic requirements

As analysed also in Section 5, it is necessary that the flow exiting from *plate B* directly strike the inclined plates to then assume as angle of impact the angle of the disk compared to z-axis. The construction of the geometry used in Section 5 shown that the requirement is satisfied, and the same has to be done in the final configuration.

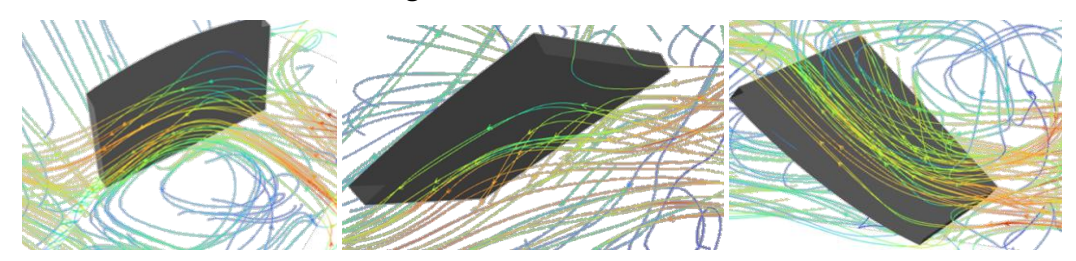


Figure 70: Path-lines coloured by velocity magnitude on the plate E, F and G (front-side, full geometry).

As analysed Section 5, the flow correctly impacts the plates in the inclined part towards its incoming direction. Compared to Figure 50 the flow is obviously more accelerated, but it also impacts slightly further down the disks, so the zones of direct impact are a little bit translated.

### 6.1.3.2 Hydraulic results

#### 6.1.3.2.1 Velocity distribution

It is important to have a look on the velocity distribution along the length of the tube to understand the magnitude of impact of the acceleration given by the geometries before:

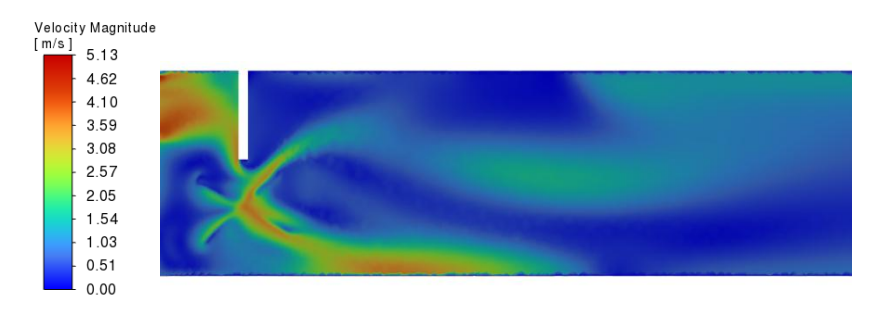


Figure 71: Contour plot of the velocity along the plane XY at z=0 of the inclined plates (full geometry).

What is visible from the above plot is that in front of the plates, and especially in this case plate E, the velocity is very high thanks to the acceleration given by the plate with holes B, that is the objective of the geometry construction. In this way the boundary layer is lower compared to the case studied in Section 5, because the inlet velocity on the plates, not uniformly but in average, is almost 4 times larger. In fact, the region where the viscous effects are important here is very restricted, or null, compared to the one with inlet condition the uniform profile of 0,8 m/s; this means that here the flow is driven by inertial forces thanks to the acceleration of the fluid mass (violet rectangle), that is translated in fluid-dynamic words as a very thin boundary layer. In this condition the streamlines of the flow outside of the boundary layer are nearly parallel to the plate.

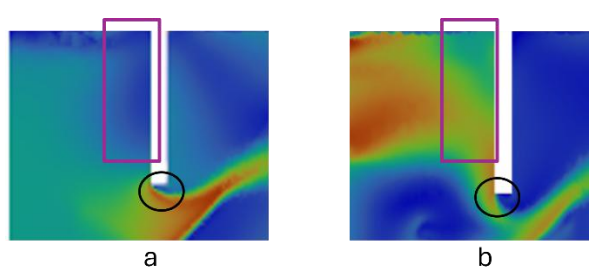


Figure 72: Zoom of Figure 51 (a) and Figure 71 (b). In the figures are underlined in the rectangles the front areas of the plate E, while in the circles the detachment points of the fluid from the plate.

Also, the separation point change and can be visualized in the black circles in Figure 72: in a the viscosity force permits to develop a detachment point before the one reached by b, where the inertial forces push the fluid more along the plate surface.

Because what said before, it is important to understand the velocity field distribution especially in front of the plates.

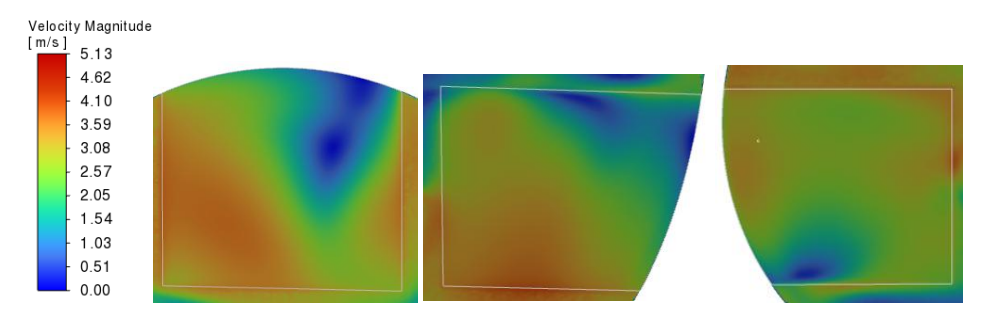


Figure 73: Velocity magnitude on front-planes parallel to the disks and placed at 0,5 mm distance before the disks themselves. In the figure from the left plate E, F and G.

### 6.1.3.2.2 Turbulence distribution

The wake zone behind the plates has to be analysed to determine the level and the location of turbulence phenomena.

It can be shown this result also on the YZ plane:

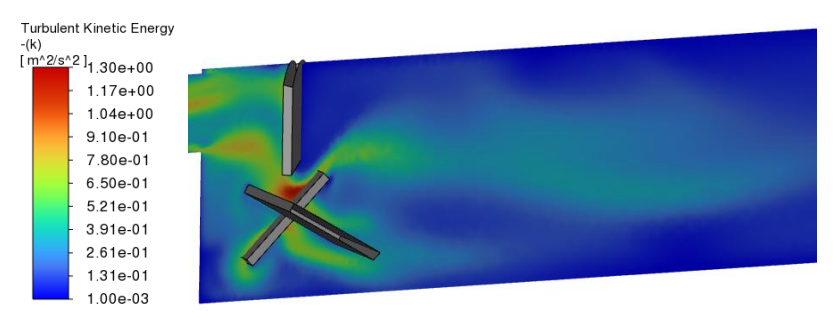


Figure 74: TKE on the YZ plane.

As can be seen by the figure above, the TKE in this case is much more impacting on the front surface of the plates compared to the back one. The TKE from Figure 74, seems much higher on the front and on the back of plate G.

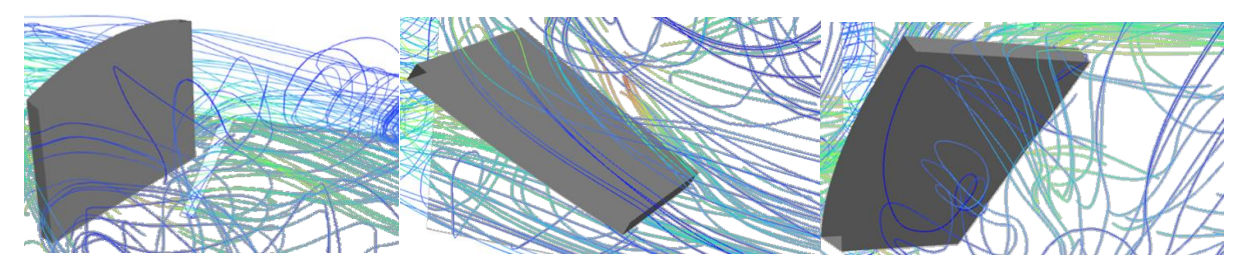


Figure 75: Path-lines coloured by TKE in the back-face of every disk. From left to right E, F and G (full geometry).

It is visible that some recirculation can appears after E and G, as happened also in Section 5. This because F has the lowest angle of impact with the fluid and it allows the fluid to be accompanied more easily along the back surface of the plate itself.

Because of this the turbulent kinetic energy is analysed in the front of all the plates and on the back of E and G:

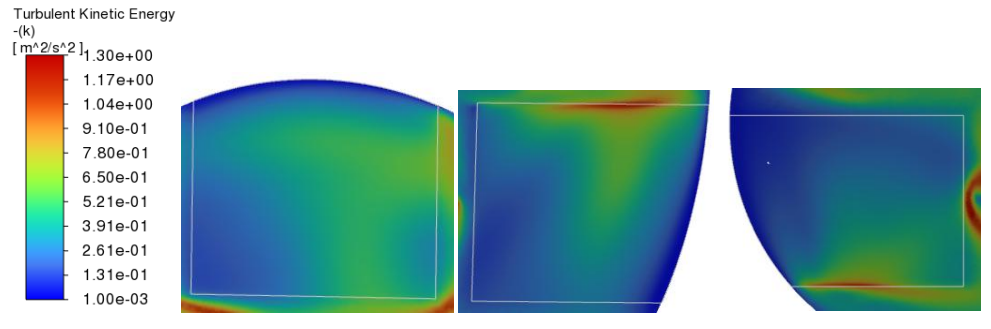


Figure 76: Front view of the TKE plot on the surfaces parallel to the plates placed 4 mm before these ones.

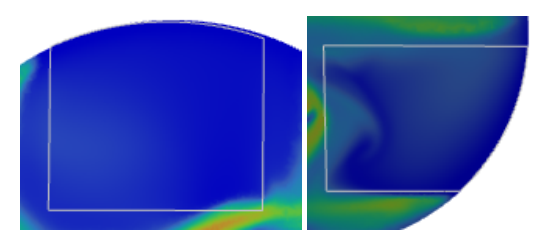


Figure 77: Back view of the TKE plot on the E and G surfaces parallel to the plates placed 4 mm after these ones.

From Figure 76 it is possible to understand that TKE is larger where the fluid is exiting from the plates, while from Figure 77 it is visible that the wake back to the plates is not subjected to high turbulence.

## 6.1.3.2.3 Impingement angle influence

The distribution of the stress is function also of the angle and because of that it is necessary to know the magnitude of its distribution on the different plates:

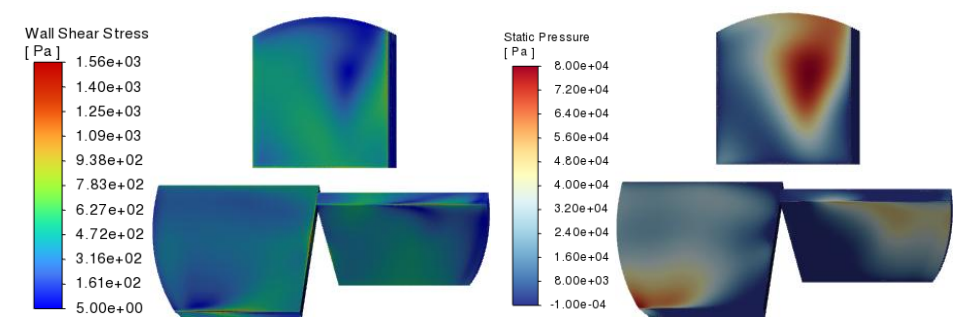
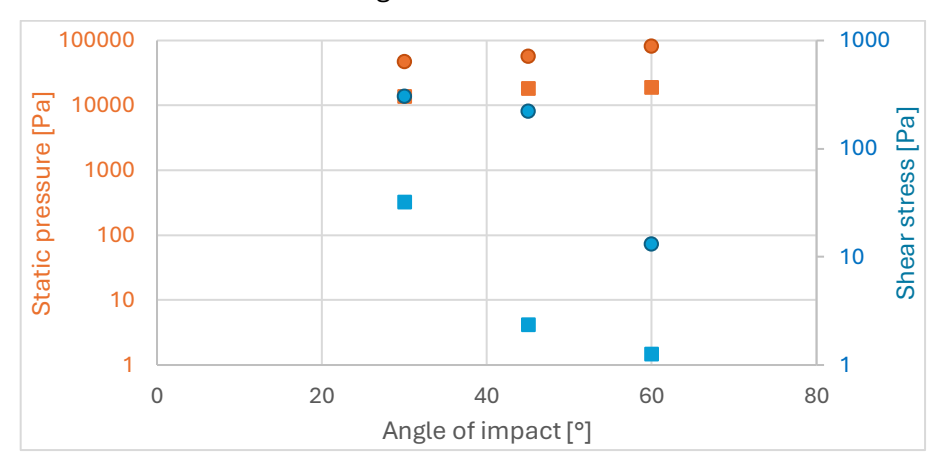


Figure 78: Shear stress and static pressure contour plots of front surfaces of the inclined plates.

As already commented during this work, the two figures are a reflection of the other and here are reported only as matter of values useful to complete the analysis when the experimental results from the test section are given.

Where the fluid directly impacts on the wall the information on the stress can be locally extract. This is done in the following graph, where it can see how a low angle of impact, such as 30°, takes to have much higher shear stress compared to higher angles. This difference is underlined by the fact that the scales of the stresses are logarithmic.



Graph 16: Stress versus angle of impact, measured on the surfaces of the inclined disks where the fluid directly impacts. Round dots are the values obtained in this analysis, while the squared ones are obtained in Section 5.

From Graph 16 it is possible also to understand the huge differences of values in shear stress between the two different simulations with different inlet conditions. In fact, in the full geometry the shear is almost 100 times higher compared to the case study in Section 5. This is due obviously to the fact that the velocity impacting the disk is more than 2 times the one of Section 5 and also, the boundary layer in this case is much narrow compared to the one in Section 5: the shear stress is proportional to the gradient of the velocity, so an higher velocity and a narrower boundary layer take obviously to high shear stresses.

# 6.2 Fragmented and full geometry conclusion

It is essential to emphasize that the primary goal of the simulation is to later correlate erosion corrosion rates with fluid dynamic data. However, this correlation must be performed locally: localized flow information is required, as average behaviour alone is insufficient for meaningful analysis.

The workflow adopted in this thesis followed a two-step approach:

- First, to optimize computational resources and reduce simulation time, a detailed analysis of fragmented geometries was conducted. These partial simulations were designed to closely replicate the behaviour of the full geometry, allowing for an early assessment of critical flow regions and validation of design criteria.
- Subsequently, a full-geometry simulation was performed to generate comprehensive data suitable for coupling with experimental measurements.

While comparing the fragmented and full simulations provided interesting insights from a fluid dynamics point of view, these differences are not directly relevant to the core objective of the study, which focuses on localized erosion corrosion phenomena.

# Conclusion

The thesis aim is to provide as many visual insights as possible through figures and data representations. However, the true value lies in the simulation files themselves, which constitute the core results of the study. Once experimental data becomes available, particularly where erosion corrosion rates are significant, it will be possible to correlate these findings with the local fluid dynamic conditions identified in the simulations.

Moreover, the simulations offer a starting point for analysis, especially in the critical regions highlighted throughout the chapters. Areas exhibiting peak or elevated values of key parameter, deserve particular attention when evaluating the test section.

Regarding the array of cylinders in backflow, the coupling between fluid dynamics and erosion corrosion effects is more straightforward in the initial columns, where the flow remains relatively stable. In contrast, the final columns require closer examination due to increased turbulence. It is important to note that in these regions, the nowadays velocity limit of 2 m/s is significantly exceeded and turbulence levels are exceptionally high.

For the perforated plates, shear stress reaches its maximum across the entire test section. Special attention must be given to the geometry of the restrictions:

- rounded restrictions exhibit both the highest velocities and the highest shear stresses;
- sharp restrictions are characterized by lower velocities but still produce high shear stress and should be avoided from a design perspective.

Additionally, it is crucial to analyse not only zones of high velocity, but also regions within the holes where velocity drops and TKE rises: these may be equally relevant to erosion corrosion processes.

Finally, for the inclined plates, shear stress is highest at a 45° inclination as expected. However, attention must also be paid to the elevated TKE values observed upstream of the plates, which may influence the onset and progression of material degradation.

It is important to remember that results near the main wall of the test section should not be considered, as they were not simulated with sufficient accuracy due to the high computational cost required to solve these regions properly.

# References

- [1]Ç. Eren and M. John, "Electricity 2025," Paris, 2025. Accessed: Mar. 11, 2025. [Online]. Available: https://www.iea.org/reports/electricity-2025
- [2] de B. Tanguy, H. Antoine, P. Nikolaos, T. Ryota, and Y. Ryo, "The Path to a New Era for Nuclear Energy," Paris, 2025. Accessed: Mar. 11, 2025. [Online]. Available: https://www.iea.org/reports/the-path-to-a-new-era-for-nuclear-energy
- [3]"Lead Fast Reactors (LFR)," GenIV International Forum. Accessed: Mar. 28, 2025. [Online]. Available: https://www.gen-4.org/generation-iv-criteria-and-technologies/lead-fast-reactors-lfr
- [4]NEA (2024), Handbook on Lead-bismuth Eutectic Alloy and Lead Properties, Materials Compatibility, Thermal-hydraulics and Technologies. Paris: OECD Publishing, 2015.
- [5] "Part I: General Aspects of Corrosion, Corrosion Control, and Corrosion Prevention," in *Corrosion Atlas Case Studies*, Elsevier, 2022, pp. xxv–xlii. doi: 10.1016/B978-0-323-85849-6.02002-3.
- [6]K. W. Wong *et al.*, "Hydrodynamic design of the Separate Effect test facility for Flow-Accelerated Corrosion and Erosion (SEFACE) studies in liquid lead," *Nuclear Engineering and Design*, vol. 417, p. 112852, Feb. 2024, doi: 10.1016/j.nucengdes.2023.112852.
- [7]T. Y. Chen, A. A. Moccari, and D. D. Macdonald, "Development of Controlled Hydrodynamic Techniques for Corrosion Testing," *Corrosion*, vol. 48, no. 3, pp. 239–255, Mar. 1992, doi: 10.5006/1.3315930.
- [8]S. Nešić, "Using computational fluid dynamics in combating erosion–corrosion," *Chem Eng Sci*, vol. 61, no. 12, pp. 4086–4097, Jun. 2006, doi: 10.1016/j.ces.2006.01.052.
- [9]I. U. Toor, H. M. Irshad, H. M. Badr, and M. A. Samad, "The Effect of Impingement Velocity and Angle Variation on the Erosion Corrosion Performance of API 5L-X65 Carbon Steel in a Flow Loop," *Metals* (*Basel*), vol. 8, no. 6, p. 402, May 2018, doi: 10.3390/met8060402.
- [10] G. A. Zhang, L. Y. Xu, and Y. F. Cheng, "Investigation of erosion–corrosion of 3003 aluminum alloy in ethylene glycol–water solution by impingement jet system," *Corros Sci*, vol. 51, no. 2, pp. 283–290, Feb. 2009, doi: 10.1016/j.corsci.2008.10.026.
- [11] "About MYRRHA." Accessed: May 12, 2025. [Online]. Available: https://myrrha.be/about-myrrha
- [12] K. Engelen, J. Pacio, and S. Keijers, "Internal communication SCK CEN."
- [13] "Ansys Fluent Theory Guide," Jan. 2025, ANSYS, Inc, Canonsburg: 2025 R1.
- [14] J. H. Ferziger and M. Perić, *Computational Methods for Fluid Dynamics*. Berlin, Heidelberg: Springer Berlin Heidelberg, 2002. doi: 10.1007/978-3-642-56026-2.
- [15] E. Amalia, M. A. Moelyadi, and M. Ihsan, "Effects of Turbulence Model and Numerical Time Steps on Von Karman Flow Behavior and Drag Accuracy of Circular Cylinder," *J Phys Conf Ser*, vol. 1005, p. 012012, Apr. 2018, doi: 10.1088/1742-6596/1005/1/012012.
- [16] Flow-induced Vibrations. Elsevier, 2014. doi: 10.1016/C2011-0-07518-X.
- [17] Robert D. Blevins, Flow Induced Vibration. Van Nostrand Reinhold, 1994.
- [18] X. Xia, Z.-J. You, J. Xu, and Y. Zhao, "Numerical study of flow characteristics around different arrays of cylinders at subcritical Reynolds number," *Ocean Engineering*, vol. 327, p. 120923, May 2025, doi: 10.1016/j.oceaneng.2025.120923.